

Die approbierte Originalversion dieser Dissertation ist an der Hauptbibliothek der Technischen Universität Wien aufgestellt (<http://www.ub.tuwien.ac.at>).

The approved original version of this thesis is available at the main library of the Vienna University of Technology (<http://www.ub.tuwien.ac.at/englweb/>).

Dissertation

Performance Evaluation of Practical OFDM Systems with Imperfect Synchronization

ausgeführt zum Zwecke der Erlangung des akademischen Grades
einer Doktorin der technischen Wissenschaften

eingereicht an der Technischen Universität Wien
Fakultät für Elektrotechnik und Informationstechnik

von

Qi Wang

geboren am 9. November 1982 in Beijing
Matrikelnummer: 0728164

Wien, im November 2012

Begutachter:

Univ. Prof. Dr.-Ing. Markus Rupp

Institute of Telecommunications

Technische Universität Wien

Österreich

Prof. Dr.-Ing. Marius Pesavento

Institut für Nachrichtentechnik

Fachgebiet Nachrichtentechnische Systeme

Technische Universität Darmstadt

Deutschland

I hereby certify that the work reported in this thesis is my own,
and the work done by other authors is appropriately cited.

Qi Wang
Vienna, September 28, 2012

Abstract

This work aims to expose the potential performance loss due to synchronization errors in the downlink of the two major cellular standards of Orthogonal Frequency Division Multiplexing (OFDM) systems, i.e., the Worldwide Inter-operability for Microwave Access (WiMAX) OFDM physical layer and the Long Term Evolution (LTE). Different to most results in literature, the physical layer coded throughput is utilized as the major performance measure. The influence of an imperfect carrier frequency synchronization or symbol timing is evaluated via analytical modeling and standard compliant link level simulations.

In the frequency aspect, a modified differential estimator for the residual frequency offset in WiMAX is proposed. It is shown that the theoretical performance of such an estimator approaches the Cramér-Rao lower bound and provides a significant gain in terms of the mean squared error. However, such an improvement becomes negligible in terms of the coded throughput. Therefore, a throughput loss prediction model is proposed for the LTE downlink. This model takes into account the entire physical layer of the LTE downlink and is able to indicate the throughput loss given an arbitrary signal-to-noise ratio and carrier frequency offset. In the timing aspect, a quantitative evaluation shows that a late timing mainly causes the inter-carrier and inter-symbol interference, whereas an early timing degrades the channel estimation performance. Therefore, an extremely accurate symbol timing is required in a coherent OFDM transmission system.

Although it is generally believed that the carrier frequency offset and symbol timing offset cause merely inter-carrier interference and inter-symbol interference, other effects, i.e., the common phase error and the additional phase variation induces negative impacts as well. Due to the overall system design constraint, these impacts may interfere the performance of other signal processing units and further degrades the system performance. These side-effects to some extent raise the requirement on the synchronization accuracy in practical OFDM systems.

Kurzfassung

Die vorliegende Arbeit zielt darauf, potentielle Übertragungsverluste verursacht durch Synchronisationsfehler in der Abwärtsstrecke von zwei bedeutenden zellularen OFDM basierten Standards aufzudecken, nämlich WiMAX und LTE. Im Gegensatz zu üblichen Verfahren der Literatur wird dabei der kodierte Datendurchsatz als wesentliches Leistungsmass herangezogen. Der Einfluss von ungenauer Trägerfrequenz und Symbol-Zeitverhalten wird mithilfe analytischer Modelle und Link-basierter Simulation von vorhandenen zellularen Standards untersucht. Bzgl. der Genauigkeit beim Frequenzversatz wird basierend auf einem modifizierten differentiellen Schätzer für WiMAX gezeigt, dass der Schätzer die Cramér-Rao Grenze erreicht und dass die Qualität signifikant erhöht wird wenn man den MSE Fehler betrachtet. Allerdings wird diese Verbesserung vernachlässigbar, wenn man den kodierten Durchsatz betrachtet. Deshalb wird eine Durchsatzverlust-Voraussage für LTE vorgeschlagen. Diese Model schließt die gesamten physikalische Schicht der LTE Abwärtsstrecke in die Betrachtung ein und erlaubt es des Durchsatzverlust auszurechnen, sobald SNR und Frequenzversatz bekannt sind. Beim Zeitverlauf zeigt sich, dass ein zu später Abtastbeginn Intercarrier und Intersymbolinterferenz erzeugen, ein zu früher Abtastbeginn hingegen verursacht einen Qualitätsverlust des Schätzers. Deshalb ist eine extrem genaue Symbolabtastzeit erforderlich, um ein kohärentes OFDM Übertragungssystem zu gewährleisten. Obwohl im Allgemeinen geglaubt wird, dass im wesentlichen nur Trägerfrequenzversatz und falsche Symbolabtastzeit Intersymbolinterferenz und Intercarrierinterferenz erzeugen, verursachen andere Effekte wie Common Phase Error und zusätzliche Phasenvariation ebenso negative Einflüsse. Wegen des Designkriteriums über dem gesamten Übertragungswegs können solche Einflüsse die Funktionalität anderer Signalverarbeitungseinheiten weiterhin negativ beeinflussen. In einem gewissen Umfang bestimmen diese Nebeneffekte auch die Anforderungen an die Synchronisationsgenauigkeit in praktischen OFDM Übertragungssystemen.

Contents

Acknowledgements	viii
Acronyms	xi
1 Introduction	1
1.1 Motivation	1
1.2 Methodology	2
1.3 Scope of the Work	2
1.4 Related Publications	4
1.5 Chapter Overview	4
2 System Model	6
2.1 Frame-based OFDM System Model	6
2.2 Carrier Frequency Offset (CFO)	8
2.2.1 Modeling	8
2.2.2 Impact on Post-FFT SINR	10
2.3 Symbol Timing Offset (STO)	11
2.3.1 Modeling	12
2.3.2 Impact on Post-FFT SINR	17
3 Carrier Frequency Synchronization in WiMAX	19
3.1 WiMAX Introduction	19
3.1.1 Transmission Resource Structure	20
3.1.2 Preambles and Pilots	21
3.2 Synchronization Procedure in WiMAX	22
3.2.1 Related Work	22

3.2.2	CFO Estimation	22
3.3	Numerical Results	28
3.3.1	Estimation Performance	28
3.3.2	Coded Throughput	30
3.4	Conclusion	31
4	LTE Performance under Carrier Frequency Offset (CFO)	33
4.1	LTE Introduction	33
4.1.1	Transmission Resource Structure	34
4.1.2	Reference Signals	35
4.1.3	Synchronization Signals	35
4.2	Carrier Frequency Offset (CFO) Estimation	35
4.3	Performance Evaluation	39
4.3.1	Estimation Performance	40
4.3.2	Post-equalization SINR	43
4.3.3	BICM Capacity and Coded Throughput	50
4.4	Conclusion	57
5	LTE Performance under Symbol Timing Offset (STO)	59
5.1	Background	59
5.2	Impact of STO on Channel Estimation	61
5.2.1	Least Squares (LS) Channel Estimator	62
5.2.2	Linear Minimum Mean Squared Error (LMMSE) Channel Es- timator	66
5.3	Post-Equalization SINR Evaluation	70
5.3.1	Perfect Channel Knowledge	70
5.3.2	Imperfect Channel Knowledge	72
5.4	Coded Throughput	74
5.5	Conclusion	75
6	Summary	76
6.1	Contributions	76
6.2	Outlook	77
	Bibliography	84

A	Differential RFO Estimation	85
A.1	Theoretical Mean Squared Error (MSE) - derivation of Equation (3.9)	85
B	CRLB of the Residual Frequency Offset (RFO) Estimator using Pilot Subcarriers	87
C	Maximum Likelihood Estimator	93
C.1	Fractional Frequency Offset (FFO) - derivation of Equation (4.1) . .	93
C.2	Integer Frequency Offset (IFO) - derivation of Equation (4.4)	94
C.3	Residual Frequency Offset (RFO) - derivation of Equation (4.6) . . .	95
D	Theoretical MSE and Cramér-Rao Lower Bound (CRLB)	97
D.1	Theoretical MSE - derivation of Equation (4.9)	97
D.2	Cramér-Rao Lower Bound (CRLB) - derivation of Equation (4.10) .	98

Acknowledgements

First and foremost, I would like to thank my supervisor Markus Rupp for offering me this great opportunity to pursue the doctor study in Vienna. Without his endless trust, help and encouragement, this thesis would never have become real.

I owe my deepest gratitude to Sebastian Caban and Christian Mehlführer for their guidance, support and patience during the beginning phase of my thesis work; to people who have been working together as the *LTE group* for sharing all their knowledge, experiences and inspirations; especially to those who were/are in the MIMO lab, to name a few, Dasa Bošanska, Josep Colom Ikuno, José Antonio García Naya, Aamir Habib, Markus Hofer and Michal Šimko, for those fruitful or unfruitful discussions and argumentation, most importantly, for making our work environment enjoyable.

Such a thesis would not have been possible without a cooperative atmosphere provided by everyone at our institute. I must thank Carolina Reyes for always "kicking" me back to work at the right point. For the support on a mental and financial basis, my acknowledgement goes to fFORTE WIT - Women in Technology Programme of Vienna University of Technology.

Last but not least, thanks to all my friends, here and there, especially the so-called "Chinese mafia", namely Mingming Gan, Yao Pan, Zhinan Xu and Hua Zhou for the time we spent together here far away from home; to Arian Bär for holding my hand at a hard moment and encouraging me to fight till the end. To my parents in China, for their understanding and support through these years, despite their incomprehension about what I do, no words can express my gratitude.

Acronyms

3GPP	3rd Generation Partnership Project
AMC	Adaptive Modulation and Coding
AWGN	Additive White Gaussian Noise
BER	Bit Error Ratio
BICM	Bit-Interleaved Coded Modulation
BLER	Block Error Ratio
BPSK	Binary Phase-Shift Keying
BS	Base Station
CFO	Carrier Frequency Offset
CP	Cyclic Prefix
CPE	Common Phase Error
CQI	Channel Quality Indicator
CRLB	Cramér-Rao Lower Bound
DL	Downlink
ECR	Effective Code Rate
FCH	Frame Control Header
FDD	Frequency Division Duplex
FFT	Fast Fourier Transform
FFO	Fractional Frequency Offset
ICI	Inter-Carrier Interference

IEEE	Institute of Electrical and Electronics Engineers
IFFT	Inverse Fast Fourier Transform
IFO	Integer Frequency Offset
ISI	Inter-Symbol Interference
LDPC	Low Density Parity Check
LMMSE	Linear Minimum Mean Squared Error
LOS	Line-of-Sight
LS	Least Squares
LTE	Long Term Evolution
MCS	Modulation and Coding Scheme
MIMO	Multiple Input and Multiple Output
MIESM	Mutual Information Effective SINR Mapping
ML	Maximum Likelihood
MMSE	Minimum Mean Squared Error
MSE	Mean Squared Error
NLOS	Non-Line-of-Sight
OFDM	Orthogonal Frequency Division Multiplexing
OFDMA	Orthogonal Frequency Division Multiple Access
PAM	Pulse-Amplitude Modulation
PDP	Power Delay Profile
PDU	Protocol Data Unit
PSS	Primary Synchronization Signal
QPSK	Quadrature Phase-Shift Keying
QAM	Quadrature Amplitude Modulation
RB	Resource Block
RE	Resource Element
RFO	Residual Frequency Offset
RS	Reference Signal
RX	Receiver
SC	Single Carrier
SC-FDMA	Single-Carrier Frequency Division Multiple Access

SER	Symbol Error Ratio
SINR	Signal to Interference-plus-Noise Ratio
SISO	Single Input and Single Output
SNR	Signal to Noise Ratio
SS	Subscriber Station
SSS	Secondary Synchronization Signal
STO	Symbol Timing Offset
TDD	Time Division Duplex
TX	Transmitter
UE	User Equipment
UL	Uplink
WiMAX	Worldwide Inter-operability for Microwave Access
WLAN	Wireless Local Area Network
ZF	Zero Forcing

1. Introduction

By the end of 2009, mobile data traffic outnumbered voice traffic for the first time, according to the wireless equipment vendor Ericsson. People tend to have always-on, always accessible broadband connections, creating huge demand on the capability of nowadays mobile wireless communication technologies. Driven by the creation and development of new services for mobile devices, innovative techniques are involved in the next generation standards for wireless communications in order to fulfill the ever growing desire on the system performance.

1.1. Motivation

Orthogonal Frequency Division Multiplexing (OFDM) has become a dominant physical layer technique of modern wireless communication systems owing to its high spectrum efficiency and robustness to frequency selective channels [1, 2]. However, these advantages are guaranteed only when the orthogonality between subcarriers is ideally preserved. With synchronization errors, typically a Carrier Frequency Offset (CFO) or a Symbol Timing Offset (STO), this orthogonality will be lost. The CFO introduces Common Phase Errors (CPEs) and Inter-Carrier Interference (ICI) and therefore degrades the system performance considerably [3]. Equivalent to an additional temporal dispersion of the channel, an inaccurate symbol timing can also cause significant Inter-Symbol Interference (ISI) and ICI [4].

Over the last decades, research efforts have been devoted to the synchronization aspects in OFDM transmissions. Novel and enhanced estimators were developed in order to compensate the CFO or STO. Their performance is usually evaluated in terms of the estimation error, in other words, the Mean Squared Error (MSE) between the true offset and its estimate. While for a communication system in

practice, the performance is evaluated in terms of the overall data throughput, encompassing all the signal processing steps applied at the transmitter and receiver, e.g., coding, modulation, equalization and detection. Therefore, it is not merely the estimation error that counts but its impact on the physical layer performance.

The goal of this thesis is to evaluate the performance of practical OFDM systems under imperfect synchronization, and to expose the impact of the residual synchronization error on the link performance.

1.2. Methodology

For evaluating the performance of communication systems, different approaches with their individual strengths and weaknesses have been developed. The most important approaches are formula-based calculation, waveform-level simulation and measurements using hardware-based prototyping. With a simulation-based approach, a communication system can be modeled on any desired level of detail. Wherein, mathematical and empirical models can be easily combined [5]. Therefore, the simulation approach is mostly adopted in today's research for its flexibility and efficiency.

In order to enable the reproducibility of research results and bridge the gap between researchers and standardization entities, we developed MATLAB based standard compliant simulation environments for the Worldwide Inter-operability for Microwave Access (WiMAX) OFDM physical layer [6] and Long Term Evolution (LTE) [7] at the Institute of Telecommunications, Vienna University of Technology. These simulators greatly ease the investigation on the system performance of practical OFDM systems.

However, as nowadays communication systems grow in complexity, simulating a perfect replica of the real system becomes costly in terms of run time efficiency. In order to reduce the simulation complexity without losing the insight to the reality, modeling with an acceptable degree of approximations is desired. In this thesis, we derive mathematical models that evaluate the link performance loss, given corresponding system parameters and arbitrary synchronization errors. The models are validated by extensive standard compliant simulations using the above-mentioned Vienna LTE link level simulator.

1.3. Scope of the Work

In this work, we consider two OFDM systems in practice, namely the OFDM physical layer in WiMAX and LTE for which standardized frame structures are defined in [8, 9]. WiMAX can be regarded as a representative of the Institute of Electrical and

Electronics Engineers (IEEE) 802.11/16 protocol suite which employs the OFDM as the physical layer technique. Whereas, LTE exemplifies the recent trend of using OFDM as a multiple access technique.

The performance evaluation of these two systems is based on the following underlying assumptions:

- **Block Fading Scenario**

Due to the requirement of spectrum efficiency and the constraint of computational complexity in practical communication systems, block fading is usually assumed on a frame basis. In this case, the frame duration is specified to be smaller than the channel coherence time, such that the system can be treated as time invariant within this time interval. Under this assumption, data transmission and signal processing on the receiver side can be carried out on a frame basis.

- **Single Link Physical Layer**

The performance evaluation is restricted to the physical layer link between a single base station and a single user.

Under these assumptions, two types of synchronization errors are taken into account:

- **Carrier Frequency Offset**

Carrier frequency synchronization is a crucial issue in an OFDM system. The mismatch between the local oscillators at the transmitter and the receiver introduces a CFO. While in simulations the CFO can readily be set to zero, this is never the case in real systems. Due to cost limitations, local oscillators on the User Equipment (UE) side may have a typical frequency stability tolerance of ± 2 ppm. Consider an oscillator at 2.5 GHz, a ± 2 ppm frequency drift results in an offset of ± 5 kHz. With the fixed subcarrier spacing of 15 kHz defined in LTE, a CFO of ± 0.33 subcarrier spacing needs to be handled at the receiver.

- **Symbol Timing Offset**

The STO is referred to as the mismatch between the Fast Fourier Transform (FFT) window of the OFDM demodulation in the Receiver (RX) and that of the modulation in the Transmitter (TX). A symbol timing error occurs when the RX is not able to detect the start of an OFDM symbol accurately. In a frame-based system, the symbol timing corresponds to the frame timing. Although it is generally believed that the symbol timing issue is eased by the introduction of the Cyclic Prefix (CP), this is not the case in a time dispersive channel.

1.4. Related Publications

The content of this thesis is to some extent based on the following peer-reviewed publications:

- [1] Q. Wang, C. Mehlführer, and M. Rupp, “**SNR optimized residual frequency offset compensation for WiMAX with throughput evaluation,**” in *Proc. 17th European Signal Processing Conference (EUSIPCO 2009)*, Glasgow, Scotland, Aug. 2009.
- [2] Q. Wang, S. Caban, C. Mehlführer, and M. Rupp, “**Measurement based throughput evaluation of residual frequency offset compensation in WiMAX,**” in *Proc. 51st International Symposium ELMAR-2009*, Zadar, Croatia, Sept. 2009.
- [3] Q. Wang, C. Mehlführer, and M. Rupp, “**Carrier frequency synchronization in the downlink of 3GPP LTE,**” in *Proceeding of the 21st Annual IEEE International Symposium on Personal, Indoor and Mobile Radio Communications (PIMRC'10)*, Istanbul, Turkey, Sept. 2010.
- [4] Q. Wang, M. Šimko, and M. Rupp, “**Modified symbol timing offset estimation for OFDM over frequency selective channels,**” in *Proceeding of IEEE 74th Vehicular Technology Conference (VTC2011-Fall)*, San Francisco, USA, Sept. 2011.
- [5] Q. Wang and M. Rupp, “**Analytical link performance evaluation of LTE downlink with carrier frequency offset,**” in *Conference Record of the 45th Asilomar Conference on Signals, Systems and Computers, 2011 (Asilomar-2011)*, Pacific Grove, USA, Nov. 2011.
- [6] Q. Wang, “**Frequency synchronization,**” in *Evaluation of HSDPA and LTE: From Testbed Measurements to System Level Performance*, S. Caban, C. Mehlführer, M. Rupp, and M. Wrulich, Eds. John Wiley & Sons, Ltd, 2012.
- [7] Q. Wang, M. Šimko, and M. Rupp, “**Performance analysis of LTE downlink under symbol timing offset,**” in *IEEE Proceedings of Workshop on Smart Antennas 2012 (WSA-2012)*, Dresden, Germany, Mar. 2012.
- [8] S. Schwarz, J. C. Ikuno, M. Šimko, M. Taranetz, Q. Wang, and M. Rupp, “**Pushing the limits of LTE: A survey on research enhancing the standard,**” *IEEE Communications Magazine*, submitted for publication.

1.5. Chapter Overview

This thesis is structured as follows:

In Chapter 2, the system model is presented. This model in general applies to any frame-based OFDM transmission systems. The impact of a CFO and an STO on the signal after the OFDM demodulation is shown analytically without taking into account the successive signal processing steps in the RX.

In Chapter 3, the OFDM physical layer of WiMAX (in particular IEEE 802.16-

2009 [8, Section 8.3] and the implementation in [6]) is considered. A three-step carrier frequency synchronization scheme using the standardized preamble and pilot symbols is elaborated. Results from simulation based performance evaluations are provided. A modified differential estimator shows significant improvement in terms of estimation error, approaching the Cramér-Rao lower bound. However, this improvement becomes negligible in terms of the system throughput.

In Chapter 4, the impact of a residual CFO on the system performance of LTE is modeled. Firstly, the estimation performance of the three-step CFO estimator is shown in the context of LTE. Secondly, as an intermediate metric that indicates the link performance, a post-equalization Signal to Interference-plus-Noise Ratio (SINR) model is derived. Finally, the Bit-Interleaved Coded Modulation (BICM) capacity is employed to estimate the throughput loss of the system. Such a model provides a direct mapping between the CFO estimation performance and the coded throughput loss in the LTE Downlink (DL).

In Chapter 5, the impact of an imperfect symbol timing on the LTE DL is investigated. The major influence from a residual STO appears in the channel estimator. The incremental channel estimation error thus degrades the link performance. A post-equalization SINR model that describes such an influence is derived analytically and evaluated via simulations.

In Chapter 6, a summary of the main contributions of this thesis can be found. Detailed derivations of the CFO estimators, their theoretical estimation errors and performance bounds are presented in the Appendices A to D.

2. System Model

This chapter presents the system model as a basis of the following chapters. In Section 2.1, the signal model of a frame based Orthogonal Frequency Division Multiplexing (OFDM) system is introduced. The Carrier Frequency Offset (CFO) in such a system is modeled in Section 2.2 and the Symbol Timing Offset (STO) in Section 2.3. Their impact on the signal after the OFDM demodulation is shown. The analysis in this chapter is independent from specification related aspects, thus applies to any OFDM system in general.

2.1. Frame-based OFDM System Model

Nowadays most wireless communication systems based on OFDM utilize certain frame structures [8, 9]. A frame is defined as a certain number of OFDM symbols with a corresponding region for control signaling. The frame length is designed to be shorter than the channel coherence time so that a quasi-static scenario can be assumed within a frame duration. Such a design not only eases the signal processing in the transceiver, but also reduces the overhead for signaling.

In a typical OFDM system, as depicted in Figure 2.1, the information bits are firstly processed at the bit level by, e.g., encoding, interleaving and more. Then, they are mapped onto data symbols according to a certain modulation scheme, i.e., Quadrature Phase-Shift Keying (QPSK), 16/64 Quadrature Amplitude Modulation (QAM). The symbol level processing includes typically spatial multiplexing and precoding. Afterwards, the signal is transformed into the time domain using an Inverse Fast Fourier Transform (IFFT), which is equivalent to modulate every N symbols onto N orthogonal subcarriers. Cyclic Prefixes (CPs) of length N_g are appended in or-

der to mitigate the Inter-Symbol Interference (ISI). On the receiver side, a reverse procedure is applied.

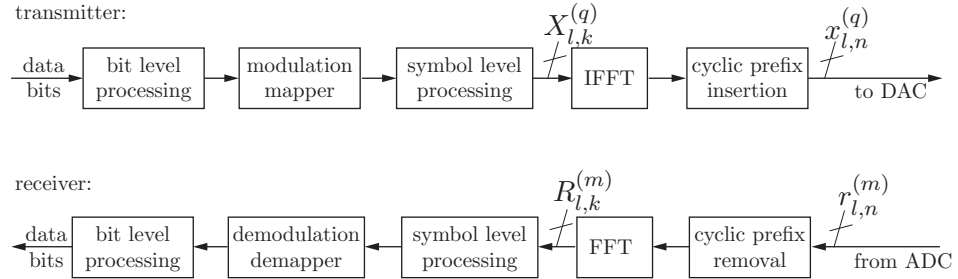


Figure 2.1: OFDM signal processing chain.

In order to describe this procedure mathematically, we denote the transmitted OFDM signal in the frequency domain by $X_{l,k}^{(q)}$ and in the time domain by $x_{l,n}^{(q)}$, where $l \in [0, \dots, N_f - 1]$ is the OFDM symbol index within one frame, $n \in [-N_g, \dots, 0, \dots, N - 1]$ the time index within one OFDM symbol, $k \in [0, \dots, N - 1]$ the subcarrier index and $q \in [1, \dots, N_T]$ the transmit antenna index. Through an IFFT, the OFDM signal is generated as,

$$x_{l,n}^{(q)} = \frac{1}{\sqrt{N}} \sum_{k=0}^{N-1} X_{l,k}^{(q)} \cdot e^{i \frac{2\pi n k}{N}}, \quad q = 1, 2, \dots, N_T. \quad (2.1)$$

Similarly, we denote the channel impulse response between Transmitter (TX) antenna q and Receiver (RX) antenna m by $h_{l,n}^{(m,q)}$, the additive white Gaussian noise at the RX antenna m by $v_{l,n}^{(m)}$, and the received time domain signal by $r_{l,n}^{(m)}$. The received signal can be written as

$$r_{l,n}^{(m)} = \sum_{q=1}^{N_T} x_{l,n}^{(q)} * h_{l,n}^{(m,q)} + v_{l,n}^{(m)}, \quad m = 1, 2, \dots, N_R, \quad (2.2)$$

where $*$ denotes a convolution.

Given the assumption that the CP is longer than the maximum channel delay and perfect timing/frequency synchronization is guaranteed, data symbols at antenna m can be demodulated using a Fast Fourier Transform (FFT), expressed as

$$R_{l,k}^{(m)} = \frac{1}{\sqrt{N}} \sum_{n=0}^{N-1} r_{l,n}^{(m)} \cdot e^{-i \frac{2\pi n k}{N}} = \sum_{q=1}^{N_T} X_{l,k}^{(q)} H_{l,k}^{(m,q)} + V_{l,k}^{(m)}, \quad m = 1, 2, \dots, N_R, \quad (2.3)$$

where correspondingly, $R_{l,k}^{(m)}$ denotes the received symbol, $H_{l,k}^{(m,q)}$ the channel re-

response and $V_{l,k}^{(m)}$ the additive white Gaussian noise in the frequency domain at the RX antenna m .

In this ideal case, the orthogonality between the subcarriers is preserved, namely on a certain subcarrier k at the RX side, only the signal which is transmitted on subcarrier k is received. Instead of one single channel of higher rate, the data symbols are conveyed through N parallel subchannels of lower rate without interfering each other.

2.2. Carrier Frequency Offset (CFO)

A CFO is the difference between the carrier frequencies generated at the two local oscillators at the TX and the RX. In general, it has a twofold impact on OFDM signals. Consider an extreme case that a 10 ppm CFO occurs in an Long Term Evolution (LTE) system. Normalized to the 15 kHz subcarrier spacing for analysis purpose, it corresponds to $\varepsilon_{\text{CFO}} = \pm 1.67$. The fractional part ± 0.67 of ε_{CFO} induces Inter-Carrier Interference (ICI) to the OFDM signal. The integer part ± 1 poses a mismatch of the subcarrier indices between the TX and the RX. In this section, we present a mathematical model of an OFDM signal that experiences imperfect carrier frequency synchronization. This model will be applied to the analysis in the latter chapters, i.e., Chapter 3 and Chapter 4.

2.2.1. Modeling

For a Multiple Input and Multiple Output (MIMO) communications system, it is generally assumed that all TX(RX) antennas are served by one common local oscillator on the TX(RX) side, leading to a common CFO for all antenna pairs. In the mathematical model, the CFO is normalized to the subcarrier spacing and denoted by ε_{CFO} . When a CFO occurs, the received signal in the time domain in Equation (2.2) becomes

$$r_{l,n}^{(m)} = \left\{ \sum_{q=1}^{N_{\text{T}}} x_{l,n}^{(q)} * h_{l,n}^{(m,q)} + v_{l,n}^{(m)} \right\} \cdot e^{i \frac{2\pi \varepsilon_{\text{CFO}} (n+l(N+N_{\text{g}}))}{N}}, \quad m = 1, 2, \dots, N_{\text{R}}. \quad (2.4)$$

Correspondingly, in the frequency-domain, there is

$$\begin{aligned}
 R_{l,k}^{(m)} &= \sum_{n=0}^{N-1} r_{l,n}^{(m)} e^{-i\frac{2\pi kn}{N}} \\
 &= \sum_{n=0}^{N-1} \left\{ \left\{ \sum_{q=1}^{N_T} x_{l,n}^{(q)} * h_{l,n}^{(m,q)} + v_{l,n}^{(m)} \right\} \cdot e^{i\frac{2\pi \varepsilon_{\text{CFO}} n}{N}} \cdot e^{i\frac{2\pi \varepsilon_{\text{CFO}} l(N+N_g)}{N}} \right\} \cdot e^{-i\frac{2\pi kn}{N}} \\
 &= e^{i\frac{2\pi \varepsilon_{\text{CFO}} l(N+N_g)}{N}} \cdot \sum_{n=0}^{N-1} \left\{ \sum_{q=1}^{N_T} x_{l,n}^{(q)} * h_{l,n}^{(m,q)} + v_{l,n}^{(m)} \right\} \cdot e^{i\frac{2\pi \varepsilon_{\text{CFO}} n}{N}} \cdot e^{-i\frac{2\pi kn}{N}}
 \end{aligned} \tag{2.5}$$

According to the convolution theorem, this further leads to

$$\begin{aligned}
 R_{l,k}^{(m)} &= e^{i\frac{2\pi \varepsilon_{\text{CFO}} l(N+N_g)}{N}} \cdot \sum_{q=1}^{N_T} \left\{ X_{l,k}^{(q)} H_{l,k}^{(m,q)} \right\} * \left\{ \frac{1}{N} \sum_{n=0}^{N-1} e^{i\frac{2\pi \varepsilon_{\text{CFO}} n}{N}} \cdot e^{-i\frac{2\pi kn}{N}} \right\} + \tilde{V}_{l,k}^{(m)} \\
 &= e^{i\frac{2\pi \varepsilon_{\text{CFO}} l(N+N_g)}{N}} \cdot \sum_{q=1}^{N_T} \left\{ X_{l,k}^{(q)} H_{l,k}^{(m,q)} \right\} *
 \end{aligned} \tag{2.6}$$

$$\begin{aligned}
 & * \left\{ \frac{\sin[\pi(\varepsilon_{\text{CFO}} - k)]}{N \sin[\pi(\varepsilon_{\text{CFO}} - k)/N]} \cdot e^{i\frac{\pi(\varepsilon_{\text{CFO}} - k)(N-1)}{N}} \right\} + \tilde{V}_{l,k}^{(m)} \\
 & = e^{i\frac{2\pi \varepsilon_{\text{CFO}} l(N+N_g)}{N}} \cdot \sum_{q=1}^{N_T} \left\{ \sum_{p=0}^{N-1} X_{l,p}^{(q)} H_{l,p}^{(m,q)} \frac{\sin[\pi(p - k + \varepsilon_{\text{CFO}})]}{N \sin[\pi(p - k + \varepsilon_{\text{CFO}})/N]} \right. \\
 & \quad \left. \cdot e^{i\frac{\pi(p - k + \varepsilon_{\text{CFO}})(N-1)}{N}} \right\} + \tilde{V}_{l,k}^{(m)}
 \end{aligned} \tag{2.7}$$

Here, $\tilde{V}_{l,k}^{(m)}$ denotes the noise term $V_{l,k}^{(m)}$ in Equation (2.3) which is rotationally altered by the CFO. Since the phase of a complex-valued Gaussian variable follows a uniform distribution in $[-\pi, \pi]$, the CFO does not change the statistical properties of the noise term. In order to elaborate the twofold impact, we split the total CFO into a fractional part ε_{FFO} and an integer part ε_{IFO} with $\varepsilon_{\text{CFO}} = \varepsilon_{\text{FFO}} + \varepsilon_{\text{IFO}}$. Thus, in Equation (2.6), there is

$$p - k + \varepsilon_{\text{CFO}} = p - k + \varepsilon_{\text{FFO}} + \varepsilon_{\text{IFO}} = p + \varepsilon_{\text{FFO}} - \underbrace{(k - \varepsilon_{\text{IFO}})}_{k'}, \tag{2.8}$$

where $k' = k - \varepsilon_{\text{IFO}}$ is the true subcarrier index at the receiver. This implies that data symbols transmitted on subcarrier $k' = k - \varepsilon_{\text{IFO}}$ are received on subcarrier k . It further allows the separation of signal and interference terms from Equation (2.7)

to

$$\begin{aligned}
 R_{l,k}^{(m)} = & \underbrace{I(0, \varepsilon_{\text{FFO}}) \cdot e^{i\Phi(\varepsilon_{\text{CFO}}, l)} \cdot \sum_{q=1}^{N_{\text{T}}} X_{l,k'}^{(q)} H_{l,k'}^{(m,q)}}_{\text{signal}} + \\
 & + \underbrace{\sum_{p \neq k'} \sum_{q=1}^{N_{\text{T}}} X_{l,p}^{(q)} H_{l,p}^{(m,q)} \cdot I(p - k', \varepsilon_{\text{FFO}}) \cdot e^{i\Phi(\varepsilon_{\text{CFO}}, l)}}_{\text{interference}} + \underbrace{\tilde{V}_{l,k}^{(m)}}_{\text{noise}}, \quad (2.9)
 \end{aligned}$$

with

$$I(0, \varepsilon_{\text{FFO}}) = \frac{\sin(\pi \varepsilon_{\text{FFO}})}{N \sin(\pi \varepsilon_{\text{FFO}}/N)} \cdot e^{i \frac{\pi \varepsilon_{\text{FFO}}(N-1)}{N}}, \quad (2.10)$$

$$\begin{aligned}
 I(p - k', \varepsilon_{\text{FFO}}) &= \frac{\sin[\pi(p - k' + \varepsilon_{\text{CFO}})]}{N \sin[\pi(p - k' + \varepsilon_{\text{CFO}})/N]} \cdot e^{i \frac{\pi(p - k' + \varepsilon_{\text{CFO}})(N-1)}{N}} \quad (2.11) \\
 &= \frac{\sin[\pi(p - k' + \varepsilon_{\text{FFO}})]}{N \sin[\pi(p - k' + \varepsilon_{\text{FFO}})/N]} \cdot e^{i \frac{\pi(p - k' + \varepsilon_{\text{FFO}})(N-1)}{N}},
 \end{aligned}$$

$$e^{i\Phi(\varepsilon_{\text{CFO}}, l)} = e^{i \frac{2\pi \varepsilon_{\text{CFO}} l (N + N_{\text{g}})}{N}}. \quad (2.12)$$

It is noted that $I(0, \varepsilon_{\text{FFO}})$ is merely dependent on ε_{FFO} and constant over the time index l , whereas $e^{i\Phi(\varepsilon_{\text{CFO}}, l)}$, known as Common Phase Error (CPE), is time-variant but identical for all the subcarriers. In summary, the CFO has a twofold impact on the received signal:

- A distortion to the desired signal $I(0, \varepsilon_{\text{FFO}}) \cdot e^{i\Phi(\varepsilon_{\text{CFO}}, l)}$ and the ICI terms weighted by $I(p - k', \varepsilon_{\text{FFO}}) \cdot e^{i\Phi(\varepsilon_{\text{CFO}}, l)}$.
- An undesirable mismatch of the subcarrier indices between the TX and the RX, denoted by $k' = k - \varepsilon_{\text{IFO}}$.

2.2.2. Impact on Post-FFT SINR

As it is shown in Equation (2.9), the ICI occurs after the FFT and is applied at the RX. The effect of imperfect frequency synchronization to OFDM systems can be measured by Signal to Interference-plus-Noise Ratio (SINR) after the FFT, as suggested in [3, 10, 11].

Based on the system model Equations (2.9) to (2.12), the power of the signal, the

interference and the noise term can be calculated as

$$\begin{aligned} E_S &= \sigma_s^2 \cdot |I(0, \varepsilon_{\text{FFO}})|^2 \cdot \sum_{q=1}^{N_T} \mathbb{E}\{|H_{l,k'}^{(m,q)}|^2\} \\ &= \sigma_s^2 \left[\frac{\sin(\pi\varepsilon_{\text{FFO}})}{N \sin(\pi\varepsilon_{\text{FFO}}/N)} \right]^2 \sum_{q=1}^{N_T} \mathbb{E}\{|H_{l,k'}^{(m,q)}|^2\}, \end{aligned} \quad (2.13)$$

$$E_I = \sigma_s^2 \left[1 - \left(\frac{\sin(\pi\varepsilon_{\text{FFO}})}{N \sin(\pi\varepsilon_{\text{FFO}}/N)} \right)^2 \right] \sum_{q=1}^{N_T} \mathbb{E}\{|H_{l,k'}^{(m,q)}|^2\}, \quad (2.14)$$

$$E_N = \mathbb{E}\{|\tilde{V}_{l,k}^{(m)}|^2\} = \sigma_v^2, \quad (2.15)$$

where $\sigma_s^2 = \mathbb{E}\{|X_{l,k}^{(m)}|^2\}$ denotes the average transmit power on each subcarrier. Thus, the so-called post-FFT SINR per subcarrier can be written as

$$\begin{aligned} \text{SINR}_{l,k}^{(m)} &= \frac{E_S}{E_I + E_N} \\ &= \frac{\sigma_s^2 \left[\frac{\sin(\pi\varepsilon_{\text{FFO}})}{N \sin(\pi\varepsilon_{\text{FFO}}/N)} \right]^2 \sum_{q=1}^{N_T} \mathbb{E}\{|H_{l,k'}^{(m,q)}|^2\}}{\sigma_s^2 \left[1 - \left(\frac{\sin(\pi\varepsilon_{\text{FFO}})}{N \sin(\pi\varepsilon_{\text{FFO}}/N)} \right)^2 \right] \sum_{q=1}^{N_T} \mathbb{E}\{|H_{l,k'}^{(m,q)}|^2\} + \sigma_v^2} \\ &\cong \frac{\left[\frac{\sin(\pi\varepsilon_{\text{FFO}})}{N \sin(\pi\varepsilon_{\text{FFO}}/N)} \right]^2}{1 - \left[\frac{\sin(\pi\varepsilon_{\text{FFO}})}{N \sin(\pi\varepsilon_{\text{FFO}}/N)} \right]^2} \quad \text{for high SNRs.} \end{aligned} \quad (2.16)$$

Till here, it is shown that the ICI is merely caused by the fractional part of the ε_{CFO} , although the mismatch of the subcarrier indices between the TX and the RX destroy the data transmission entirely. In Figure 2.2, as an example, we plot the post-FFT SINR against varying levels of CFO at different SNRs over an Additive White Gaussian Noise (AWGN) channel. The FFT size $N = 128$ is chosen.

Figure 2.2 shows that the system is more sensitive to the ICI for higher SNRs where higher-order Modulation and Coding Schemes (MCSs) are supposed to be applied. Even so, this impact is fairly negligible for a CFO around $\varepsilon < 0.004$, as claimed in [3]. In the later chapter, it will be shown that in fact $\varepsilon < 0.001$ must be guaranteed.

2.3. Symbol Timing Offset (STO)

One key principle of OFDM is that in order to eliminate ISI in a multi-path channel, a guard interval is appended at the beginning of each OFDM symbol. These so-called CPs are corrupted by the delayed versions of the previous OFDM symbol. With a designed CP longer than the maximum channel excess delay, ISI can be fully avoided

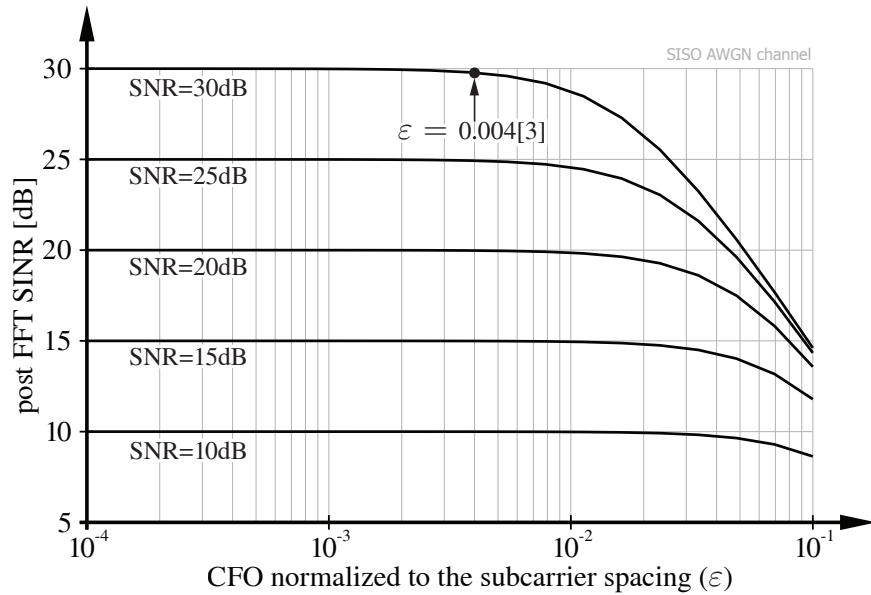


Figure 2.2: Calculated post-FFT SINRs in AWGN channel ($N = 128$).

at the receiver side simply by the CP removal.

It is generally believed that the CP to some extent, provides the system a certain tolerance to the timing synchronization error. As long as the FFT is applied to an ISI-free region, no additional interference is introduced. However, as the channel maximum excess delay grows, the ISI-free region shrinks correspondingly, leaving timing synchronization a crucial issue again.

In this section, as a basis for Chapter 5, a mathematical model for an OFDM system with imperfect symbol timing is presented.

2.3.1. Modeling

In this work, we consider an integer-valued STO of θ sampling periods, i.e., $\theta \in \mathbb{Z}$. The sampling time index is referred to as n , the OFDM symbol index as l and the subcarrier indices as k and p . Among the N subcarriers, only N_{tot} of them are occupied by data symbols, while the rest are reserved as guard band. This frame structure is illustrated in Figure 2.3.

Given a block fading assumption on a frame basis, the channel within a time interval of N_f OFDM symbols is regarded to be quasi-static. Thus, a multi-path channel in the time domain is described by

$$h_n = \sum_{\tau=0}^L c_{\tau} \cdot \delta_K(n - \tau), \quad (2.17)$$

be interpreted as the transfer functions for the desired signal $\underline{\mathbf{x}}_l$ and the interfering signal $\underline{\mathbf{x}}_{\text{int}}$.

Specifically,

$$\mathbf{P} = \begin{bmatrix} \mathbf{0} & \mathbf{I}_{N_{\text{tot}}/2} \\ \mathbf{0} & \mathbf{0} \\ \mathbf{I}_{N_{\text{tot}}/2} & \mathbf{0} \end{bmatrix}_{N \times N_{\text{tot}}} \quad (2.22)$$

is the zero-subcarrier-padding matrix of size $N \times N_{\text{tot}}$ so that the inter-band interference is eliminated. Here, $\mathbf{0}$ denotes a zero-matrix. The matrix \mathbf{F} (\mathbf{F}^{H}) is the $N \times N$ FFT (IFFT) matrix. The insertion of the CP is fulfilled by the matrix

$$\mathbf{M} = \begin{bmatrix} \mathbf{0}_{N_{\text{g}} \times (N - N_{\text{g}})} & \mathbf{I}_{N_{\text{g}}} \\ & \mathbf{I}_N \end{bmatrix}_{(N + N_{\text{g}}) \times N} \quad (2.23)$$

where N_{g} denotes the CP length.

The convolution in the time domain is described as a Toeplitz matrix composed by the channel coefficients in Equation (2.17), given as

$$\mathbf{H}^{(\text{toep})} = \begin{bmatrix} c_0 & 0 & \cdots & \cdots & 0 \\ c_1 & c_0 & 0 & \cdots & 0 \\ \vdots & \ddots & \ddots & \ddots & \vdots \\ \vdots & \ddots & \ddots & \ddots & \vdots \\ 0 & \ddots & 0 & c_L & c_{L-1} \\ 0 & \cdots & \cdots & 0 & c_L \end{bmatrix}, \quad (2.24)$$

which has a dimension of $(N + N_{\text{g}} + L) \times (N + N_{\text{g}})$.

The timing synchronization on the receiver side determines the boundary of the FFT windows, as shown in Figure 2.4. This can be described by the two windowing matrices $\mathbf{W}(\theta)$ and $\mathbf{W}^{\text{ISI}}(\theta)$ of size $N \times (N + N_{\text{g}} + L)$. In the ideal symbol timing case, i.e., $\theta = 0$,

$$\mathbf{W}(\theta)|_{\theta=0} = \begin{bmatrix} \mathbf{0}_{N \times N_{\text{g}}} & \mathbf{I}_{N \times N} & \mathbf{0}_{N \times L} \end{bmatrix}, \quad \mathbf{W}^{\text{ISI}}|_{\theta=0} = \mathbf{0}_{N \times (N + N_{\text{g}} + L)}. \quad (2.25)$$

Afterwards, an FFT is applied to the truncated signal part. Then, the guard bands are discarded by applying the matrix \mathbf{P}^{H} .

Till here, we have shown how the transfer functions $\mathbf{A}(\theta)$ and $\mathbf{B}(\theta)$ are constructed step by step. In case of ideal symbol timing ($\theta = 0$), transfer matrix $\mathbf{A}(\theta)$ becomes diagonal and matrix $\mathbf{B}(\theta)$ all-zero. In this case, neither ICI nor ISI occurs. Com-

pared to [12], this model allows a straightforward modeling of symbol timing errors, where merely the windowing matrices $\mathbf{W}(\theta)$ and $\mathbf{W}^{\text{ISI}}(\theta)$ are dependent on the STO θ . We distinguish two cases, namely an STO to the right (late timing) and an STO to the left (early timing), as illustrated in Figure 2.4.

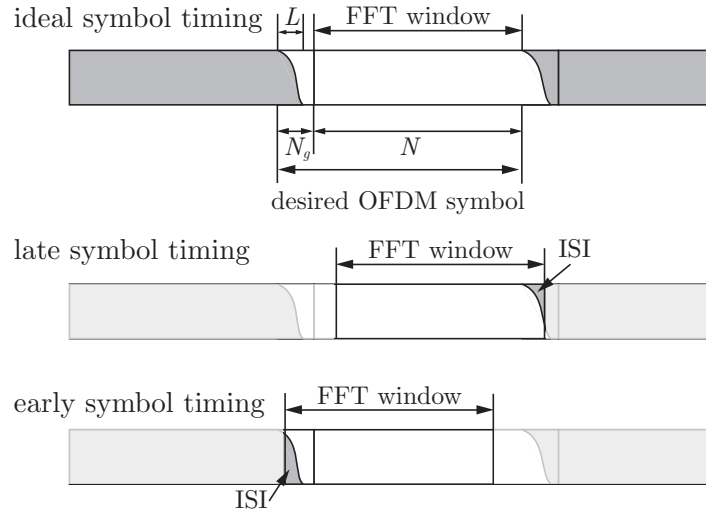


Figure 2.4: A received OFDM symbol sequence through a time dispersive channel under ideal/imperfect symbol timing.

- STO to the right ($\theta < 0$), late timing

As shown in Figure 2.4, in the late timing case, the FFT window is shifted to the right and takes in the interference from the successive OFDM symbol. Such a process can be modeled by applying

$$\mathbf{W}(\theta) = \begin{bmatrix} \mathbf{0}_{N \times (N_g - \theta)} & \mathbf{I}_{N \times N} & \mathbf{0}_{N \times (L + \theta)} \end{bmatrix}_{N \times (N + N_g + L)}, \quad (2.26)$$

$$\mathbf{W}^{\text{ISI}}(\theta) = \begin{bmatrix} \mathbf{0} & \mathbf{0} \\ \mathbf{I}_{(-\theta) \times (-\theta)} & \mathbf{0} \end{bmatrix}_{N \times (N + N_g + L)} \quad (2.27)$$

to Equations (2.19) and (2.20).

- STO to the left ($\theta > N_g - L$), early timing

When an early symbol timing occurs, the FFT window is shifted to the left. No interference is induced unless the FFT window embraces the tail of the previous OFDM symbol. Otherwise, there are $d = \theta + L - N_g$ samples in the desired OFDM symbol which are corrupted by the previous one. Similarly, this can be modeled by applying $\mathbf{W}(\theta)$ in Equation (2.26) and

$$\mathbf{W}^{\text{ISI}}(\theta) = \begin{bmatrix} \mathbf{0} & \mathbf{I}_{d \times d} \\ \mathbf{0} & \mathbf{0} \end{bmatrix}_{N \times (N + N_g + L)}. \quad (2.28)$$

Let matrices $\mathbf{A}^{(d)}(\theta)$ and $\mathbf{A}^{(o)}(\theta)$ contain the diagonal and off-diagonal elements in $\mathbf{A}(\theta)$, namely

$$\mathbf{A}^{(d)}(\theta) = \begin{bmatrix} a_{11} & 0 & \cdots & 0 \\ 0 & a_{22} & \ddots & \vdots \\ \vdots & \ddots & \ddots & 0 \\ 0 & \cdots & 0 & a_{N_{\text{tot}}N_{\text{tot}}} \end{bmatrix}, \quad (2.29)$$

$$\mathbf{A}^{(o)}(\theta) = \begin{bmatrix} 0 & a_{12} & \cdots & a_{1N_{\text{tot}}} \\ a_{21} & 0 & \ddots & \vdots \\ \vdots & \ddots & \ddots & a_{N_{\text{tot}}-1N_{\text{tot}}} \\ a_{N_{\text{tot}}1} & \cdots & a_{N_{\text{tot}}N_{\text{tot}}-1} & 0 \end{bmatrix}. \quad (2.30)$$

Thus, Equation (2.18) becomes

$$\mathbf{r}_l = \underbrace{\mathbf{A}^{(d)}(\theta)\mathbf{x}_l}_{\text{desired signal}} + \underbrace{\mathbf{A}^{(o)}(\theta)\mathbf{x}_l}_{\text{ICI}} + \underbrace{\mathbf{B}(\theta)\mathbf{x}_{\text{int}}}_{\text{ISI}} + \mathbf{v}_l \quad (2.31)$$

Similarly, we denote the entry on the i -th row and the j -th column of the matrix $\mathbf{B}(\theta)$ as b_{ij} . The received signal on an arbitrary subcarrier k can be expressed as

$$r_{l,k} = a_{kk}X_{l,k} + \underbrace{\sum_{p \neq k} a_{kp}X_{l,p}}_{\text{ICI}} + \underbrace{\sum_p b_{kp}X_{\text{int},p}}_{\text{ISI}} + V_{l,k}. \quad (2.32)$$

In fact, for a MIMO system where the multiple antennas are relatively closely deployed at the TX and RX, this model can be easily extended to an $N_R \times N_T$ case. Thus, the transfer functions $\mathbf{A}(\theta)$ and $\mathbf{B}(\theta)$ become block matrices:

$$\mathbf{A}(\theta) = \begin{bmatrix} \mathbf{A}_{11} & \cdots & \mathbf{A}_{1N_{\text{tot}}} \\ \vdots & \ddots & \vdots \\ \mathbf{A}_{N_{\text{tot}}1} & \cdots & \mathbf{A}_{N_{\text{tot}}N_{\text{tot}}} \end{bmatrix}, \quad \mathbf{B}(\theta) = \begin{bmatrix} \mathbf{B}_{11} & \cdots & \mathbf{B}_{1N_{\text{tot}}} \\ \vdots & \ddots & \vdots \\ \mathbf{B}_{N_{\text{tot}}1} & \cdots & \mathbf{B}_{N_{\text{tot}}N_{\text{tot}}} \end{bmatrix} \quad (2.33)$$

We therefore obtain a vector-matrix form for Equation (2.32) on subcarrier k , expressed as

$$\mathbf{r}_{l,k} = \mathbf{A}_{kk}\mathbf{x}_{l,k} + \underbrace{\sum_{p \neq k} \mathbf{A}_{kp}\mathbf{x}_{l,p}}_{\text{ICI}} + \underbrace{\sum_p \mathbf{B}_{kp}\mathbf{x}_{\text{int},p}}_{\text{ISI}} + \mathbf{v}_{l,k}, \quad (2.34)$$

where $\mathbf{r}_{l,k}$ ($\mathbf{v}_{l,k}$) denotes the $N_R \times 1$ received signal (noise) vector, $\mathbf{x}_{l,k}$ the $N_T \times 1$

transmitted signal vector. The transfer functions for subcarrier k are of dimension $N_R \times N_T$, given as

$$\mathbf{A}_{kk} = \begin{bmatrix} a_{kk}^{(1,1)} & \dots & a_{kk}^{(1,N_T)} \\ \vdots & \ddots & \vdots \\ a_{kk}^{(N_R,1)} & \dots & a_{kk}^{(N_R,N_T)} \end{bmatrix}, \mathbf{B}_{kp} = \begin{bmatrix} b_{kp}^{(1,1)} & \dots & b_{kp}^{(1,N_T)} \\ \vdots & \ddots & \vdots \\ b_{kp}^{(N_R,1)} & \dots & b_{kp}^{(N_R,N_T)} \end{bmatrix}. \quad (2.35)$$

2.3.2. Impact on Post-FFT SINR

An interference analysis concerning the STO has been provided in [12–14]. In this section, we present an equivalent analysis based on the previously introduced signal model. According to Section 2.2.2, the post-FFT SINR is chosen to be the metric that reflects the system distortion.

Given Equation (2.32) where the interference terms induced by the residual STO are identified, the power of the signal, the interferences and the noise terms at an arbitrary subcarrier k are calculated as

$$E_S = |a_{kk}|^2 \cdot \sigma_s^2, \quad (2.36)$$

$$E_I = \left(\sum_{p \neq k} |a_{kp}|^2 + \sum_p |b_{kp}|^2 \right) \cdot \sigma_s^2, \quad (2.37)$$

$$E_N = \sigma_v^2, \quad (2.38)$$

where $\sigma_s^2 = \mathbb{E}\{|X_{l,k}|^2\}$ and $\sigma_v^2 = \mathbb{E}\{|V_{l,k}|^2\}$. The effective SINR at this stage is given as

$$\text{SINR} = \frac{E_S}{E_I + E_N}. \quad (2.39)$$

In Figure 2.5, SINR curves are plotted for AWGN and ITU Pedestrian A/B channels [15]. When the maximum excess delay of the channel impulse response approaches the duration of the CP, the valid symbol timing region becomes accordingly shorter. In addition, an asymmetric degradation in the effective SINR can be observed for the time dispersive channels. Compared to the early timing where $\theta > 0$, a late timing, i.e., $\theta < 0$ causes a sharp drop in performance. Although STO is not a time-variant distortion, it can damage an OFDM system by introducing ICI and ISI as well.

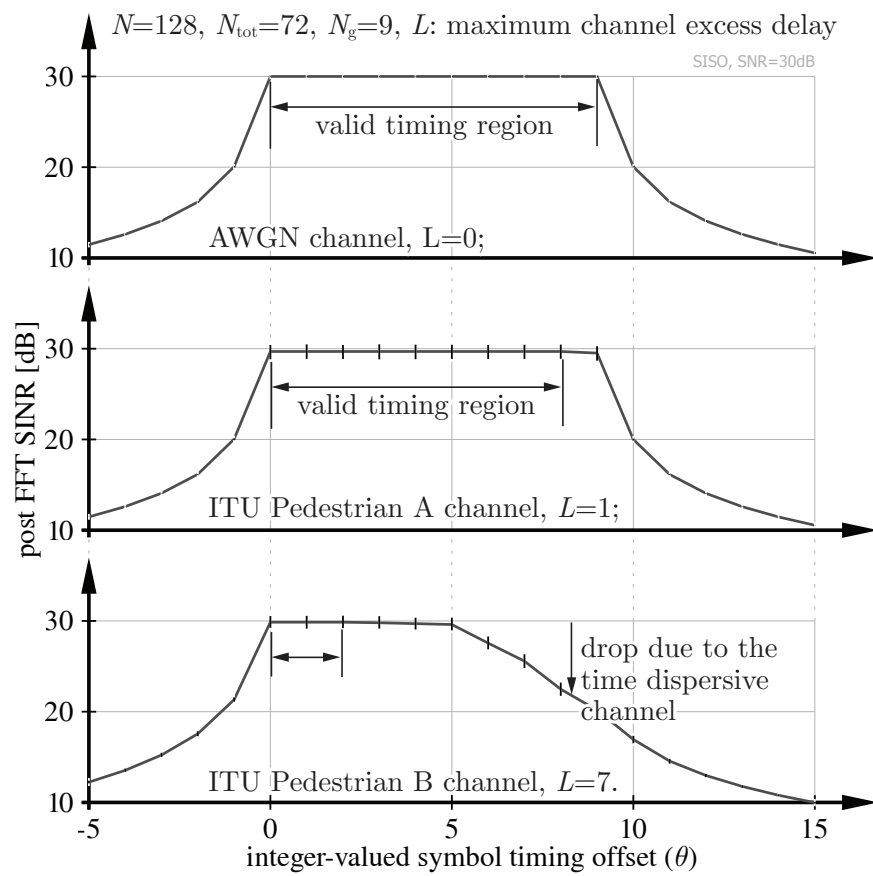


Figure 2.5: Calculated post-FFT SINRs in AWGN and ITU Pedestrian A/B channels at SNR = 30 dB ($N = 128, N_{\text{tot}} = 72, N_g = 9, L$: maximum channel excess delay, vertical lines display the 95% confidence intervals).

3. Carrier Frequency Synchronization in WiMAX

This chapter investigates the carrier frequency synchronization in the context of the Orthogonal Frequency Division Multiplexing (OFDM) physical layer of Worldwide Inter-operability for Microwave Access (WiMAX). Starting with a brief introduction of the IEEE 802.16 protocol suite in Section 3.1, the carrier frequency synchronization procedure is elaborated in Section 3.2. Section 3.3 provides a performance evaluation in terms of the estimation error as well as the coded throughput from standard compliant simulations. Section 3.4 concludes the chapter.

3.1. WiMAX Introduction

WiMAX refers to inter-operable solutions based on the IEEE 802.16 family of standards, e.g., [1, 8]. It was designed to provide a broadband wireless alternative that is competitive to traditional wireline-access technologies. WiMAX far surpasses the wireless range of Wireless Local Area Network (WLAN) and is involved as a part of the fourth generation wireless communication technology.

Although WiMAX was originally approved in the form of Single Carrier (SC) for delivering high-speed connections to Line-of-Sight (LOS) businesses in December 2001, OFDM was introduced into the physical layer since 2003 in order to enable Non-Line-of-Sight (NLOS) deployments. Since this amendment, namely IEEE 802.16-2004 [1], OFDM has established itself as a method of choice for dealing with multi-path for broadband wireless communications. Afterwards, further revisions were made to accommodate high-speed mobility by supporting, for instance, scalable OFDM, adaptive antenna systems, capacity-approaching codes, i.e., Turbo codes and Low

Density Parity Check (LDPC) codes. These modifications made the physical layer of the so-called Mobile WiMAX standard [8] comparable to its major competitor the 3rd Generation Partnership Project (3GPP) Long Term Evolution (LTE) which was finalized in December 2008 [2].

WiMAX has three different physical layers defined according to IEEE 802.16-2009 [8], namely the SC [8, Section 8.1], the OFDM [8, Section 8.3] and Orthogonal Frequency Division Multiple Access (OFDMA) [8, Section 8.4]. The SC physical layer is designed for directional radio links with LOS, whereas the OFDM and the OFDMA physical layers are for NLOS conditions. At the time, based on IEEE 802.16-2004, the WiMAX forum defined two different system profiles: one based on the OFDM physical layer, called the fixed system profile; the other one based on the scalable OFDMA physical layer, called the mobility system profile [16].

Our investigation on the performance of a practical OFDM system started with the OFDM physical layer of WiMAX [17–20] where the potential performance of WiMAX was evaluated using a wireless radio testbed [21]. The construction of the Vienna MIMO Testbed ensures perfect timing and frequency synchronization between transmitter and receiver [22]. Therefore, the effects of imperfect synchronization on the throughput was not considered in the previous work.

In [1, 8], the synchronization procedure between a Base Station (BS) and a Subscriber Station (SS) is referred to as ranging. There are two types of ranging processes, namely initial ranging and periodic ranging. In this work, we consider the physical layer procedure of the initial ranging during (re)registration and when synchronization is lost.

3.1.1. Transmission Resource Structure

The OFDM physical layer of WiMAX supports a frame-based transmission. A frame consists of a Downlink (DL) subframe and an Uplink (UL) subframe. A DL subframe, as shown in Figure 3.1, consists of only one DL physical layer Protocol Data Unit (PDU). Each DL physical layer PDU starts with a long preamble which is used for physical layer synchronization. The preamble is followed by a one-OFDM-symbol long Frame Control Header (FCH) burst that contains control information. The FCH is followed by one or multiple DL bursts. Each DL burst consists of an integer number of OFDM symbols. A number of specific frame durations are allowed, varying from 2.5 ms to 20 ms. The specific frame duration is determined by the periodicity of the frame start preambles at the BS. However, once it is selected, it shall not be changed [8, Section 8.3.5]. In this work, we constrain to the shortest frame duration, namely 2.5 ms.

The OFDM physical layer of WiMAX utilizes 256 narrowband subcarriers, 200 of

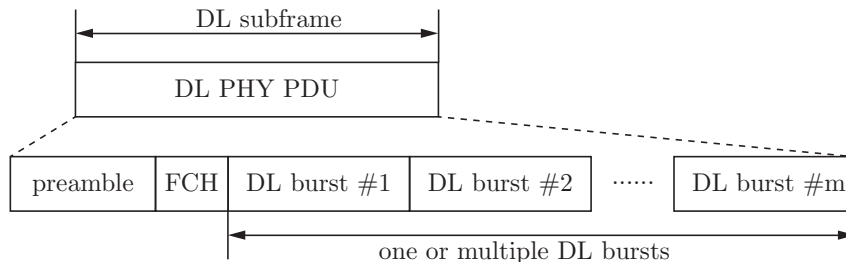


Figure 3.1: Frame structure in the OFDM physical layer of IEEE 802.16-2009 [8].

which carries modulated data symbols. Four different Cyclic Prefix (CP) lengths are allowed, although a CP of 64 samples is considered within this work.

3.1.2. Preambles and Pilots

The OFDM physical layer follows the frame structure specified in IEEE 802.16 [8] which implies the block fading assumption on a frame basis. As shown in Figure 3.1, each DL subframe starts with a preamble that consists of two consecutive OFDM symbols with regular length CPs. The preamble enables an SS to synchronize in timing and frequency to a BS. Additionally, there are eight subcarriers reserved as pilots.

The first OFDM symbol in the preamble, as shown in Figure 3.2, uses only subcarriers, the indices of which are multiples of four. As a result, the time domain waveform of the first symbol consists of four repetitions of 64-sample fragments, preceded by a CP. The second OFDM symbol utilizes only even subcarriers, resulting in a time domain structure which is composed of two repetitions of a 128-sample fragment, preceded by a CP. The combination of the two OFDM symbols are referred to as the long preamble [8].

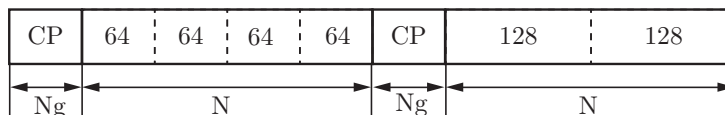


Figure 3.2: DL and network entry preamble structure in the OFDM physical layer of IEEE 802.16-2009 [8, Figure 207]. A repetitive structure can be found in the time domain.

In addition to the long preambles which is mainly used for initialization, the eight equi-spaced pilot subcarriers are inserted into each data burst in order to constitute the symbol. Binary Phase-Shift Keying (BPSK) modulation is utilized for the pilot symbols.

3.2. Synchronization Procedure in WiMAX

Designed for burst transmissions, a WiMAX DL transmission requires a synchronization procedure for initial registration. Such a procedure is repeated either periodically or when synchronization is lost. In this work, we assumed that a synchronization procedure is carried out at every received frame.

3.2.1. Related Work

The literature on timing and frequency synchronization in general OFDM systems falls into two categories: data-aided methods and non-data-aided methods. Data aided methods estimate the Carrier Frequency Offset (CFO) using periodically transmitted training symbols, where usually a repetitive pattern is required [23–26]. These methods can be applied to burst transmission protocols such as in WLAN (i.e., IEEE 802.11x) and in WiMAX standards (i.e., IEEE 802.16x) [27–31]. On the other hand, blind or non-data-aided methods [32–39] do not rely on dedicated training symbols. In [32] and [33], Maximum Likelihood (ML) CFO estimators were proposed for flat-fading and frequency selective fading channels. These two estimators exploit the redundancy of the CP in OFDM. In [34–36], subspace based estimators were presented based on the null subcarriers in an OFDM symbol. Other non-data-aided methods exploit either the cyclostationarity of the OFDM signal [37] or a kurtosis-type cost function [38].

3.2.2. CFO Estimation

The carrier frequency synchronization block is located prior to the demodulation of the OFDM symbols. Figure 3.3 provides an insight to this part. After a correct symbol timing is obtained, the received OFDM signal in the time domain is fed into the frequency synchronization block. A three-step carrier frequency offset estimation scheme is presented in this section. Following the philosophy outlined in [13, 25], this scheme consists of three steps processing, in either the time or the frequency domain, namely Fractional Frequency Offset (FFO) estimation, Integer Frequency Offset (IFO) estimation and Residual Frequency Offset (RFO) estimation. The relationship between the three parts can be expressed as

$$\hat{\epsilon}_{\text{CFO}} = \underbrace{\hat{\epsilon}_{\text{FFO}} + \hat{\epsilon}_{\text{RFO}}}_{\approx \epsilon_{\text{FFO}}} + \underbrace{\hat{\epsilon}_{\text{IFO}}}_{\approx \epsilon_{\text{IFO}}}, \quad (3.1)$$

where ϵ in general is the CFO in Hertz (Δf) normalized to the subcarrier spacing. Consider a 5 MHz bandwidth mode, the subcarrier spacing is derived as 22.5 kHz according to [8]. Therefore, within the scope of this chapter, there is $\epsilon = \Delta f / 22.5 \text{ kHz}$.

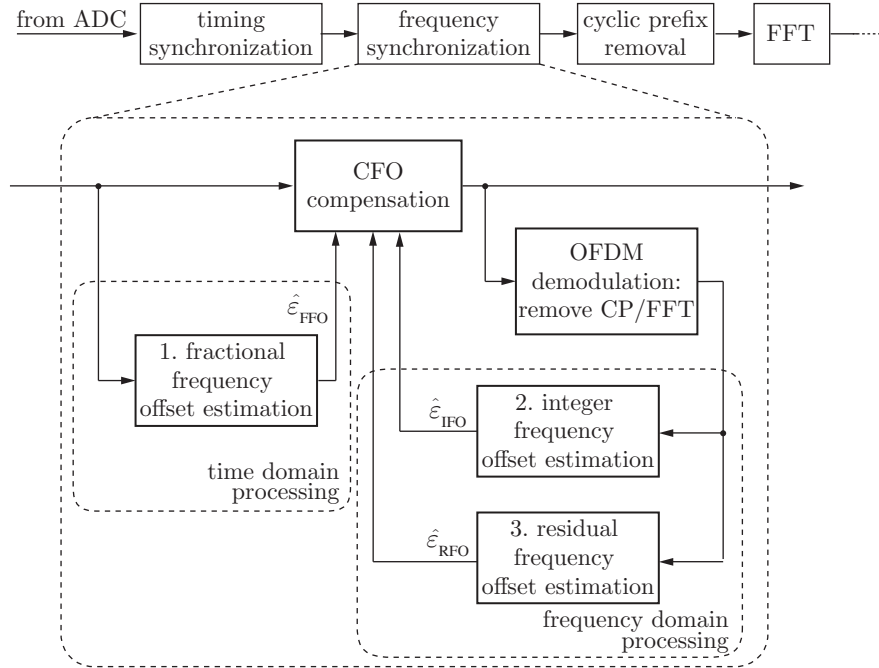


Figure 3.3: Carrier frequency synchronization block in an OFDM receiver.

As shown in Chapter 2, FFO causes the Inter-Carrier Interference (ICI). In order to provide a fast acquisition of the fractional part of the CFO, a pre-Fast Fourier Transform (FFT) algorithm is required. Afterwards, preambles and pilot symbols in the frequency domain are utilized to estimate the integer and the residual part. The FFO and IFO estimation are sometimes referred to as CFO acquisition or coarse estimation, whereas the RFO estimation is referred to as CFO tracking or fine estimation.

Fractional Frequency Offset (FFO) Estimation

This step provides an initial estimate of the FFO. Given the repetitive structure of the long preamble in Figure 3.2, the approach in [23] can be applied. Following the notation in Equation (2.4), an estimation of the FFO is obtained by extracting the phase difference between the two halves in the long preamble,

$$\hat{\epsilon}_{\text{FFO}} = -\frac{1}{\pi} \arg \left\{ \sum_{m=1}^{N_R} \sum_{l=0}^1 \sum_{n=-N_g}^{127} r_{l,n}^{(m)} r_{l,n+128}^{(m)*} \right\}, \quad (3.2)$$

where N_R denotes the number of receive antennas and N_g the length of the CP. The estimation performance of such an estimator in a non-time-dispersive channel

in terms of the Mean Squared Error (MSE) is given as

$$\begin{aligned} \text{MSE}_{\text{FFO}} &= \mathbb{E}\{|\varepsilon_{\text{FFO}} - \hat{\varepsilon}_{\text{FFO}}|^2\} = \frac{2\gamma_{\text{T}} + 1}{8\pi^2 N_{\text{R}}(128 + N_{\text{g}})\gamma_{\text{T}}^2} \\ &= \frac{1}{4\pi^2 N_{\text{R}}(128 + N_{\text{g}})\gamma_{\text{T}}} \quad \text{for large } \gamma_{\text{T}}, \end{aligned} \quad (3.3)$$

where $\gamma_{\text{T}} = \sigma_{\text{s}}^2 \sigma_{\text{h}}^2 / \sigma_{\text{v}}^2$ is the Signal to Noise Ratio (SNR) at the Receiver (RX) in the time domain. The derivation of this estimator is analogous that is shown in Appendix C.1. The estimation range of the FFO estimator is determined by the $\arg\{\cdot\}$ operation. Therefore, $\hat{\varepsilon}_{\text{FFO}}$ falls into the range $(-1, 1)$.

Integer Frequency Offset (IFO) Estimation

Authors in [23] proposed an IFO estimator which greatly extends the overall estimation range of the CFO estimation. Although the ICI is usually claimed to be the reason that degrades the system performance, a mismatch in subcarrier indices between Transmitter (TX) and RX destroys the transmission entirely. In order to align the subcarrier indices at the receiver to those at the transmitter, ε_{IFO} needs to be estimated in the frequency domain.

In [23], a method based on the differential information between two consecutive OFDM symbols was proposed. Later references improved this method by introducing some modifications based on the ML estimation technique [40–42]. These methods can be directly applied to the long preamble in the frequency domain. Given the first two OFDM symbols $l = 0, 1$ in a frame in the frequency domain, based on the notation in Equation (2.9), the IFO estimator is expressed as

$$\hat{\varepsilon}_{\text{IFO}} = \arg \max_s \left\{ \Re \left[e^{\frac{i2\pi s(N+N_{\text{g}})}{N}} \cdot \sum_{k \in \mathcal{K}} \left(R_{0,k+s}^{(1)} R_{1,k+s}^{(1)*} \right) \left(X_{0,k}^{(1)} X_{1,k}^{(1)*} \right)^* \right] \right\}, \quad (3.4)$$

where \mathcal{K} denotes the set of non-zero subcarrier indices in the second preamble. In other words, set \mathcal{K} consists of even subcarrier indices for $m = 1$. The estimation range of this estimator is determined by the search range s , in this work, $s \in [-100, -98, \dots, -2, 0, 2, \dots, 98, 100]$.

Although only even-integer-valued estimates are allowed, given the estimation range $(-1, 1)$ of the aforementioned FFO estimator, the combination of the two is capable of estimating an arbitrary real-valued ε_{CFO} . It is noticed that Equation (3.4) can merely be applied to the preamble transmitted from the first antenna. This is due to the fact that the first preamble ($l = 0$) only has training symbols on every fourth subcarriers. Since the second TX antenna transmits on odd subcarriers k in the

second OFDM symbol ($l = 1$), the cross-correlation $X_{0,k}^{(1)} X_{1,k}^{(1)*}$ in Equation (3.4) always results in a zero.

Residual Frequency Offset (RFO) Estimation

The OFDM physical layer in WiMAX targets for broadband wireless connections in a low mobility scenario. The frame structure is therefore adjusted correspondingly to such a quasi-static scenario. One example is that the frame duration can be configured, namely by increasing the length of the payload part in Figure 3.1, the signaling overhead can be reduced. Also, assuming the channel stays constant within one frame duration, the initial registration (synchronization) and channel estimation are carried out merely at the preamble. All these facts leave the system sensitive to time-variant distortions, e.g., CFO.

The estimation error of the FFO estimation leaves a residual CFO, referred to as RFO. Although it can be shown that the ICI caused by a small-valued RFO is negligible, as shown in Equation (2.9), it slowly induces a Common Phase Error (CPE) to the desired signal term. Such a distortion increases with the OFDM symbol index l within one frame. Therefore, it is necessary to estimate and compensate the RFO in the frequency domain [25, 28, 43].

This section investigates RFO estimation schemes based on the eight pilot subcarriers of WiMAX. We consider the differential estimation of the phase offset per pilot subcarrier, i.e., $\Phi(\varepsilon_{\text{CFO}}, l)$ in Equation (2.12), which is directly linked to the CFO. Differential Estimation is attractive because it does not require any channel knowledge, and is, hence, robust to channel estimation errors [44, 45].

Given a small-valued RFO, i.e., the resulting ICI is sufficiently small to be neglected and the subcarriers correctly aligned, the received signal on pilot symbol positions can be expressed as

$$\begin{aligned} R_{l,k}^{(m)} &= e^{i \frac{2\pi \varepsilon_{\text{RFO}} l (N + N_g)}{N}} \cdot X_{l,k}^{(q)} H_{l,k}^{(m,q)} + \tilde{V}_{l,k}^{(m)} \\ &= e^{i\phi \cdot l} \cdot X_{l,k}^{(q)} H_{l,k}^{(m,q)} + \tilde{V}_{l,k}^{(m)}, \quad m = 1, 2, \dots, N_R \end{aligned} \quad (3.5)$$

with

$$\phi = \frac{2\pi \varepsilon_{\text{RFO}} (N + N_g)}{N}. \quad (3.6)$$

If we observe the two pilot symbols on subcarrier k in the OFDM symbols l and

$l + d$, we obtain

$$\begin{aligned}
 W_{l,k}^{(m)} &= R_{l,k}^{(m)} R_{l+d,k}^{(m)*} \cdot \left(X_{l,k}^{(q)} X_{l+d,k}^{(q)*} \right)^* = \\
 &= e^{-i\phi \cdot d} \cdot |X_{l,k}^{(q)}|^2 |X_{l+d,k}^{(q)}|^2 |H_{l,k}^{(m,q)}|^2 + e^{i\phi \cdot l} \cdot |X_{l,k}^{(q)}|^2 X_{l+d,k}^{(q)} H_{l,k}^{(m,q)} \tilde{V}_{l+d,k}^{(m)*} + \\
 &+ e^{-i\phi \cdot (l+d)} \cdot |X_{l+d,k}^{(q)}|^2 X_{l,k}^{(q)*} H_{l,k}^{(m,q)*} \tilde{V}_{l,k}^{(m)} + \tilde{V}_{l,k}^{(m)} \tilde{V}_{l+d,k}^{(m)*} \cdot \left(X_{l,k}^{(q)} X_{l+d,k}^{(q)*} \right)^* \quad (3.7) \\
 & \quad \quad \quad l \in [0, N_f - d - 1], k \in \mathcal{K}_p,
 \end{aligned}$$

where \mathcal{K}_p represents the set of pilot subcarrier indices. Here, the block fading assumption holds, that is, the channel coherence time is greater than the frame duration. This implies that $H_{l,k}^{(m,q)} = H_{l+d,k}^{(m,q)}$. A RFO estimator can be expressed as

$$\hat{\varepsilon}_{\text{RFO}} = -\frac{1}{2\pi} \frac{N}{d \cdot (N + N_g)} \cdot \arg \left\{ \sum_m \sum_{l=0}^{N_f-d-1} \sum_{k \in \mathcal{K}_p} W_{l,k}^{(m)} \right\}. \quad (3.8)$$

The MSE at this stage is

$$\text{MSE}_{\text{RFO}}(d) = \frac{N^2}{4\pi^2 (N + N_g)^2 N_R N_p \cdot (N_f - d) \cdot d^2} \cdot \frac{1}{\gamma_F}, \quad (3.9)$$

where N_p denotes the number of pilot subcarriers, N_R the number of RX antennas and N_f the number of OFDM symbols in one frame. The average received SNR $\gamma_F = \sigma_h^2 \sigma_s^2 / \sigma_v^2$. A detailed derivation of the MSE_{RFO} is found in Appendix A. Given the pilot symbols available on the eight pilot subcarriers in the N_f OFDM symbols in one frame, the MSE can be minimized by

$$\begin{aligned}
 &\text{maximize} && (N_f - d) \cdot d^2, \\
 &\text{subject to} && 0 < d \leq N_f - 1, d \in \mathbb{Z}
 \end{aligned} \quad (3.10)$$

When $N_f = 44$, $d_{\text{opt}} = 29$ is obtained, leading to

$$\text{MSE}_{\text{RFO}}(d_{\text{opt}}) = \frac{N^2}{4\pi^2 (N + N_g)^2 N_R N_p \cdot 15 \cdot 29^2} \cdot \frac{1}{\gamma_F}, \quad (3.11)$$

In Appendix B, the Cramér-Rao Lower Bound (CRLB) of the RFO estimation based on the pilot subcarriers is derived. It is later shown by simulation that Equation (3.11) approaches the CRLB. In addition, the estimation range of the estimator is constrained by the argument operation, namely

$$\hat{\varepsilon}_{\text{RFO}} \in \left(-\frac{N}{2\pi d(N + N_g)}, \frac{N}{2\pi d(N + N_g)} \right). \quad (3.12)$$

Robust RFO Estimation

Equation (3.12) implies that the estimation range of the RFO estimator in Equation (3.8) is dependent on the factor d . An optimal value d_{opt} that minimizes the MSE may in turn shrink the estimation range. In a time-dispersive channel, the performance of an FFO estimation in the time domain is usually limited. Therefore, an RFO estimator of a small estimation range increases the probability that an overflow occurs. In order to obtain an estimator that is robust to the overflow issue, an RFO estimator with a fixed estimation range is proposed. We modify Equation (3.7) to be

$$\bar{W}_{l,k}^{(m)} = \sum_l^{l+N_f-d-1} \left(R_{l,k}^{(m)} X_{l,k}^{(q)*} \right) \cdot \sum_l^{l+N_f-d-1} \left(R_{l+1,k}^{(m)} X_{l+1,k}^{(q)*} \right)^* . \quad (3.13)$$

The differential estimator in Equation (3.8) thus becomes

$$\hat{\epsilon}'_{\text{RFO}} = -\frac{1}{2\pi} \frac{N}{(N + N_g)} \cdot \arg \left\{ \sum_m \sum_{l=0}^{d-1} \sum_{k \in \mathcal{K}_p} \bar{W}_{l,k}^{(m)} \right\} . \quad (3.14)$$

Such a modification is illustrated in Figure 3.4. Instead of obtaining a phase difference of two blocks that are d OFDM symbols apart, the robust alternative calculates the phase difference at each step. Such a procedure guarantees a fixed estimation range of

$$\hat{\epsilon}_{\text{RFO}} \in \left(-\frac{N}{2\pi(N + N_g)}, \frac{N}{2\pi(N + N_g)} \right) , \quad (3.15)$$

which is independent of the value of d . Therefore, it is capable of reducing the overflow probability at the lower SNR region and in the meanwhile achieves an equal estimation performance for the high SNRs.

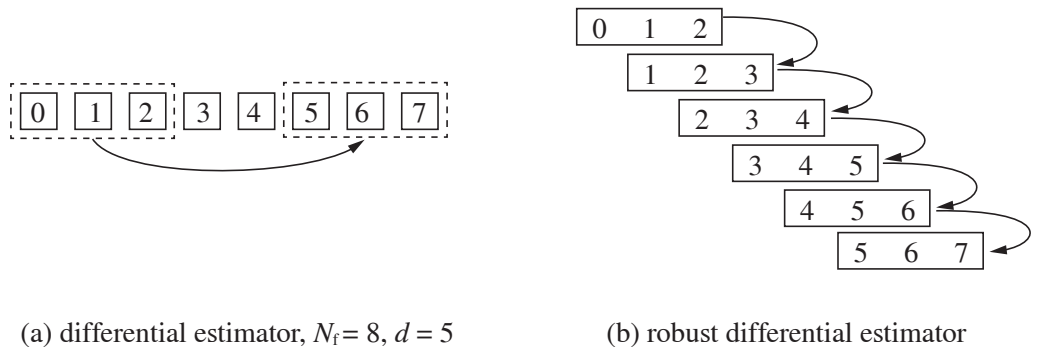


Figure 3.4: The two differential RFO estimators.

Table 3.1.: Simulation parameters for performance evaluation in WiMAX.

Parameter	Value
Channel bandwidth	5 MHz
Frame duration	2.5 ms
FFT size (N)	256
No. data subcarriers (N_{tot})	192
No. pilot subcarriers (N_{p})	8
Subcarrier spacing	22.5 kHz
CP length (N_{g})	64
No. OFDM symbols per frame (N_{f})	44
Transmission setting $N_{\text{R}} \times N_{\text{T}}$	1×1
Channel model	AWGN, Pedestrian B [15]
CFO introduced (ε_{CFO})	$\pi - 4 = -0.8584 \dots$ subcarrier spacing
Channel knowledge	perfect
Channel coding	Reed-Solomon convolutional code
Modulation scheme	Table 3.2

Table 3.2.: The coding rates and modulation alphabets of the seven WiMAX AMC schemes. All values are calculated for a frame size of 44 OFDM data symbols transmitted in a frame duration of 2.5 ms and a channel bandwidth of 5 MHz.

AMC	Data bits	Modulation	Coding Rate	Max. Throughput
1	4224	2-PAM	1/2	1.69 Mbit/s
2	8448	4-QAM	1/2	3.38 Mbit/s
3	12672	4-QAM	3/4	5.07 Mbit/s
4	16896	16-QAM	1/2	6.76 Mbit/s
5	25344	16-QAM	3/4	10.14 Mbit/s
6	33792	64-QAM	2/3	13.52 Mbit/s
7	38016	64-QAM	3/4	15.21 Mbit/s

3.3. Numerical Results

The performance evaluation in this section was carried out using a WiMAX simulator which is an MATLAB implementation of the OFDM physical layer [6]. Relevant simulation parameters are listed in Table 3.1 and Table 3.2.

3.3.1. Estimation Performance

The estimation performance of the aforementioned FFO and RFO estimators are evaluated in terms of MSE in an Additive White Gaussian Noise (AWGN) as well as a time dispersive, i.e., frequency selective channel, namely ITU Pedestrian B, shown in Figure 3.5. Since the FFO is estimated merely based on the received signal in the time domain, a saturation can be observed in the estimation error for the time dispersive channel case. The increased estimation error in the first stage loads the

burden to the RFO estimation. Therefore, an RFO estimator with a relatively large estimation range is preferred especially in the time dispersive channel.

Also in Figure 3.5, the MSE curves of the modified differential estimator are plotted. Even though $d = 43$ is suboptimal, the RFO estimation improves the FFO estimation by 2 ~ 3 orders for the AWGN as well as the frequency selective channel ITU Pedestrian B. The curves obtained from simulations agree well with those from the calculation using Equation (3.3) and Equation (3.9).

The improvement from using the robust differential estimator for the RFO is presented in Figure 3.6. An optimal choice of d that minimizes the estimation error is applied. In the low SNR regions, overflows can be observed for both cases. Compared to the original differential estimator which exhibits overflows for an SNR lower than 12 dB, the robust alternative shifts such an effect to 6 dB. This guarantees the performance in the medium SNR region, namely 10 ~ 15 dB, which is the common situation in reality. In addition, by roughly comparing the RFO curves in Figure 3.5 and Figure 3.6, it can be observed that an optimal choice $d_{\text{opt}} = 29$ improves the estimation performance in terms of the MSE by yet another order. Moreover, with the optimal choice of d , the MSE asymptotically approaches the CRLB calculated in Appendix B in the high SNR region.

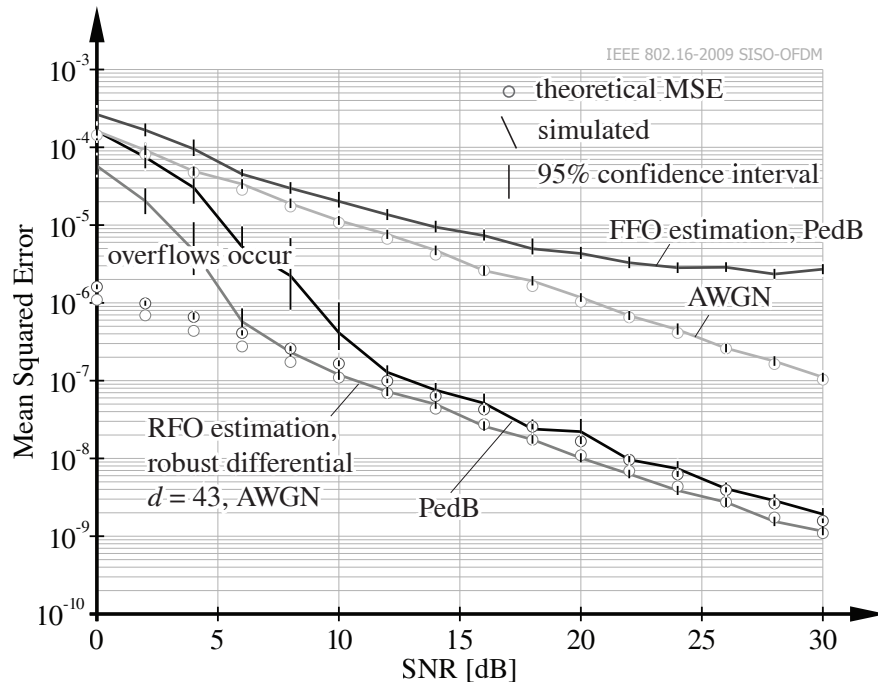


Figure 3.5: The estimation performance of the FFO and the RFO estimators in AWGN and ITU Pedestrian B channels, a suboptimal $d = 43$, averaged over 500 estimates.

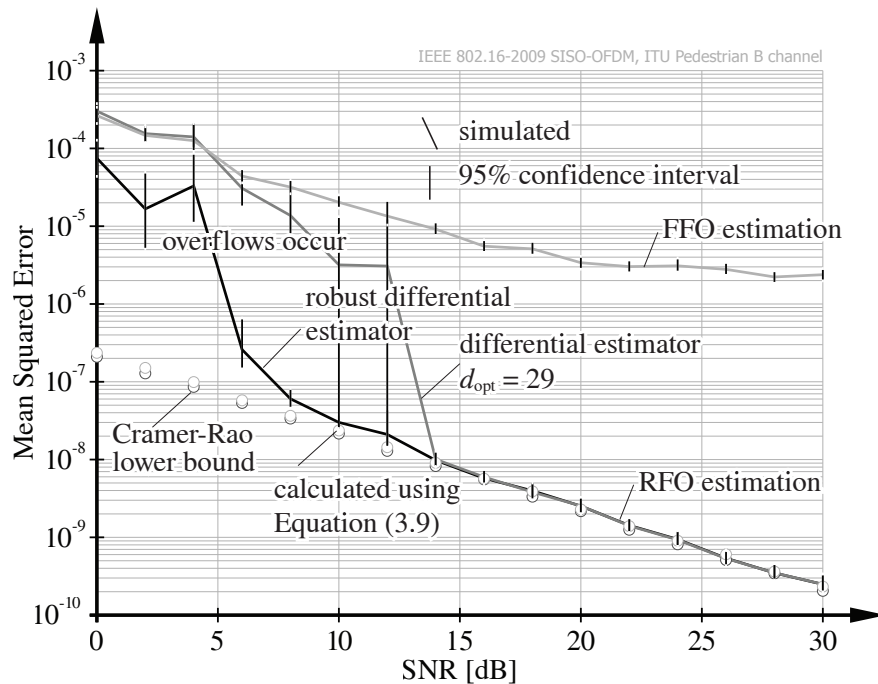


Figure 3.6: The estimation performance of the differential RFO estimator and the robust differential estimator in ITU Pedestrian B channels, an optimal $d_{opt} = 29$, averaged over 500 estimates.

3.3.2. Coded Throughput

Usually, an investigation on the CFO estimation performance stops at the MSE evaluation. However, for a communications system in practice, the metric of interests for the physical layer is eventually the coded throughput. For CFO estimation, it is not the 'best' estimator that is needed but a sufficient one. Therefore, a coded throughput simulation was carried out.

In the throughput simulation, the AMC is implemented by enforcing an optimal feedback. We transmitted 2000 frames over 2000 ITU Pedestrian B channel realizations at each SNR level using all seven Modulation and Coding Schemes (MCSs). Afterwards, the MCS which delivers the highest throughput is chosen for each channel realization. The total throughput is an average over the 2000 "maxima". As a reference, we chose the system without CFO. The resulting curves are shown in Figure 3.7.

For the coded throughput curves in the upper figure, the differences between the ideally synchronized case and the CFO compensated cases are hardly visible. In the lower figure, the throughput losses due to the imperfect carrier frequency synchronization are plotted. The robust differential RFO estimator reduces the relative throughput loss in the low SNR region significantly compared to the original ap-

proach.

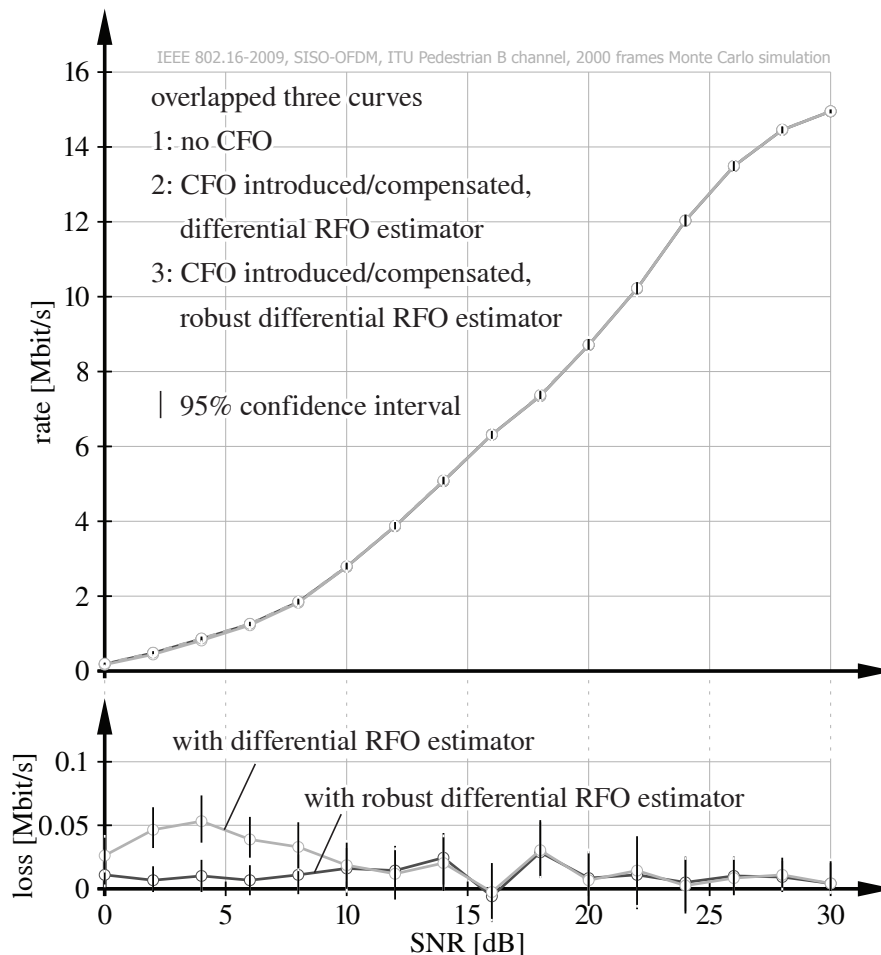


Figure 3.7: The coded throughput of the WiMAX OFDM physical layer in ITU Pedestrian B channel, 2000 frames Monte Carlo simulation.

3.4. Conclusion

In this chapter, we studied the carrier frequency synchronization issue in the context of the WiMAX OFDM physical layer. A three-step CFO estimation/compensation scheme was implemented in a MATLAB based standard compliant simulator. The throughput evaluation shows that such a compensation scheme successfully compensates the performance loss from a CFO. Although plenty of sophisticated RFO tracking schemes are found in literature, it is shown that a simple differential estimator provides sufficient estimation performance as well as an estimation range which allows operation in deep frequency selective scenarios.

From the evaluation methodology point of view, although a large improvement is obtained in the estimation performance in terms of the MSE when comparing the

two CFO tracking schemes, the difference becomes negligible when it corresponds to the system performance in terms of the coded throughput. This suggests that MSE should not be used as the only criterion when designing/evaluating a synchronization scheme for a practical wireless communication system, because it does not sufficiently reflect the reality. Instead, a thorough evaluation approach including the coded throughput is required.

As time proceeds, the general research focus has been shifted to an OFDMA physical layer which has more flexibility, for instance, scalable bandwidth, multi-user scheduling in the frequency and spatial dimension. Also, a different pilot symbol pattern which better supports a mobile scenario is adopted. Since the OFDMA physical layer of WiMAX is fairly comparable to that of the 3GPP LTE, the further investigation is continued in the latter.

In the next chapter, the influence of the CFO on the link performance of LTE downlink is evaluated in terms of the post-equalization Signal to Interference-plus-Noise Ratio (SINR) which determines the achievable throughput eventually. As most of the presented work on WiMAX was performed first, the coded throughput evaluation is constrained to MATLAB based simulations. The analytical approach in the next chapter may also be applicable for WiMAX.

4. LTE Performance under Carrier Frequency Offset (CFO)

This chapter discusses carrier frequency synchronization related issues in the context of Long Term Evolution (LTE) downlink. Section 4.1 presents aspects in the LTE downlink that are related to this work. Section 4.2 briefly introduces the three-step Carrier Frequency Offset (CFO) estimation scheme which has been presented in [46]. A detailed derivation of the involved estimators can be found in Appendix C. Section 4.3 provides a thorough performance evaluation, from the estimation performance of the CFO estimators, an analytical post-equalization Signal to Interference-plus-Noise Ratio (SINR) model under residual CFOs, to the theoretical loss in the coded throughput due to the CFO. Section 4.4 concludes this chapter.

4.1. LTE Introduction

The LTE physical layer as defined in [9], is based on Orthogonal Frequency Division Multiplexing (OFDM) with a Cyclic Prefix (CP) in the Downlink (DL), and on Single-Carrier Frequency Division Multiple Access (SC-FDMA) with a CP in the Uplink (UL). Two duplex modes, namely Frequency Division Duplex (FDD) and Time Division Duplex (TDD), are supported, enabling transmission in a paired and an unpaired spectrum.

By converting a wide band frequency selective channel into a set of flat fading subchannels, such systems allow for flexible frequency domain scheduling, typically trying to assign only 'good' subchannels to the individual users [47]. Referred to as Orthogonal Frequency Division Multiple Access (OFDMA), such a technique

offers a dramatic gain in terms of cell throughput. In addition, with multiple antenna techniques, such as transmit diversity, spatial multiplexing with appropriate precoding/beamforming, LTE’s target peak data rate was set by the standard to 100 Mbit/s for the DL and 50 Mbit/s for the UL [48]. However, LTE also inherits the drawback of OFDM, vulnerable to time variant distortions such as Carrier Frequency Offset (CFO), sampling frequency offset, phase noise and Doppler spread which destroy the orthogonality between subchannels and introduce Inter-Carrier Interference (ICI). Given an increasing demand on the system performance, these impairments have come to be critical issues.

4.1.1. Transmission Resource Structure

The transmission resources in LTE downlink can be identified in three dimensions: time, frequency and space. The spatial dimension is referred to as ‘layer’ which is accessed by means of multiple antenna transmission and reception.

In the time dimension, radio frames have a duration of $T_{\text{frame}} = 10$ ms. Each frame is subdivided into 10 subframes of equal length. Each subframe contains two 0.5 ms slots. With normal CP, one slot typically consists of seven OFDM symbols (six if with extended CP). Focusing on the FDD mode, the frame structure is shown in Figure 4.1.

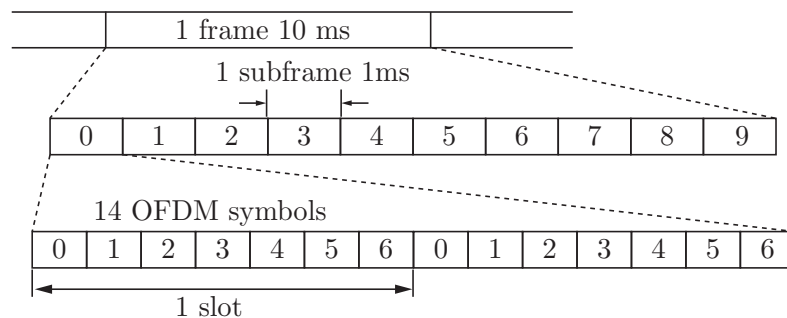


Figure 4.1: LTE frame structure in FDD mode (normal CP).

In the frequency domain, the available bandwidth is divided into equally spaced orthogonal subcarriers. A typical subcarrier spacing is 15 kHz [9]. The smallest unit of resources is the so-called Resource Element (RE) which consists of one subcarrier in one OFDM symbol. REs in a time-frequency grid of 12 subcarriers over a slot duration of 0.5 ms are grouped as a Resource Block (RB). The DL transmission bandwidth can be configured in the cell by adjusting the number of RBs ($N_{\text{RB}}^{\text{DL}}$). The available channel bandwidth and corresponding $N_{\text{RB}}^{\text{DL}}$ are listed in Table 4.1.

Table 4.1.: Available LTE channel bandwidths and available resource blocks [49].

channel bandwidth B_{channel} [MHz]	1.4	3	5	10	15	20
transmission bandwidth configuration $N_{\text{RB}}^{\text{DL}}$	6	15	25	50	75	100
number of subcarriers	72	180	300	600	900	1200
FFT size	128	256	512	1024	1536	2048
bandguard size [% of B_{channel}]	23%	10%	10%	10%	10%	10%

4.1.2. Reference Signals

As specified in [9], cell-specific Reference Signals (RSs) are transmitted in all down-link subframes. Often referred to as common RSs, cell-specific RS are available for all User Equipments (UEs) in a cell to estimate their channel state information.

Cell-specific RSs utilize Quadrature Amplitude Modulation (QAM) modulated symbol alphabets, supporting up to four antenna transmission. The arrangement follows an equidistant principle in the time-frequency lattice structure. The mapping is configured by antenna ports, shown in Figure 4.2. For one, two and four antenna transmission, antenna ports $\{0\}$, $\{0, 1\}$ and $\{0, 1, 2, 3\}$ are used, respectively. RSs from different Transmitter (TX) antennas are separated in time and frequency, which ensures their orthogonality.

4.1.3. Synchronization Signals

The LTE standard defines two synchronization signals, namely the Primary Synchronization Signal (PSS) and the Secondary Synchronization Signal (SSS) [9]. In FDD mode, these signals are located on the 62 subcarriers symmetrically arranged around the DC-carrier, shown in Figure 4.3.

Specifically, the two PSSs in one frame are identical and constructed from a frequency domain Zadoff-Chu sequence [50, 51]. While the two SSS are different and based on maximum length sequences, known as M-sequences. They are chosen for certain benefits, such as a good periodic autocorrelation or cross-correlation property, a constant amplitude (PSS) or being spectrally flat (SSS) and so on. These two synchronization signals are utilized mainly for the initial synchronization where basic system parameters as well as the frame timing are identified. Therefore, they are designed to be robust to a CFO up to ± 7.5 kHz [52].

4.2. Carrier Frequency Offset (CFO) Estimation

The CFO estimation in LTE follows a similar three-step procedure shown in Figure 3.3. Since the LTE DL utilizes a fixed subcarrier spacing of 15 kHz, intuitively

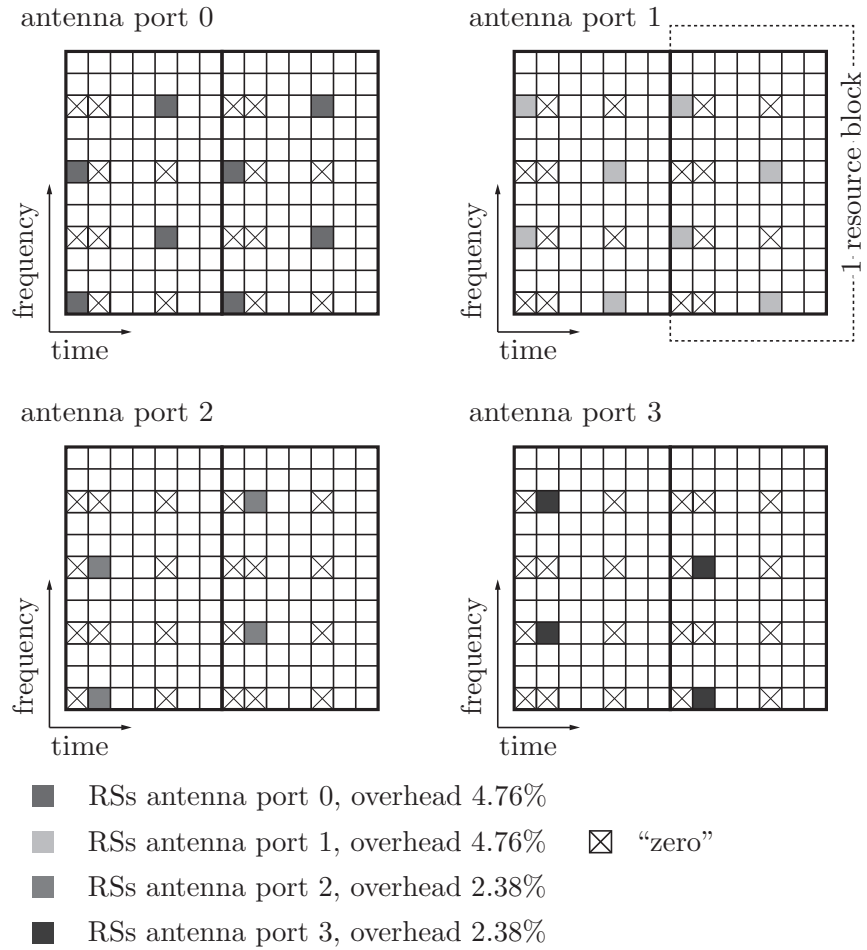


Figure 4.2: RSs mapping for antenna port {0,1,2,3}.

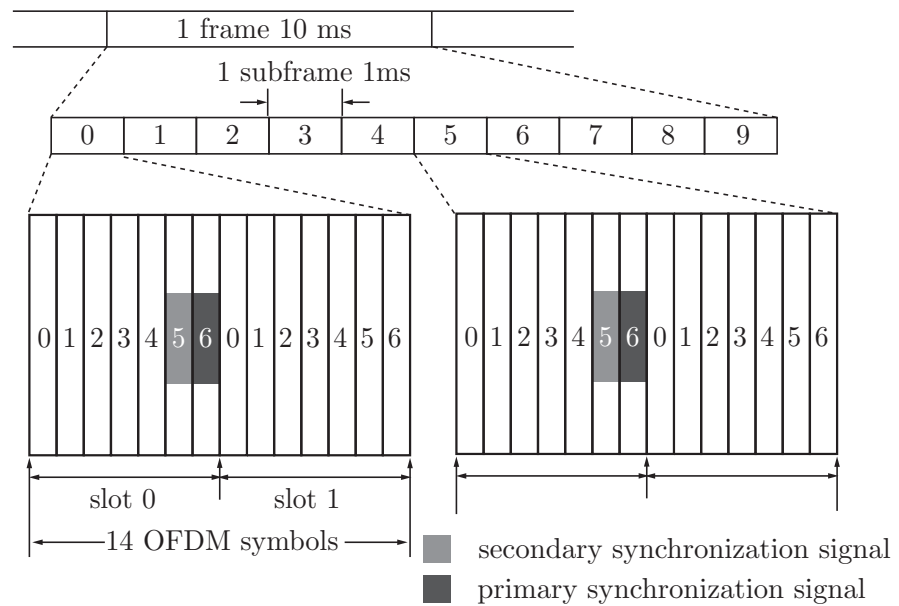


Figure 4.3: Synchronization signals in LTE FDD downlink.

it is more sensitive to a CFO than the OFDM physical layer in Worldwide Interoperability for Microwave Access (WiMAX). In this chapter, a CFO estimation scheme from [46] based on the physical signals and reference signals in LTE is presented.

Fractional Frequency Offset (FFO) Estimation

Unlike WiMAX, LTE does not have preambles with repetitive pattern defined, therefore data-aided estimation cannot be applied. Throughout the literatures, FFO estimation is carried out jointly with the symbol timing offset estimation [23, 26, 32, 33, 37]. Once the symbol timing is obtained, FFO estimation based on the Maximum Likelihood (ML) principle can be applied. In [32], a blind estimator is derived using the duplicative property of the CP. In the context of the block fading assumption where the channel coherence time is greater than one subframe duration (1 ms), this method can be extended to

$$\hat{\varepsilon}_{\text{FFO}} = -\frac{1}{2\pi} \arg \left\{ \sum_{m=1}^{N_R} \sum_{l=0}^{N_f-1} \sum_{n=-N_g}^{-1} r_{l,n}^{(m)} r_{l,n+N}^{(m)*} \right\}, \quad (4.1)$$

where N_R denotes the number of receive antennas, N_f the number of OFDM symbols in one subframe, and N_g the CP length. The estimation range (normalized to the subcarrier spacing) of this stage is $(-0.5, 0.5)$, which is determined by the $\arg\{\cdot\}$ operation. A detailed derivation of Equation (4.1) can be found in Appendix C.

Integer Frequency Offset (IFO) Estimation

Similar to that in Equation (3.3), the IFO estimation technique [40–42] based on the ML estimation technique can be applied to LTE as well, given the Primary Synchronization Signal (PSS) and the SSS located in two consecutive OFDM symbols.

After the first stage, it can be assumed that the FFO has been mostly compensated. Knowing that identical synchronization signals are transmitted from all transmit antennas, according to Equation (2.9), the received SSS and PSS become

$$R_{\text{SSS},k}^{(m)} = e^{i\frac{2\pi\varepsilon_{\text{IFO}}l(N+N_g)}{N}} \cdot X_{\text{SSS},k-\varepsilon_{\text{IFO}}} \sum_{q=1}^{N_T} H_{\text{SSS},k-\varepsilon_{\text{IFO}}}^{(m,q)} + \tilde{V}_{\text{SSS},k}^{(m)}, \quad (4.2)$$

$$R_{\text{PSS},k}^{(m)} = e^{i\frac{2\pi\varepsilon_{\text{IFO}}(l+1)(N+N_g)}{N}} \cdot X_{\text{PSS},k-\varepsilon_{\text{IFO}}} \sum_{q=1}^{N_T} H_{\text{PSS},k-\varepsilon_{\text{IFO}}}^{(m,q)} + \tilde{V}_{\text{PSS},k}^{(m)}. \quad (4.3)$$

Here, subscripts SSS and PSS denote the corresponding OFDM symbol indices. Based on the transmitted and received synchronization signals, the ML estimator

for ε_{IFO} can be derived as (for the full derivation, see Appendix C.2)

$$\hat{\varepsilon}_{\text{IFO}} = \arg \max_s \left\{ \Re \left[e^{\frac{i2\pi s(N+N_g)}{N}} \cdot \sum_{m=1}^{N_R} \sum_{k \in \mathcal{K}_{\text{sync}}} \left(R_{\text{SSS},k+s}^{(m)} R_{\text{PSS},k+s}^{(m)*} \right) (X_{\text{SSS},k} X_{\text{PSS},k}^*)^* \right] \right\}, \quad (4.4)$$

where $\Re\{\cdot\}$ returns the real part of the argument and $s \in (-31, 31)$ corresponds to the set of potential integer offsets that can be estimated. This set is determined by the length of the synchronization signals in LTE. Set $\mathcal{K}_{\text{sync}}$ represents the subcarrier indices that are occupied by the synchronization signals. Note that due to the fact that in LTE the synchronization signals only exist in every fifth subframe, ε_{IFO} can only be estimated in these subframes.

Residual Frequency Offset (RFO) Estimation

As shown in Section 4.1.2, LTE has the advantage that the cell-specific reference signals from different transmit antennas do not overlap with each other. If one RE is reserved for the reference signals, there is only one antenna that transmits the reference signal while all others keep silence by sending zeros. This has been shown to be a robust design against channel characteristics [45, 53]. Also, it easily reduces the Multiple Input and Multiple Output (MIMO) processing to a Single Input and Single Output (SISO) case.

Similar to that in Equation (3.7), we observe the two reference signals on subcarrier k in the OFDM symbols l and $l + N_s$, leading to

$$\begin{aligned} W_{l,k}^{(m)} &= R_{l,k}^{(m)} R_{l+N_s,k}^{(m)*} \cdot \left(X_{l,k}^{(q)} X_{l+N_s,k}^{(q)*} \right)^* = \\ &= e^{-i \frac{2\pi \varepsilon_{\text{RFO}} N_s (N+N_g)}{N}} \cdot |X_{l,k}^{(q)}|^2 |X_{l+N_s,k}^{(q)}|^2 |H_{l,k}^{(m,q)}|^2, \quad m = 1, 2, \dots, N_R, \end{aligned} \quad (4.5)$$

where N_s is the number of OFDM symbols in one slot. Here, the block fading assumption holds, that is, the channel coherence time is greater than one subframe duration. This implies that $H_{l,k}^{(m,q)} = H_{l+N_s,k}^{(m,q)}$. The RFO can be estimated by applying the ML principle, as shown in Appendix C.3. The solution can be expressed as

$$\hat{\varepsilon}_{\text{RFO}} = -\frac{1}{2\pi} \frac{N}{N_s(N+N_g)} \cdot \arg \left\{ \sum_m \sum_{(k,l) \in \mathcal{K}_P} W_{l,k}^{(m)} \right\}. \quad (4.6)$$

The estimation is performed on a subframe basis with set \mathcal{K}_P corresponding to the joint set of the subcarrier and OFDM symbol indices on which the reference symbols

are located. Unlike in WiMAX, an LTE subframe has at most two RSs on each subcarrier, no freedom can be exploited in the time dimension. Also from Figure 4.2, it is noticed that the pair-wise reference signals $X_{l,k}^{(q)}$ and $X_{l+N_s,k}^{(q)}$ are only available for antenna port 0 and 1. The reference signals of antenna port 2 and 3 are not utilized in this case. Similar to the FFO estimation, the estimation range for ϵ_{RFO} is $(-N/[2N_s(N + N_g)], N/[2N_s(N + N_g)]) = (-0.0667, 0.0667)$.

4.3. Performance Evaluation

In most of the literature on frequency synchronization, as previously mentioned, the performance is evaluated in terms of the estimation error, in other words, the Mean Squared Error (MSE). However, the performance of a communication system is evaluated in terms of overall throughput. Therefore, not only the accuracy of the estimation is of interest, but more importantly, the impact of the estimation error on the overall throughput.

In the past decade, efforts have been made in evaluating the performance degradation caused by the CFO in terms of Bit Error Ratio (BER) or Symbol Error Ratio (SER) analytically [54–59]. Some authors considered the effect of CFO only and give analytical expressions in terms of uncoded BER for the Additive White Gaussian Noise (AWGN) channel [54–56]. This work was extended to frequency selective fading channels in [57]. The authors of [58, 59] further develop the calculation for uncoded BER and link capacity under the aggregate effect of time-variant impairments, namely CFO, imperfect channel knowledge and I/Q imbalance.

Throughout all these literature, either a perfect or an estimated channel knowledge at every OFDM symbol is assumed. Other aspects, e.g., frame structure and pilot symbol positions are not taken into account. In a practical communication system, namely LTE, taking into account the resource overhead, merely a subframe based channel knowledge is available, especially in a low mobility scenario. In this section, as illustrated in Figure 4.4, we try to include these practical aspects, step by step, and quantitatively expose the relationship between CFO, OFDM parameters and performance metrics such as CFO estimation error, post-equalization SINR and link capacity.

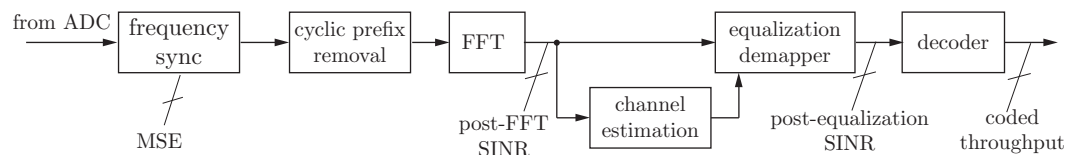


Figure 4.4: Evaluation positions in an LTE receive signal processing chain.

4.3.1. Estimation Performance

The estimation performance of previously introduced ML estimators are evaluated in this section. A theoretical MSE analysis provides the ideal capability of these estimators, which is compared to its theoretical lower bound. Afterwards, these analytical evaluation is confirmed by simulation results from the Vienna LTE Link Level simulator [60].

Theoretical Mean Squared Error (MSE) and Cramér-Rao Lower Bound (CRLB)

The estimation performance of the ε_{FFO} and the ε_{RFO} is expressed in terms of the MSE, given by

$$\text{MSE}_{\text{FFO}} = \mathbb{E}\{|\varepsilon_{\text{FFO}} - \hat{\varepsilon}_{\text{FFO}}|^2\} \quad (4.7)$$

and

$$\text{MSE}_{\text{RFO}} = \mathbb{E}\{|\varepsilon_{\text{FFO}} - \hat{\varepsilon}_{\text{FFO}} - \hat{\varepsilon}_{\text{RFO}}|^2\}. \quad (4.8)$$

Given the extended version of the ML estimator for FFO in Equation (4.1), the MSE can be derived as

$$\begin{aligned} \text{MSE}_{\text{FFO}} &= \frac{2\sigma_z^2\sigma_v^2 + \sigma_v^4}{8\pi^2 N_{\text{R}} N_{\text{f}} N_{\text{g}} \sigma_z^4} = \frac{2\gamma_{\text{T}} + 1}{8\pi^2 N_{\text{R}} N_{\text{f}} N_{\text{g}} \gamma_{\text{T}}^2} \\ &\approx \frac{1}{4\pi^2 N_{\text{R}} N_{\text{f}} N_{\text{g}} \gamma_{\text{T}}} \quad \text{for large } \gamma_{\text{T}}, \end{aligned} \quad (4.9)$$

where σ_z^2 is the received signal power in the time domain. Thus, the Signal to Noise Ratio (SNR) of the received signal is written as $\gamma_{\text{T}} = \sigma_z^2/\sigma_v^2$. A detailed derivation of Equation (4.9) can be found in Appendix D.1.

In classical estimation theory, a lower bound on the variance of any unbiased estimator is given as CRLB [61]. Practically, it provides a performance benchmark for any unbiased estimator to compare with. Given the received sequence $r_{l,n}^{(m)}$ and $r_{l,n+N}^{(m)}$, $n \in [-N_{\text{g}}, -1]$, $l \in [0, N_{\text{f}} - 1]$, $m \in [1, N_{\text{R}}]$, as shown in Appendix D.2, the MSE of an unbiased estimator for ε_{FFO} is lower bounded by

$$\text{CRLB}_{\text{FFO}} = \frac{2\sigma_z^2\sigma_v^2 + \sigma_v^4}{8\pi^2 N_{\text{R}} N_{\text{f}} N_{\text{g}} \sigma_z^4}, \quad (4.10)$$

which is identical to the theoretical performance of the ML estimator in Equation (4.9). Knowing that the estimator in Equation (4.1) is unbiased, it can be concluded that the lower bound of the estimation performance has been attained.

A similar procedure can be carried out for the RFO estimator in Equation (4.6). It

leads to a theoretical MSE

$$\begin{aligned} \text{MSE}_{\text{RFO}} &= \frac{N^2(2\sigma_{\text{R}}^2\sigma_{\text{v}}^2 + \sigma_{\text{v}}^4)}{8\pi^2 N_{\text{s}}^2(N + N_{\text{g}})^2 N_{\text{R}} N_{\text{p}} \sigma_{\text{R}}^4} = \frac{N^2(2\gamma_{\text{F}} + 1)}{8\pi^2 N_{\text{s}}^2(N + N_{\text{g}})^2 N_{\text{R}} N_{\text{p}} \gamma_{\text{F}}^2} \\ &\approx \frac{N^2}{4\pi^2 N_{\text{s}}^2(N + N_{\text{g}})^2 N_{\text{R}} N_{\text{p}} \gamma_{\text{F}}} \quad \text{for large } \gamma_{\text{F}}, \end{aligned} \quad (4.11)$$

where σ_{R}^2 denotes the received signal power in the frequency domain. The SNR at each subcarrier¹ accordingly is defined as $\gamma_{\text{F}} = \sigma_{\text{R}}^2/\sigma_{\text{v}}^2$. The term N_{s} denotes the distance between the two RSs on one subcarrier. In the context of LTE, it equals the number of OFDM symbols in one slot, typically $N_{\text{s}} = 7$ for the normal CP. The total number of RSs in one slot is denoted by N_{p} . Following a derivation similar to Appendix D.2, it can be shown that this theoretical performance attains the CRLB of an unbiased estimator given the received RSs in the frequency domain.

Numerical Results

In order to validate the theoretical analysis and evaluate the estimation performance specifically in LTE, simulations were carried out by the *Vienna LTE Link Level Simulator* [7, 60] which provides a standard compliant physical layer implementation in MATLAB. Monte-Carlo simulations were applied to 5 000 LTE subframes transmissions. Since the estimation performance is independent from the magnitude of the CFO [62], a deterministic CFO of $\varepsilon_{\text{CFO}} = 3.14159 \dots$ subcarrier spacing was introduced. The FFO and IFO were estimated at every five subframes, resulting in 1 000 estimates. While the RFO estimated was conducted for all subframes, resulting in 5 000 estimates. Further simulation parameters are listed in Table 4.2.

In the first experiment, the previously derived analytical performance was validated in AWGN channels². Figure 4.5 shows its MSE performance of the FFO and RFO estimation and the error probability (P_e) of the IFO estimation, expressed as

$$P_e = \frac{\text{number of wrong estimates}}{\text{total number of estimates}}. \quad (4.12)$$

The following facts can be observed:

- The MSE curves for FFO estimation obtained from simulations show an excellent agreement to the theoretical performance, meanwhile the CRLB. As the number of receive antennas doubles, a 3 dB gain can be observed.

¹ In this work, SNR is defined on a subcarrier basis. Due to the fact that only N_{tot} out of N subcarriers are actually loaded, there is $\gamma_{\text{T}} = \frac{N_{\text{tot}}}{N} \cdot \gamma_{\text{F}}$.

² We applied a channel matrix $H = [1, 1; 1, -1]$ for the 2×2 case and $H = [1, 1, 1, 1; 1, -1, -1, 1; 1, -1, 1, -1; 1, 1, -1, -1]$ for the 4×4 case, so that $\text{rank}(H) = \min(N_{\text{R}}, N_{\text{T}})$ holds.

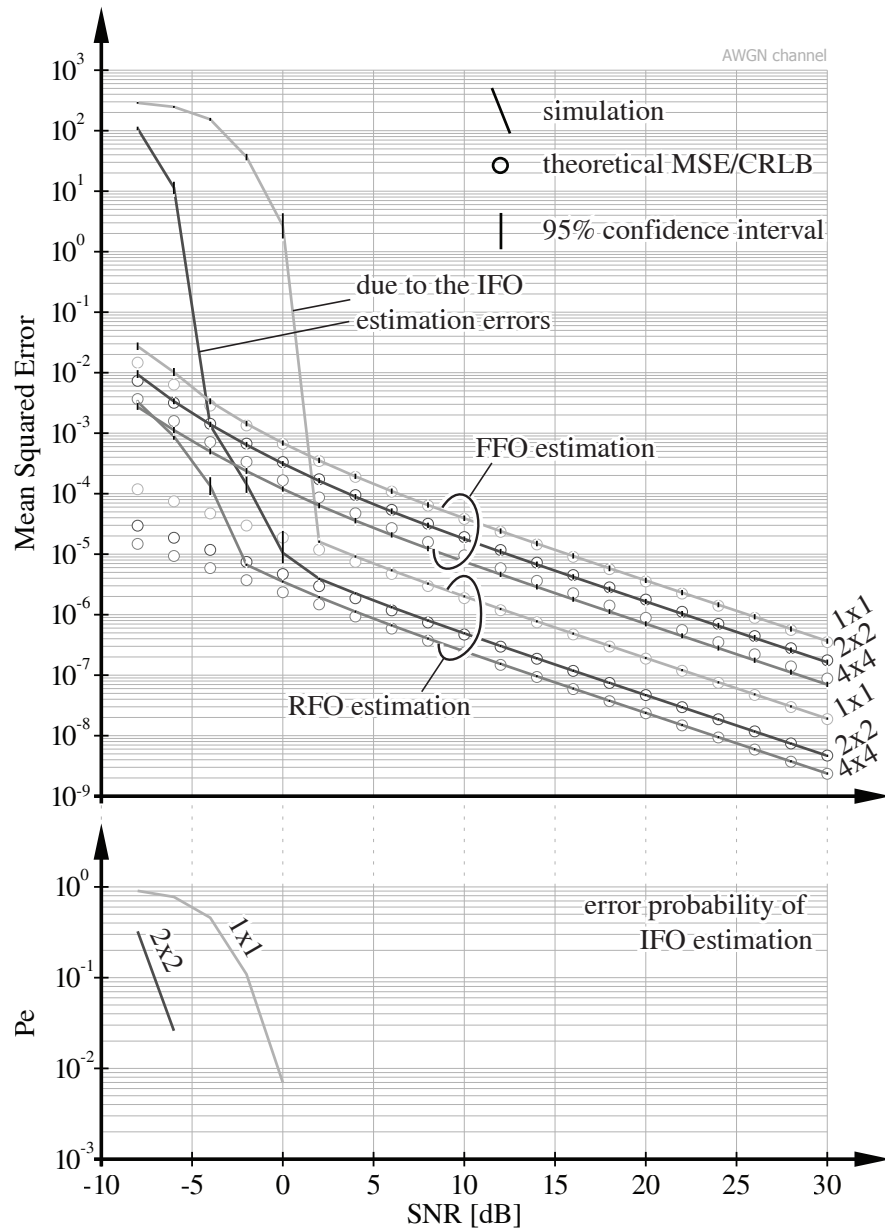


Figure 4.5: CFO estimation performance in AWGN channel. For FFO and RFO, it is measured in terms of MSE, for IFO in terms of the error probability P_e .

Table 4.2.: Simulation parameters for estimation performance evaluation in LTE.

Parameter	Value
Channel bandwidth	1.4 MHz
Carrier frequency	2.5 GHz
Fast Fourier Transform (FFT) size (N)	128
No. data subcarriers	72
Subcarrier spacing	15 kHz
CP length (N_g)	[10, 9] (normal [9])
No. OFDM symbols per slot (N_s)	7
No. OFDM symbols per subframe (N_f)	14
No. RSs per slot used (N_p)	24 for 1×1 , 48 for others
Transmission setting $N_R \times N_T$	1×1 , 2×2 , 4×4
Channel model	AWGN, Pedestrian B [15]
CFO introduced (ε_{CFO})	$\pi = 3.14159 \dots$ subcarrier spacing

- IFO estimation errors occur only in the regime of negative received SNR (in dB).
- In the positive SNR region, the MSE curves for RFO coincide with those from the calculation. Compared with the single antenna case, the 2×2 case provides a 6 dB gain of which 3 dB comes from the doubled number of the RSs and 3 dB from the doubled number of receive antennas. While for the 4×4 case, since the RSs on the third and fourth transmit antenna are not involved in the CFO estimation, merely a 3 dB gain is achieved from the doubled number of receive antennas.
- In the relatively low SNR region, the performance RFO estimation is constrained by two effects, namely IFO estimation error and the magnitude of the residual offset from the FFO estimation. These two effects lead to the outliers in the corresponding region.

The second experiment was carried out in the ITU Pedestrian B channel [15] which consists of multiple paths that result in a deep frequency selective fading in the frequency domain. The resulting curves are shown in Figure 4.6. Except of the error probability curve for IFO estimation which is shifted to the right due to the channel fading, the curves exhibit similar trends as in Figure 4.5. Additionally, it can be observed that the MSE curves for FFO estimation saturate at a certain point, because the CP is corrupted by the multi-path delay. Given this saturation in the frequency selective channel, the third step RFO estimation becomes necessary.

4.3.2. Post-equalization SINR

The impact of the CFO on OFDM systems has been investigated in [3] and [11] where the impact means exclusively the degradation in terms of the SINR after the FFT in an OFDM receiver. This measure implies the degradation induced by

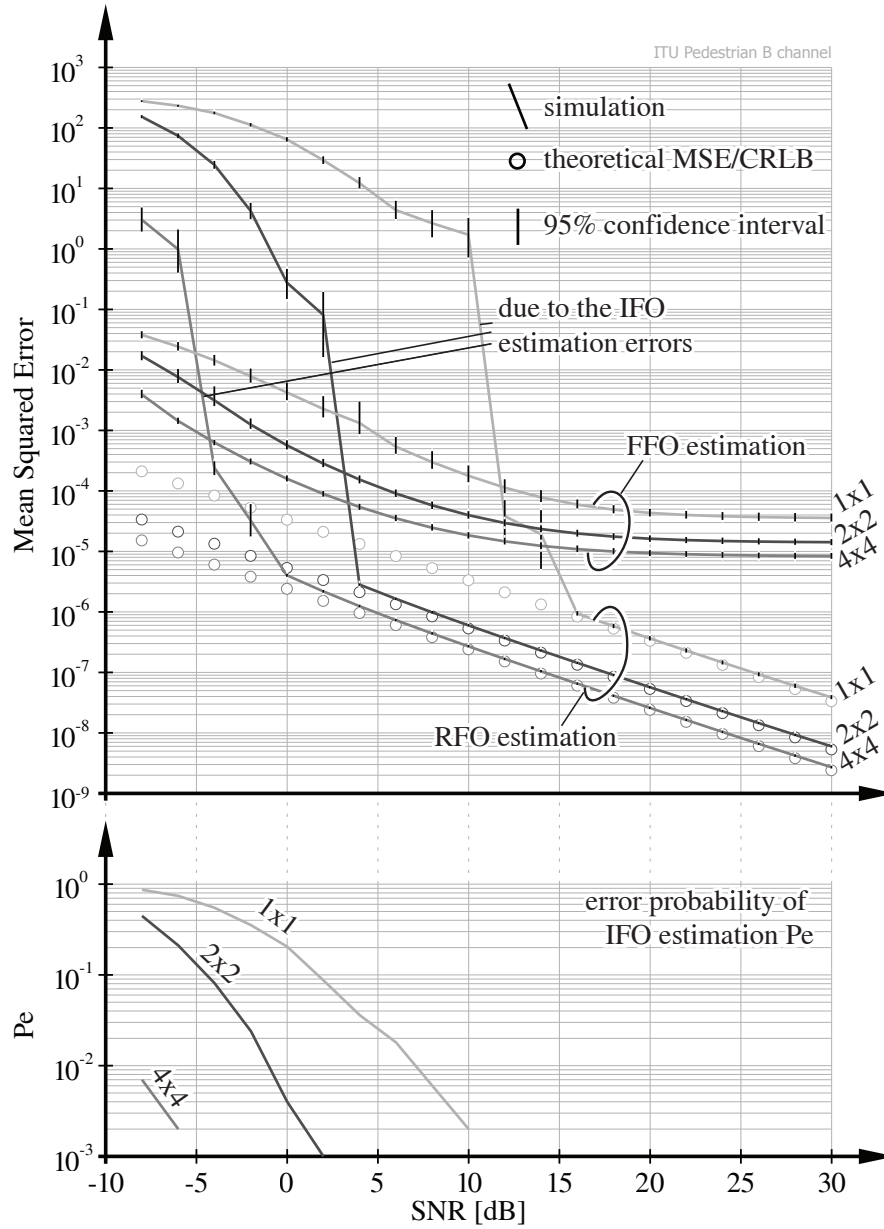


Figure 4.6: CFO estimation performance in ITU Pedestrian B channel.

the ICI. However, for a transmission system employing linear spatial equalizers at the receiver, post-equalization SINR is of more importance, because it directly determines the theoretically possible throughput T via Shannon's formula:

$$T = \log_2(1 + \text{SINR}). \quad (4.13)$$

In order to evaluate the impact of the CFO on the actual link performance, post-FFT processing such as channel estimation, equalization also need to be considered under reasonable assumptions.

As introduced in Section 4.1, data transmission in LTE is subframe-based. For the low mobility case, a block fading assumption holds within the time duration of one subframe, i.e., the channel is assumed to be quasi-static within 1 ms. Under such an assumption, the channel estimator is usually designed to be time invariant within this time interval [63], as well as the channel equalizer. This means, one average channel estimation is obtained using all available RSs on one subcarrier without interpolation in time. Then, equalization is performed on a subframe basis using this average channel knowledge.

In this section, we choose the average post-equalization SINR per subframe as a performance metric and evaluate the impact of the residual CFO on the downlink of LTE, as it was shown in [64].

Analytical Derivation

We constrain the evaluation within one subframe and consider a residual CFO with only a fractional part, denoted by ε . Given the block fading assumption, the time (OFDM symbol) index l of the channel response can be omitted, i.e., $H_k^{(m,q)} = H_{l,k}^{(m,q)}$. The received signal in Equation (2.3) can be written into a vector-matrix form as

$$\mathbf{r}_{l,k} = \mathbf{H}_k \mathbf{x}_{l,k} + \mathbf{v}_{l,k}. \quad (4.14)$$

The transmitted signal vector $\mathbf{x}_{l,k}$ is of length N_T , the receive vector $\mathbf{r}_{l,k}$ of length N_R . The channel \mathbf{H}_k is described by an $N_R \times N_T$ matrix. When the system is impaired by the CFO ε , Equation (4.14) becomes

$$\mathbf{r}_{l,k} = I(0, \varepsilon) \cdot e^{i\Phi(\varepsilon, l)} \cdot \mathbf{H}_k \mathbf{x}_{l,k} + \sum_{p \neq k} I(p - k, \varepsilon) \cdot e^{i\Phi(\varepsilon, l)} \cdot \mathbf{H}_p \mathbf{x}_{l,p} + \mathbf{v}_{l,k}. \quad (4.15)$$

where

$$I(0, \varepsilon) = \frac{\sin(\pi\varepsilon)}{N \sin(\pi\varepsilon/N)} \cdot e^{i\frac{\pi\varepsilon(N-1)}{N}}, \quad (4.16)$$

$$I(p-k, \varepsilon) = \frac{\sin[\pi(p-k+\varepsilon)]}{N \sin[\pi(p-k+\varepsilon)/N]} \cdot e^{i\frac{\pi(p-k+\varepsilon)(N-1)}{N}} \quad (4.17)$$

$$e^{i\Phi(\varepsilon, l)} = e^{i\frac{2\pi\varepsilon l(N+N_g)}{N}}. \quad (4.18)$$

Given the distortion term $I(0, \varepsilon) \cdot e^{i\Phi(\varepsilon, l)}$, the effective channel $I(0, \varepsilon) \cdot e^{i\Phi(\varepsilon, l)} \cdot \mathbf{H}_k$ is dependent on the OFDM symbol index l , in other words, becomes time-variant. However, since the estimator has assumed a time invariant channel over one sub-frame, only an average channel can be obtained.

We first assume that the perfect channel state information is available at each sub-frame. A Zero Forcing (ZF) equalizer at subcarrier k is then given as

$$\mathbf{G}_k = (\mathbf{H}_k^H \mathbf{H}_k)^{-1} \mathbf{H}_k^H. \quad (4.19)$$

Therefore, the estimated data symbol after equalization can be expressed as

$$\begin{aligned} \hat{\mathbf{x}}_{l,k} &= \mathbf{G}_k \cdot \mathbf{r}_{l,k} = I(0, \varepsilon) \cdot e^{i\Phi(\varepsilon, l)} \cdot \mathbf{x}_{l,k} + \underbrace{\mathbf{G}_k \sum_{p \neq k} I(p-k, \varepsilon) \cdot e^{i\Phi(\varepsilon, l)} \cdot \mathbf{H}_p \mathbf{x}_{l,p}}_{\mathbf{i}_{l,k}} + \underbrace{\mathbf{G}_k \mathbf{v}_{l,k}}_{\tilde{\mathbf{v}}_{l,k}} \\ &= I(0, \varepsilon) \cdot e^{i\Phi(\varepsilon, l)} \cdot \mathbf{x}_{l,k} + \mathbf{i}_{l,k} + \tilde{\mathbf{v}}_{l,k}. \end{aligned} \quad (4.20)$$

The $\text{SINR}_{l,k}^{(m)}$ on the m -th Receiver (RX) antenna of the subcarrier k in the l -th OFDM symbol can be found by

$$\text{SINR}_{l,k}^{(m)}(\varepsilon, \mathbf{H}_k) = \frac{\left[\mathbf{x}_{l,k} \mathbf{x}_{l,k}^H \right]_{(m,m)}}{\left[(\hat{\mathbf{x}}_{l,k} - \mathbf{x}_{l,k})(\hat{\mathbf{x}}_{l,k} - \mathbf{x}_{l,k})^H \right]_{(m,m)}}, \quad (4.21)$$

where $[\cdot]_{(i,j)}$ denotes the entry on the i -th row and j -th column of the given matrix. We denote the average signal power on each subcarrier and each antenna by σ_s^2 and the corresponding noise power by σ_v^2 . Plugging Equation (4.20) into Equation (4.21), we obtain a closed form expression of the post-equalization SINR on the m -th RX

Table 4.3.: Carrier Frequency Offsets (CFOs) introduced at carrier frequency 2.5 GHz with subcarrier spacing 15 kHz ($\varepsilon = \Delta f/15$ kHz)

ε [$\cdot 10^{-3}$]	0.10	0.14	0.21	0.30	0.43	0.62	0.89
Δf in Hz	1.5	2.2	3.1	4.5	6.4	9.2	13.3
in ppm [$\cdot 10^{-3}$]	0.6	0.9	1.2	1.8	2.6	3.7	5.3
ε [$\cdot 10^{-3}$]	1.27	1.83	2.64	3.79	5.46	7.85	11.29
Δf in Hz	19.1	27.5	39.5	56.9	81.8	117.7	169.3
in ppm [$\cdot 10^{-3}$]	7.6	11	15.8	22.8	32.7	47.1	67.7
ε [$\cdot 10^{-3}$]	16.24	23.36	33.60	48.33	69.52	100	
Δf in Hz	243.6	350.4	504.0	724.9	1043	1500	
in ppm [$\cdot 10^{-3}$]	97.4	140.1	201.6	290.0	417.1	600.0	

antenna at RE (l, k) , expressed as

$$\begin{aligned}
 \text{SINR}_{l,k}^{(m)}(\varepsilon, \mathbf{H}_k) &= \frac{\sigma_s^2}{\left[\mathbf{i}_{l,k} \mathbf{i}_{l,k}^H \right]_{(m,m)} + \left[\tilde{\mathbf{v}}_{l,k} \tilde{\mathbf{v}}_{l,k}^H \right]_{(m,m)} + |I(0, \varepsilon) \cdot e^{i\Phi(\varepsilon, l)} - 1|^2 \cdot \left[\mathbf{x}_{l,k} \mathbf{x}_{l,k}^H \right]_{(m,m)}} \\
 &= \frac{\sigma_s^2}{\underbrace{\sigma_s^2 \sum_{p \neq k} |I(p-k, \varepsilon)|^2 \left[\mathbf{G}_k^H \mathbf{G}_k \mathbf{H}_p \mathbf{H}_p^H \right]_{(m,m)}}_{\text{ICI}} + \underbrace{\sigma_v^2 \left[\mathbf{G}_k^H \mathbf{G}_k \right]_{(m,m)}}_{\text{noise}} + \underbrace{\sigma_s^2 |I(0, \varepsilon) \cdot e^{i\Phi(\varepsilon, l)} - 1|^2}_{\text{signal distortion}}}
 \end{aligned} \tag{4.22}$$

Numerical Results

In this section, the analytical solution in Equation (4.22) is compared with simulation results obtained using the *Vienna LTE Link Level Simulator* [60]. Aiming to investigate the impact of the residual CFO on the post-equalization SINR, we introduced 20 logarithmically spaced CFOs, shown in Table 4.3. Through this work, ε represents the CFO that is normalized to the subcarrier spacing, namely 15 kHz in LTE. Corresponding values in Hz and in ppm to the carrier frequency are also listed in Table 4.3. The other parameters follow Table 4.2. Neither an estimation nor a compensation procedure was applied at this stage.

Starting with a simple test, we consider an SISO scenario in an AWGN channel. For better visualization of the impact from the CFOs, the SNR is fixed at 30 dB. Using a ZF equalizer with perfect channel knowledge, the simulated post-FFT and post-equalization SINRs are plotted in Figure 4.7 and compared with Equation (2.16) and Equation (4.22), respectively.

As shown in Equation (2.16), the post-FFT SINR implies the impact of the ICI on the OFDM system. Therefore, it can be claimed from Figure 4.7 that up to

$\varepsilon \approx 2.64 \cdot 10^{-3}$, the loss due to ICI is negligible. However, in the meanwhile a dramatic drop occurs at the post-equalization SINR. The denominator of Equation (4.22) explains this phenomenon. Since the equalizer ignores the channel variation within one subframe, a signal distortion term $\sigma_s^2 |I(0, \varepsilon) \cdot e^{i\Phi(\varepsilon, l)} - 1|^2$ appears in the denominator. This is the dominant term that accounts for the performance loss.

By inspecting the output signal from the equalizer in Equation (4.20), the transmitted data symbol is rotated in phase by $\Phi(\varepsilon, l)$ which grows linearly with the OFDM symbol index l and the offset ε . Therefore, the last OFDM symbol may turn over a full circle in one subframe when a large ε occurs. Therefore, a slight fluctuation can be observed at the post-equalization SINR curve around $\varepsilon = 0.1$ in Figure 4.7.

Furthermore, in Figure 4.7, it is observed that calculated results match well with those from the standard compliant simulation. Similar facts can be found in Figure 4.8 for the multiple antenna case in a frequency selective scenario, namely ITU Pedestrian B channel [15]. This indicates that Equation (4.22) can be used as a valid characterization of the system behavior.

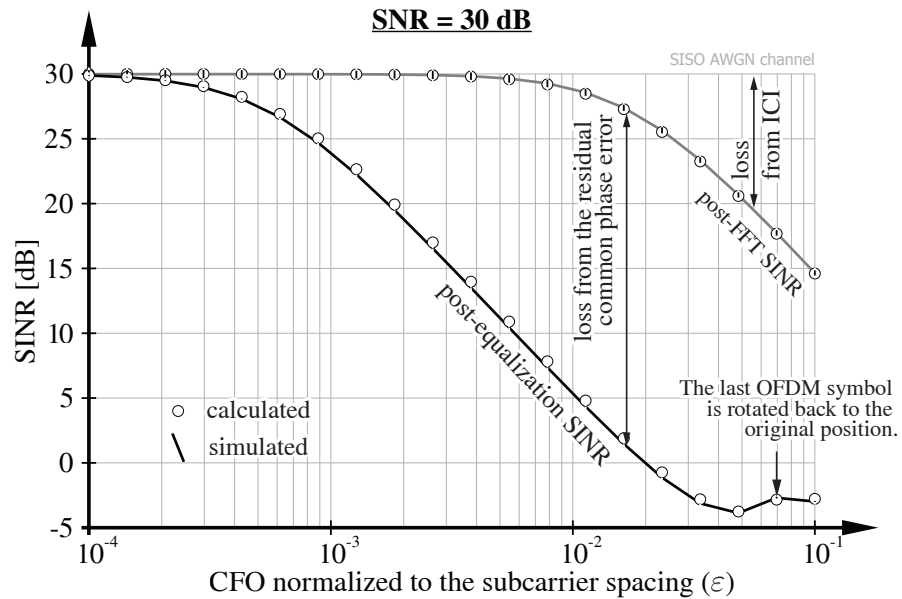


Figure 4.7: SINR under increasing levels of residual CFOs.

On Imperfect Channel Knowledge

In the previous analysis, a perfect channel knowledge \mathbf{H}_k was assumed at the RX for simplicity. However, given a time-invariant channel estimator on a subframe basis, the result will not change dramatically. We consider a simple linear channel estimator. Given the time-frequency grid shown in Figure 4.2, Least Squares (LS)

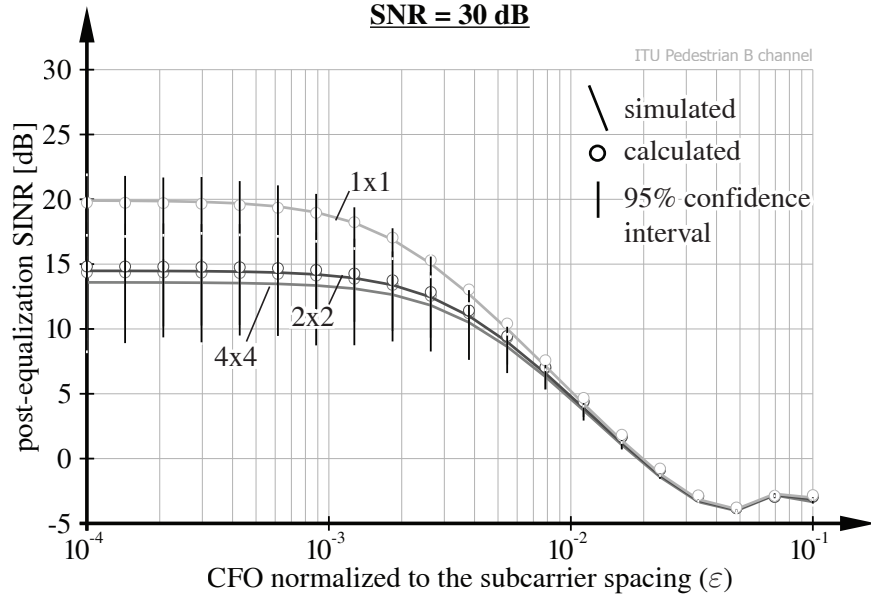


Figure 4.8: Post-equalization SINR under increasing levels of residual CFOs in ITU Pedestrian B channel. Relatively large confidence intervals are due to the frequency selectivity over the data subcarriers.

estimation is applied on the RS positions. Since the block fading scenario assumes a static channel within one subframe duration, channel estimates on the RSs are averaged in the time dimension. In the frequency dimension, linear interpolation is applied. Afterwards, the equalizer is constructed based on the estimated channel state information $\hat{\mathbf{H}}_k$ using Equation (4.19).

In order to demonstrate the effect of the Common Phase Error (CPE) introduced by the CFO, we transmit an all-one sequence on subcarrier k over an AWGN channel, namely $X_{l,k} = 1, H_k = 1$. Thus, any variation in the output signal $\hat{X}_{l,k}$ comes from the CFO. For simplicity, the interference and the noise term in Equation (4.15) are ignored. Figure 4.9 illustrates the phase variation of the transmitted signal over one subframe.

As shown in the signal constellation, a constant phase rotation is induced from one received OFDM symbol to the successive one. In the case shown where the RSs are located in the 4-th and 11-th OFDM symbol, the aforementioned LS channel estimator delivers an estimate given as

$$\begin{aligned}
 \hat{H}_k &= \frac{\hat{H}_{4,k} + \hat{H}_{11,k}}{2} & k \in \mathcal{K}_p, \text{ where } l = 4, 11 & \quad (4.23) \\
 &\approx \frac{\sin(\pi\varepsilon)}{N \sin(\pi\varepsilon/N)} \cdot e^{i\frac{\pi\varepsilon(N-1)}{N}} \cdot \frac{e^{i\Phi(\varepsilon,4)} + e^{i\Phi(\varepsilon,11)}}{2} \cdot H_k \\
 &= \frac{\sin(\pi\varepsilon)}{N \sin(\pi\varepsilon/N)} \cdot e^{i\frac{\pi\varepsilon(N-1)}{N}} \cdot e^{i\Phi(\varepsilon,7.5)} \cos\left(\frac{2\pi\varepsilon(N + N_g)}{N} \cdot 3.5\right) \cdot H_k.
 \end{aligned}$$

Therefore, after equalization using such a time-invariant channel estimate, the entire signal constellation is rotated reversely as shown in Figure 4.9, which unfortunately does not correct the CFO induced phase distortion. Similar to Figure 4.8, the post-equalization SINR in the imperfect channel knowledge case is plotted in Figure 4.10. A similar trend can be observed. Thus in the later analysis, we stick to the perfect channel knowledge assumption for simplicity.

sending an all-one sequence on subcarrier k :

$$\begin{array}{c}
 k \quad \boxed{} \\
 l = 0, 1, 2, \dots \quad X_{l,k} = 1
 \end{array}$$

signal constellation:

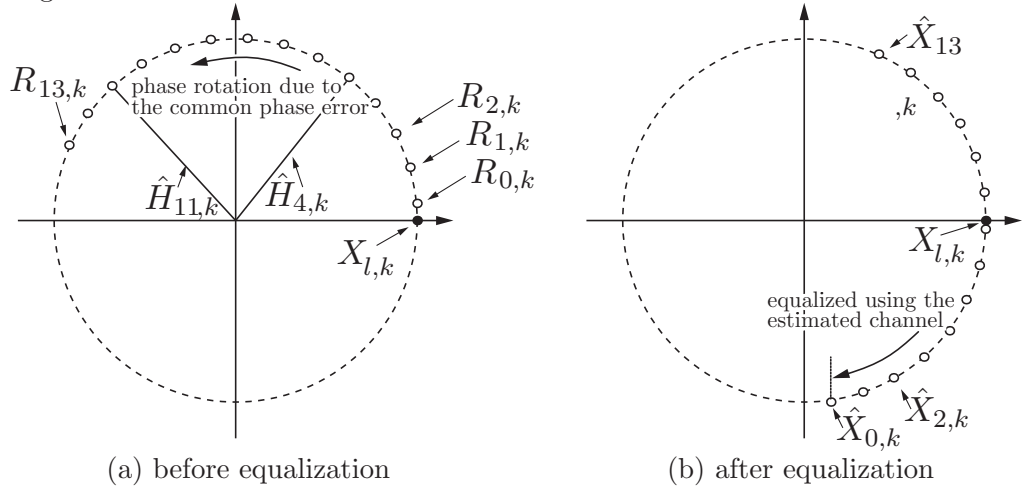


Figure 4.9: Signal constellation variation caused by the CFO when LS channel estimation is applied.

4.3.3. BICM Capacity and Coded Throughput

In [59], a capacity analysis of impaired OFDM links was presented, where the mutual information of the impaired link was calculated using the probability density function of the equalized signal. A different approach has been developed in [47, 65], where bounds on achievable throughput of LTE were derived based on the Bit-Interleaved Coded Modulation (BICM) capacity. However, link impairments was not considered in this case. In this section, we apply the methodology elaborated in [65], utilize the closed form expression of the post-equalization SINR in Equation (4.22) to deliver a quantitative relationship between CFO, OFDM system parameters and the achievable BICM capacity bound of LTE DL. Compared to that of the perfect synchronization case, an expected throughput loss due to the CFO can be claimed.

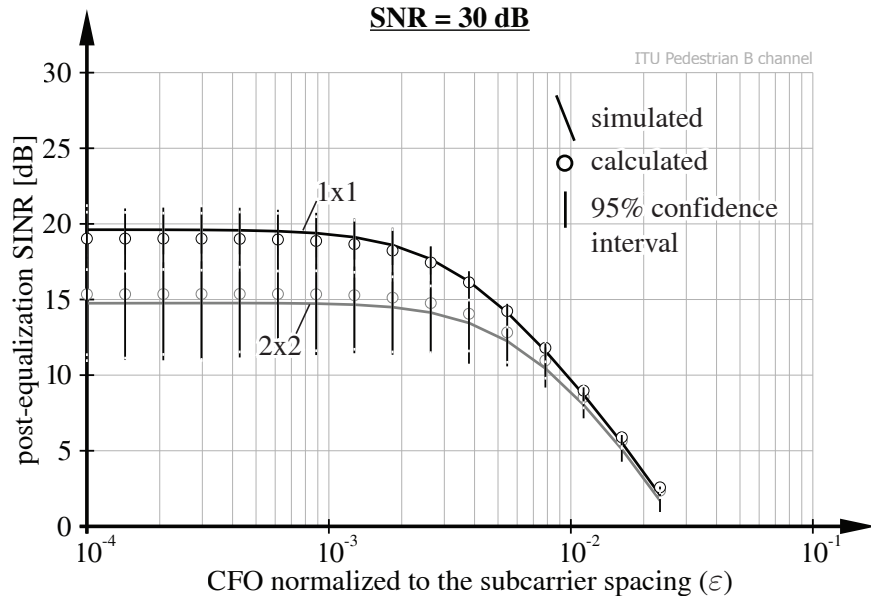


Figure 4.10: Post-equalization SINR under increasing levels of residual CFOs in ITU Pedestrian B channel with LS estimated channel knowledge. Relatively large confidence intervals are due to the frequency selectivity over the data subcarriers.

BICM Capacity

In general, a BICM architecture is obtained by concatenating channel coding with modulation mapping through a bit interleaver. Such a scheme allows combinations of any channel code with any arbitrary modulation alphabet [66]. Based on this architecture, LTE employs 4, 16 or 64-QAM and a rate 1/3 turbo code that is appropriately rate matched to achieve the desired code rates as defined in [67]. The capacity of BICM systems is well known, though not in closed-form [68]. In Figure 4.11, BICM capacity of three defined modulation alphabets are plotted. As suggested in [47], a function $f(\text{SNR})$ is introduced to deliver the maximum efficiency over all available modulation alphabets, shown in Figure 4.11.

Since the focus in this work is to expose the capacity loss due to a physical impairment, namely CFO, issues such as the selection of an optimal precoder and the optimal number of layers transmitted are skipped for simplicity. Instead, identity precoding is applied for the MIMO case. Thus, the spectral efficiency of an LTE system suffers from a CFO ϵ can be expressed as $f(\text{SINR}_r^{(m)}(\epsilon))$, where $\text{SINR}_r^{(m)}(\epsilon)$ is plugged in from Equation (4.22). The index r denotes a RE which is devoted to data transmission, in other words, overhead such as RSs, PSS, SSS and guard bands have been excluded. Therefore, the average spectral efficiency that can be achieved at each transmission layer is written as

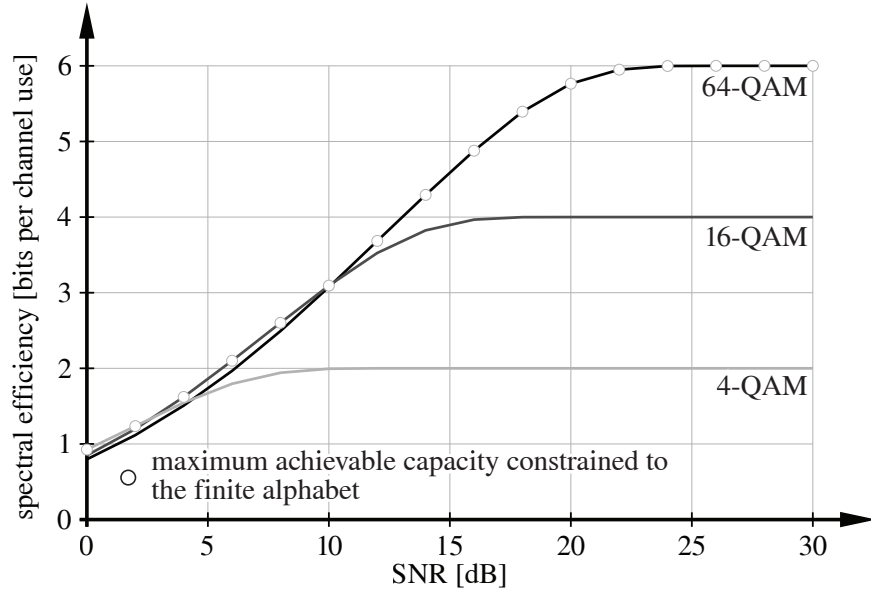


Figure 4.11: BICM capacity of 4, 16 and 64-QAM modulation.

$$\bar{B}(\varepsilon) = \frac{1}{N_r N_R} \sum_r \sum_m f(\text{SINR}_r^{(m)}(\varepsilon, \mathbf{H}_k)), \quad (4.24)$$

where N_r is the number of available data REs, N_R the number of RX antennas. Here, we assume a symmetric configuration of full diversity, e.g., the number of available transmission layers $N_L = N_R = N_T$. According to Equation (4.22), the post-equalization SINR degrades when a CFO occurs. Given several deterministic CFOs, this degradation is shown in Figure 4.12. There, results are calculated based on 200 realizations from the ITU Pedestrian B channel model [15].

The subfigure on the left-hand side shows the theoretical degradation in spectral efficiency subjected to fixed CFOs at different SNR levels. Two CFOs are introduced as examples where $\varepsilon = 1.27 \cdot 10^{-3}$ corresponds to 19.1 Hz and $\varepsilon = 5.46 \cdot 10^{-3}$ to 81.8 Hz given the subcarrier spacing 15 kHz. Compared to the zero-CFO case, it can be observed that the higher SNR region where higher efficiency is aimed, appears to be more sensitive to the CFO. Whereas, the impacts on SISO and MIMO systems are fairly equal.

In the subfigure on the right-hand side, the SNR is fixed at 30 dB in order to visualize the impact under CFOs of increasing magnitude. The average spectral efficiency starts to decrease around $\varepsilon = 1 \cdot 10^{-3}$, approximately. Similar behavior can be observed for the SISO and MIMO cases, although the average spectral efficiency per layer slightly decreases for the multiple antenna scenario due to the incremental noise enhancement from a ZF equalizer.

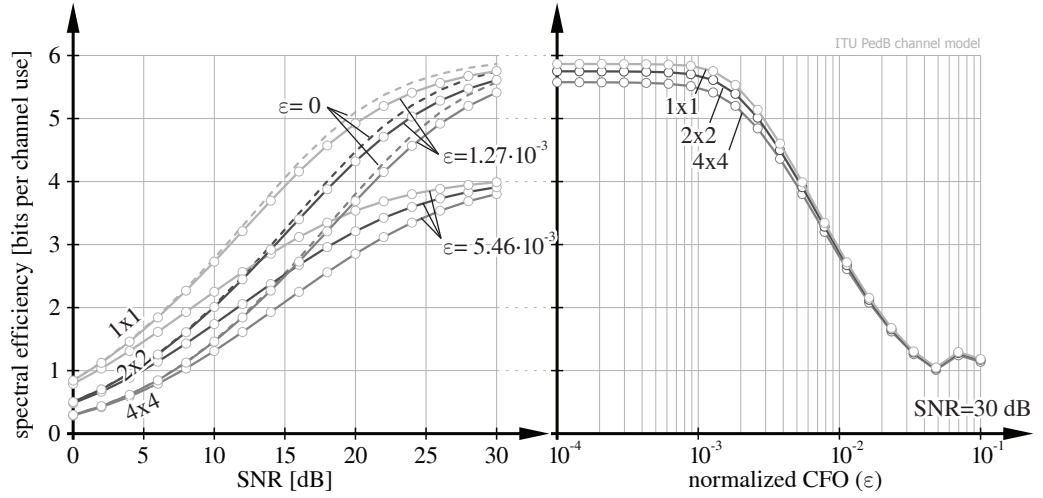


Figure 4.12: Degradation in average spectral efficiency (per layer for the MIMO cases) due to the residual CFOs.

Based on these theoretical analysis, it can be concluded that given the physical layer design of LTE and slow fading scenario, a residual CFO lower than 15 Hz must be guaranteed especially in the high SNR region.

Coded Throughput

In the previous analysis, only residual CFOs of fixed values were considered. However, knowing that a residual CFO is in fact the error of a CFO estimation, as implied in Section 4.3.1, the estimation performance should be considered when evaluating the system performance. Although the higher SNR region appears to be more sensitive to the CFO according to Figure 4.12, smaller estimation errors are expected at the higher SNRs. In the following, we try to expose an expectation of the throughput loss in the LTE DL subjected to the residual estimation errors of the CFO. Comparison is drawn between the calculated BICM capacity and the simulated coded throughput.

Consider an LTE DL experiencing slow frequency selective fading where the channel is quasi-static within one subframe duration, the channel estimator and equalizer on the receiver side are designed to be subframe based time-invariant. A CFO occurs between the two local oscillators at the TX and the RX. In the receiver as shown in Figure 4.4, the three-step CFO estimation presented in Section 4.2 is applied. After these three steps, given the theoretical estimation performance, meanwhile the CRLB in Equation (4.11), a theoretical residual estimation error can be assumed, written as $\bar{\varepsilon} = \sqrt{\text{MSE}_{\text{RFO}}(\gamma)}$. Here, γ denotes the SNR at the receiver side in the frequency domain on RS positions. Thus, a theoretically achievable BICM capacity can be expressed as

Table 4.4.: Simulation parameters for coded throughput evaluation in LTE.

Parameter	Value
Channel bandwidth	1.4 MHz
FFT size (N)	128
No. data subcarriers	72
Subcarrier spacing	15 kHz
CP length (N_g)	[10, 9] (normal [9])
Transmission setting $N_R \times N_T$	$1 \times 1, 2 \times 2$
Transmission mode	open-loop spatial multiplexing
Precoding	identity
Channel model	Pedestrian B [15]
CFO introduced (ε_{CFO})	$0, 0.14159 \dots$ subcarrier spacing
Channel knowledge	perfect
Equalizer	Zero Forcing (ZF)
CQI feedback	optimal

$$B(\gamma) = \sum_r \sum_m f(\text{SINR}_r^{(m)}(\bar{\varepsilon}, \mathbf{H}_k)) = \sum_r \sum_m f(\text{SINR}_r^{(m)}(\sqrt{\text{MSE}_{\text{RFO}}(\gamma)}, \mathbf{H}_k)). \quad (4.25)$$

This capacity bound takes into account the finite set of Modulation and Coding Schemes (MCSs) suggested in [67], a linear receiver structure and the limitation of the CFO estimation performance, while ignores other aspects such as a finite code block length, limited number of code rates as well as an optimal selection of precoding matrix and number of transmission layers. Since we are only interested in the throughput loss compared to the perfect synchronization case, these imperfect aspects will cause an offset in the absolute value of the estimated throughput, but this offset approximately cancels out when calculating the throughput loss

$$\Delta B(\gamma) = \sum_r \sum_m f(\text{SINR}_r^{(m)}(0, \mathbf{H}_k)) - \sum_r \sum_m f(\text{SINR}_r^{(m)}(\bar{\varepsilon}, \mathbf{H}_k)). \quad (4.26)$$

For comparison, we simulated coded throughput of the LTE DL using the *Vienna LTE Link Level Simulator* [60]. The parameter setting is shown in Table 4.4. Unlike previous experiments, the IFO estimation error is excluded. Fifteen MCSs indicated by Channel Quality Indicators (CQIs) shown in Table 4.5 are implemented. In the LTE DL, UEs provide wideband feedbacks to the eNodeB so that the MCS can be adapted to the current channel quality. In our experiment, the CQI feedback is forced to optimum by selecting the MCS that delivers the highest throughput for each channel realization.

Figure 4.13 and Figure 4.14 exhibit the results obtained for a SISO and a 2×2

4. LTE PERFORMANCE UNDER CARRIER FREQUENCY OFFSET (CFO)

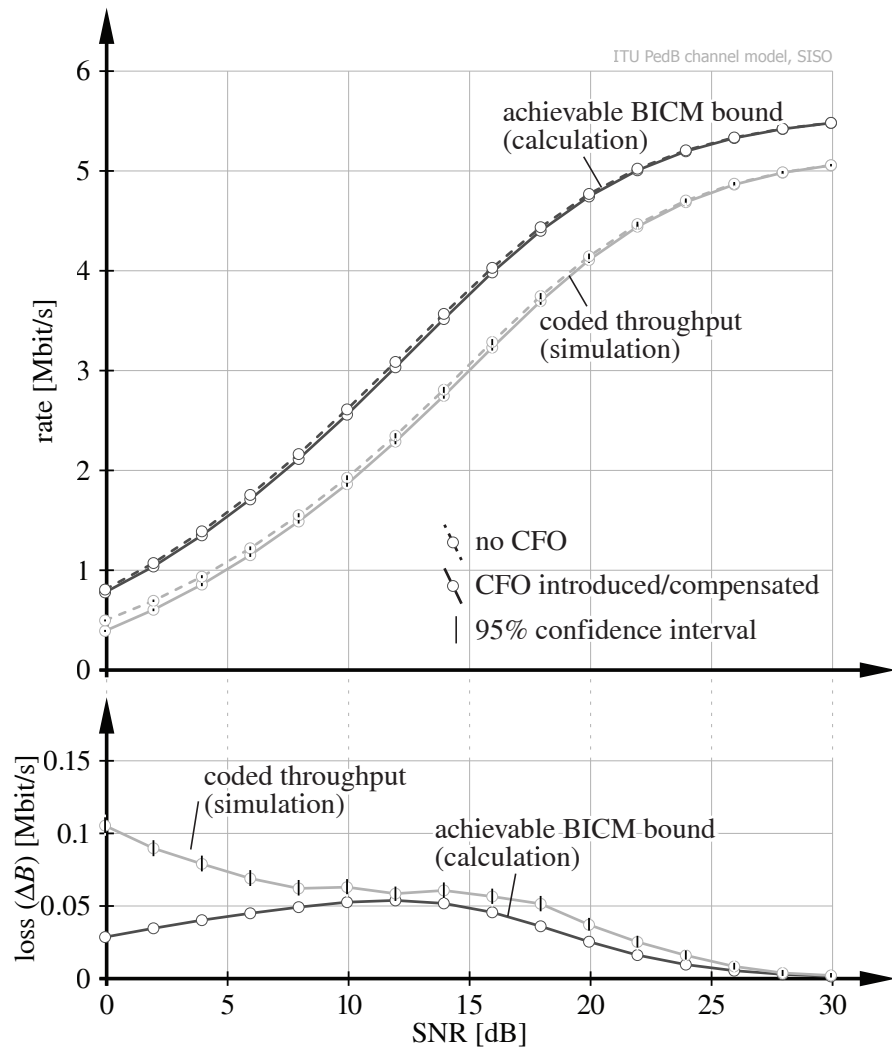


Figure 4.13: Achievable BICM capacity and simulated coded throughput for an SISO LTE DL under CFO, 5 000 subframes Monte Carlo simulation.

4. LTE PERFORMANCE UNDER CARRIER FREQUENCY OFFSET (CFO)

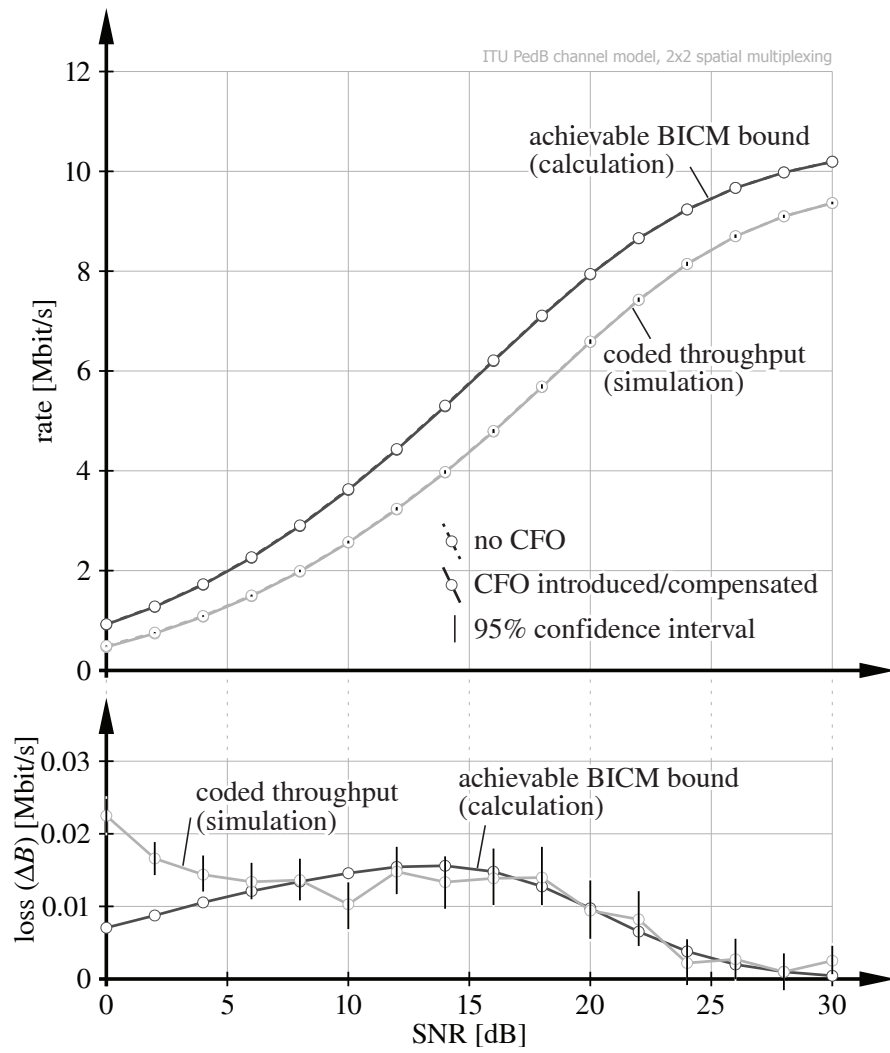


Figure 4.14: Achievable BICM capacity and simulated coded throughput for a 2×2 spatial multiplexing LTE DL under CFO, 5 000 subframes Monte Carlo simulation.

Table 4.5.: Modulation scheme and effective coding rate for each of the Channel Quality Indicators (CQIs).

CQI Index	Modulation	ECR	Data [bit/symbol]
0		out of range	
1	4-QAM	0.08	0.15
2	4-QAM	0.12	0.23
3	4-QAM	0.19	0.38
4	4-QAM	0.30	0.60
5	4-QAM	0.44	0.88
6	4-QAM	0.59	1.18
7	16-QAM	0.37	1.48
8	16-QAM	0.48	1.91
9	16-QAM	0.60	2.41
10	64-QAM	0.46	2.73
11	64-QAM	0.55	3.32
12	64-QAM	0.65	3.90
13	64-QAM	0.75	4.52
14	64-QAM	0.85	5.12
15	64-QAM	0.93	5.55

MIMO LTE DL. In the upper figures, coded throughputs of ideally synchronized transmission are compared to the CFO-compensated case. When the three-step CFO estimation scheme is applied, loss between the two cases is hardly visible, especially for the MIMO case. The corresponding achievable BICM capacity curves confirm such an observation. Although there is a constant difference between the calculated capacity curves and the simulated throughput, it is due to the imperfect channel code which is beyond the scope of this work.

In the lower subfigures of Figure 4.13 and Figure 4.14, the absolute throughput loss between the no-CFO and the CFO-compensated case are plotted. In the higher SNR region, it can be observed that the simulated coded throughput loss follows the trend of the analytical calculation. However, large differences appear in the lower SNR region. This can be explained as following: in the theoretical analysis, merely the estimation error of the third stage, RFO estimation, is considered. Whereas, in the lower SNR region, the true residual error exceeds the estimation range of the RFO estimator. This effect is not modeled by the theoretical MSE performance.

4.4. Conclusion

As pointed out at the beginning of Section 4.3, when the carrier frequency synchronization issue is encountered in a practical OFDM system, the question is not only about how accurate the CFO estimation is, but also how robust such a system is to a residual estimation error. In this work, we have shown that, in LTE DL, a general

conclusion for OFDM, e.g., "for negligible SNR degradation the carrier frequency offset has to be corrected to values $\varepsilon < 0.004 \dots$ [3]" is not true. In contrast, we have shown that a higher accuracy of $\varepsilon < 0.001$ is required.

Although ICI has been claimed to be the major reason that degrades the link performance, by an appropriate post-equalization SINR model, it is shown that even when the CFO is so small that its resulting ICI can be neglected, a dramatic loss can be observed due to the CPE, although it is in general believed that CPE can be handled properly by channel estimation. However, a time-invariant channel estimator in reality fails this expectation. Therefore, in a practical system, it is not only the physical impairment itself that influences the overall performance. Instead, the system design might amplify this influence as well.

The capacity analysis in Section 4.3.3 shows that for a high SNR at 30 dB, the LTE DL requires the variance of the CFO estimation error to be lower than approximately $1 \cdot 10^{-6}$. Though critical, the three-step CFO estimation scheme presented in Section 4.2 fulfills this requirement, as it did in WiMAX. The throughput loss after CFO compensation is negligible for both SISO and MIMO cases.

In this chapter, we elaborated a performance evaluation approach to expose the throughput loss due to a CFO in the LTE DL. This model interconnects the three performance metrics, namely MSE, post-equalization SINR and coded throughput, and is applicable to OFDM systems in general. Although in this work for simplicity, the post-equalization SINR model is only derived for systems using a ZF equalizer, it can be adapted for systems using another linear equalizer, e.g., a Minimum Mean Squared Error (MMSE) equalizer. Also, the BICM capacity is employed to estimate the throughput due to the fact that LTE is based on a BICM architecture. It needs to be adjusted according to a different system specification as well.

5. LTE Performance under Symbol Timing Offset (STO)

This chapter presents a performance evaluation of the Long Term Evolution (LTE) Downlink (DL) under imperfect symbol timing. Section 5.1 describes the background of the symbol timing synchronization issue in the context of the LTE DL. As an intermediate step, Section 5.2 discusses the impact of a Symbol Timing Offset (STO) on two state-of-the-art channel estimators, namely the Least Squares (LS) and the Linear Minimum Mean Squared Error (LMMSE). Section 5.3 evaluates the link performance by modeling the post-equalization Signal to Interference-plus-Noise Ratio (SINR) as a function of a residual STO. The mathematical analysis is validated by standard compliant simulations. Section 5.4 provides a throughput evaluation using standard compliant link level simulator. Section 5.5 concludes the chapter.

5.1. Background

Unlike the Carrier Frequency Offset (CFO), symbol timing acquisition in the LTE DL is closely related to the initial access procedure. This so-called cell search procedure enables a User Equipment (UE) to synchronize with a cell and detect its physical layer cell identity [69]. In LTE, there are in total 504 unique physical layer cell identities. They are grouped into 168 groups, each of which contains three identities that are usually assigned to the three sectors under the control of one eNodeB. With the physical layer cell identity, the reference signals and control information can be obtained at the UEs [9].

After power-up, a UE performs an initial synchronization procedure starting with

the detection of the Primary Synchronization Signal (PSS)(Figure 4.3) from the incoming sequence in the digital time domain. This allows the UE to acquire the cell identity within a group and in the meanwhile synchronize on a 5 ms basis. In the next stage, the group identity and the frame timing is obtained by detecting the Secondary Synchronization Signal (SSS). After the initial cell search procedure, it is generally assumed that the Orthogonal Frequency Division Multiplexing (OFDM) symbol timing is inherently obtained.

Due to the importance of the cell search, the PSS and SSS are designed to be well suited for the cell identity acquisition, namely, with good periodic autocorrelation and cross-correlation properties, robustness against potential frequency offsets [52]. These properties ensure that a UE acquires its cell identity in an ill-conditioned scenario without any a-priori knowledge. However, the correlation-based approach does not necessarily result in an accurate frame/symbol timing estimation, especially in Non-Line-of-Sight (NLOS) scenarios [70, 71]. Instead of the earliest arrived signal, the correlation based approach detects the signal arrives from the strongest path. Thus, a late timing becomes a common issue when no Line-of-Sight path is available.

Over decades, plenty of efforts have been dedicated to developing STO estimators for OFDM systems, [14, 23, 26, 32, 33, 37, 70–72]. They fall into two categories, i.e., data-aided and non-data-aided. The data-aided estimators obtains the symbol timing using a carefully chosen training sequence [23, 26]. Non-data-aided methods utilizes either the implicit repetition structure of the Cyclic Prefix (CP) [32, 70–72] or are exclusively based on the statistical characteristics of the received signal [14, 33, 37]. The former type has been adopted, for example, in IEEE 802.16 suite [1] where a preamble is equipped for every frame. The latter, however, is able to cope with any OFDM based system without specific overhead constraints.

Unlike the IEEE 802.11/16 protocol suite which mainly targets for burst mode data transmission, in a cellular radio system such as LTE, a UE must maintain its connection to a serving eNodeB. This guarantees that the UE is in general synchronized to one eNodeB, although with a limited accuracy.

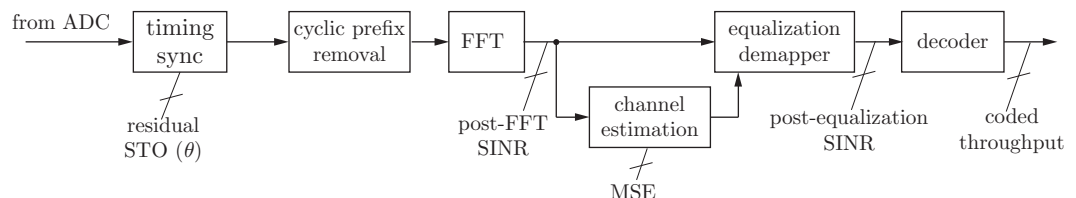


Figure 5.1: Evaluate the impact of residual STOs at different positions in an LTE receive signal processing chain.

In this section, the link performance of LTE DL under an imperfect symbol timing is evaluated. As shown in the block diagram in Figure 5.1, the potential performance

degradation from a residual STO can be evaluated at several positions. The impact of the STO on a general OFDM system has been discussed in Section 2.3.2. The analysis was based on the post-Fast Fourier Transform (FFT) SINR. This metric implies the SINR degradation due to the Inter-Carrier Interference (ICI) and the Inter-Symbol Interference (ISI) induced by the STO. As for how this degradation accounts for a link performance degradation at the end of the signal processing chain, other aspects in the receiver, e.g., channel estimation and equalization, need to be considered. In the following sections, we first analyze the impact of a residual STO on the channel estimators; then, the link performance degradation is evaluated in terms of the post-equalization SINR.

5.2. Impact of STO on Channel Estimation

LTE defines a series of Reference Signals (RSs) allowing for coherent detection [9]. The state-of-the-art channel estimators can be implemented using the RSs depicted in Figure 4.2 [63, 73, 74]. The influence of a residual STO on pilot-aided channel estimation in OFDM has been firstly exposed in [75]. For an LS estimator, references have shown that the residual STO does not negatively affect the channel estimation on the pilot subcarriers, but does corrupt the channel information obtained via interpolation [76–78]. For an LMMSE estimator which requires the second-order channel statistics as a-priori knowledge, the estimation performance is determined by the accuracy of the a-priori knowledge [79]. In this section, these aspects are discussed in the context of LTE DL. The performance degradation in these two channel estimators due to a residual STO is evaluated in terms of the Mean Squared Error (MSE).

In LTE [9] DL, cell-specific RSs are utilized in channel estimation for both demodulation and feedback calculation. The cell-specific RSs are multiplexed in time and frequency. At each RS instance, only one antenna transmits RS while the other antennas keep silence. Such a structure leads the Multiple Input and Multiple Output (MIMO) channel estimation equivalent to that for the Single Input and Single Output (SISO) case.

5.2.1. LS Channel Estimator

In order to derive a linear channel estimator based on the cell-specific RS in LTE, we rewrite the received signal in OFDM symbol l in Equation (2.31) as

$$\begin{aligned} \mathbf{r}_l &= \underbrace{\mathbf{A}^{(d)}(\theta)\mathbf{x}_l}_{\text{desired signal}} + \underbrace{\mathbf{A}^{(o)}(\theta)\mathbf{x}_l}_{\text{ICI}} + \underbrace{\mathbf{B}(\theta)\mathbf{x}_{\text{int}}}_{\text{ISI}} + \mathbf{v}_l \\ &= \mathbf{X}_l \cdot \mathbf{a}_l + \mathbf{w}_l. \end{aligned} \quad (5.1)$$

The diagonal matrix \mathbf{X}_l has the entries in \mathbf{x}_l on its diagonal, while the vector \mathbf{a}_l contains the diagonal elements in $\mathbf{A}^{(d)}(\theta)$. The three interfering terms are combined as \mathbf{w}_l . The effective channel on the desired signal \mathbf{a}_l can be further factorized as

$$\mathbf{a}_l = \alpha \cdot \mathbf{E}(\theta) \cdot \mathbf{h}_l, \quad (5.2)$$

where α is a so-called attenuation factor determined by the STO and the channel Power Delay Profile (PDP). The matrix $\mathbf{E}(\theta)$ represents the phase rotation:

$$\mathbf{E}(\theta) = \begin{bmatrix} 1 & 0 & \cdots & 0 \\ 0 & e^{i\frac{2\pi\theta}{N}} & \ddots & \vdots \\ \vdots & \ddots & \ddots & 0 \\ 0 & \cdots & 0 & e^{i\frac{2\pi\theta(N_{\text{tot}}-1)}{N}} \end{bmatrix} \quad (5.3)$$

The vector \mathbf{h}_l denotes the undistorted channel frequency response. Let $(l', k') \in \mathcal{K}_p$ indicates the RS symbols positions, the corresponding LS estimation on these positions can be expressed as

$$\hat{\mathbf{a}}_{l', \text{RS}}^{\text{LS}} = \arg \min_{\hat{\mathbf{a}}_{l', \text{RS}}} \|\mathbf{r}_{l', \text{RS}} - \mathbf{X}_{l', \text{RS}} \hat{\mathbf{a}}_{l', \text{RS}}\|_2^2 = \mathbf{X}_{l', \text{RS}}^\dagger \mathbf{r}_{l', \text{RS}}, \quad (5.4)$$

where \dagger denotes the pseudo-inverse. Such an estimator delivers a suboptimal estimation performance with relatively low computation complexity [80]. Refer to Equation (2.32), an LS estimator treats ICI and ISI simply as additive noise, leading to the theoretical MSE on an arbitrary RS position (l', k')

$$\begin{aligned} \sigma_{e, \text{RS}}^2 &= \mathbb{E}\{\|a_{k'k'}^{\text{LS}} - \hat{a}_{k'k'}\|^2\} \\ &= \underbrace{\sum_{p \neq k'} |a_{k'p}|^2}_{\text{ICI}} + \underbrace{\sum_p |b_{k'p}|^2}_{\text{ISI}} + \frac{\sigma_v^2}{\sigma_s^2}. \end{aligned} \quad (5.5)$$

On data symbol positions, linear interpolation is applied. Let u and v denote two adjacent RS subcarriers. Given that the error terms are uncorrelated to the desired

channel, we can write

$$\hat{a}_{uu}^{\text{LS}} = a_{uu} + e_u, \quad \hat{a}_{vv}^{\text{LS}} = a_{vv} + e_v, \quad (5.6)$$

where e_u, e_v are the estimation errors on the two RS subcarriers. Thus, on data position k between u and v , the channel estimate is obtained by

$$\hat{a}_{kk} = c_u \hat{a}_{uu}^{\text{LS}} + c_v \hat{a}_{vv}^{\text{LS}} = c_u a_{uu} + c_u e_u + c_v a_{vv} + c_v e_v; \quad c_v = 1 - c_u \quad (5.7)$$

which leads to the estimation error on the data position k

$$a_{kk} - \hat{a}_{kk} = \underbrace{a_{kk} - c_u a_{uu} - c_v a_{vv}}_{\text{interpolation error}} - \underbrace{c_u e_u - c_v e_v}_{\text{estimation error}}. \quad (5.8)$$

Estimation Performance

Similar to the result that was shown in [81], the theoretical MSE on the interpolated data positions becomes

$$\sigma_{\text{e,data}}^2 = \mathbb{E}\{\|a_{kk} - \hat{a}_{kk}\|_2^2\} = \sigma_{\text{int}}^2 + \underbrace{(c_u^2 + c_v^2)}_{c_e} \cdot \sigma_{\text{e,RS}}^2, \quad (5.9)$$

where the interpolation error

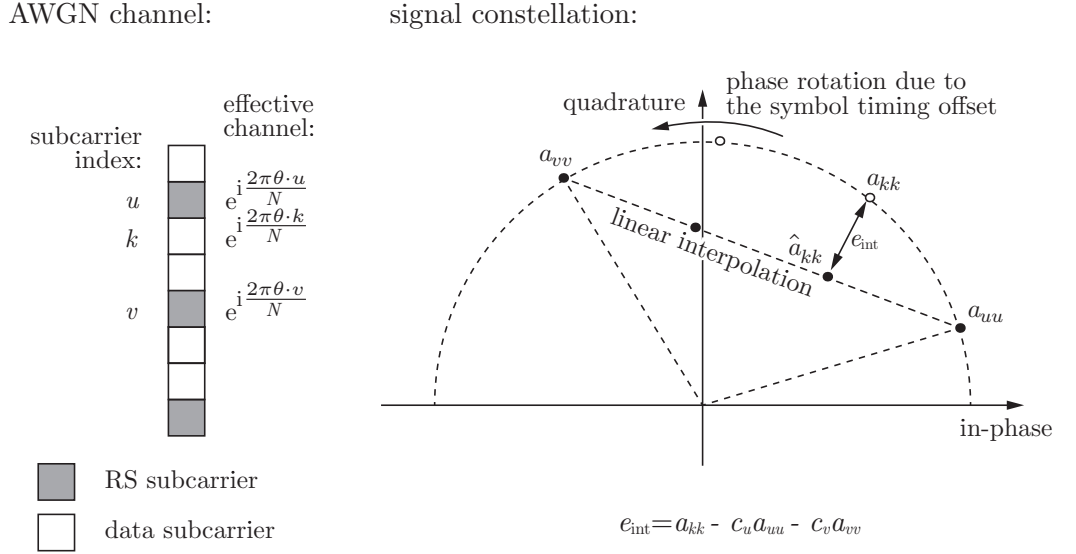
$$\begin{aligned} \sigma_{\text{int}}^2 &= \mathbb{E}\{(a_{kk} - c_u a_{uu} - c_v a_{vv})(a_{kk} - c_u a_{uu} - c_v a_{vv})^*\} \\ &= \mathbf{R}_{aa}^{(k,k)} + c_u^2 \mathbf{R}_{aa}^{(u,u)} + c_v^2 \mathbf{R}_{aa}^{(v,v)} \\ &\quad - 2c_u \cdot \Re\{\mathbf{R}_{aa}^{(u,k)}\} - 2c_v \cdot \Re\{\mathbf{R}_{aa}^{(v,k)}\} + 2c_u c_v \cdot \Re\{\mathbf{R}_{aa}^{(u,v)}\}. \end{aligned} \quad (5.10)$$

The autocorrelation matrix \mathbf{R}_{aa} refers to the effective channel frequency response \mathbf{a}_l , namely

$$\mathbf{R}_{aa} = \mathbb{E}\{\mathbf{a}_l \mathbf{a}_l^{\text{H}}\} = \alpha^2 \cdot \mathbf{E}(\theta) \mathbb{E}\{\mathbf{h}_l \mathbf{h}_l^{\text{H}}\} \mathbf{E}(\theta)^{\text{H}} = \alpha^2 \cdot \mathbf{E}(\theta) \mathbf{R}_{hh} \mathbf{E}(\theta)^{\text{H}}, \quad (5.11)$$

where \mathbf{R}_{hh} is the autocorrelation matrix of the undistorted channel.

The interpolation coefficients c_u and c_v are determined by the RS structure, more precisely, the RS spacing in the frequency dimension. A spacing of three subcarriers for the cell specific RSs in LTE DL results in $(c_u, c_v) = (\frac{1}{3}, \frac{2}{3})$. Equations (5.9) to (5.11) imply that the ICI and the ISI degrade the estimation performance on the RS positions, whereas the interpolation error on a data position is exclusively dependent on the effective channel autocorrelation matrix. The relationship between the STO and the interpolation error is illustrated in Figure 5.2 for an Additive White Gaussian Noise (AWGN) channel.


 Figure 5.2: Interpolation error given an STO θ .

In Figure 5.3, the MSE of the channel estimation versus various levels of STOs at a 30 dB Signal to Noise Ratio (SNR) can be found. The two constructive parts, namely the estimation error and the interpolation error, are plotted individually. In the late timing region, i.e., $\theta < 0$, the total error mainly attributes to the estimation error caused by the ICI and the ISI. The interpolation error in this region is relatively small. Whereas in the early timing region, i.e., $\theta > 0$, the interpolation error dominates the total error magnitude, even in the valid timing region where ICI and ISI are in fact negligible.

In Figure 5.4, MSE curves are plotted for several fixed STO at different SNRs. Since the interpolation error σ_{int}^2 does not depend on the noise amplitude, an error floor can be observed for the total performance especially at higher SNRs.

The dramatic performance degradation of an LS channel estimator due to the STO calls for a different interpolation technique. In [82], several alternative interpolators are provided, some of which are further discussed in [83, 84]. In the following, two alternative interpolation methods are introduced.

Polar-linear Interpolator

Although it was originally not intended to combat an imperfect symbol timing, the idea of polar linear interpolation has gained attention because it is very simple to implement [82–84]. Unlike the typical linear interpolator which interpolates in the complex plane, a polar-linear interpolator does the job using the polar coordinates.

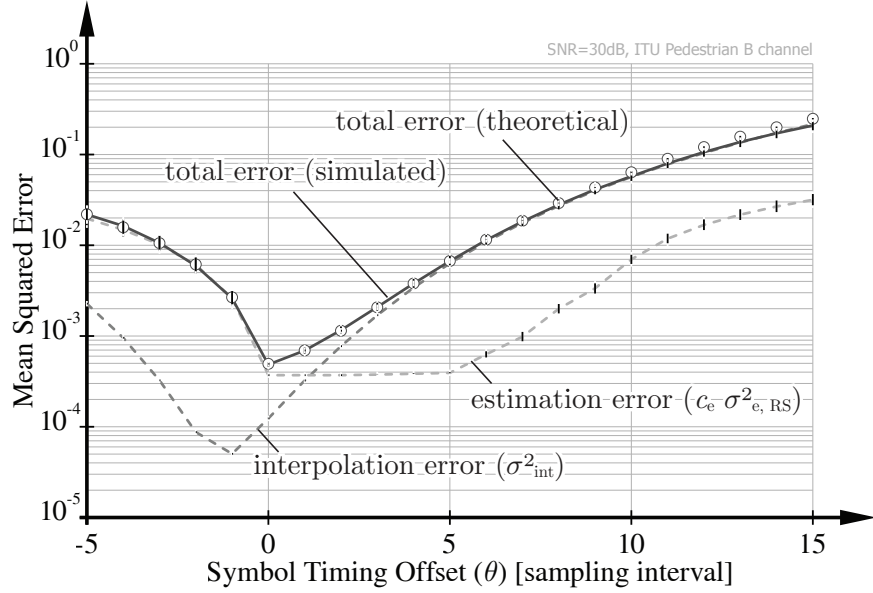


Figure 5.3: MSE of the LS channel estimator versus STOs in ITU Pedestrian B channel at 30 dB SNR.

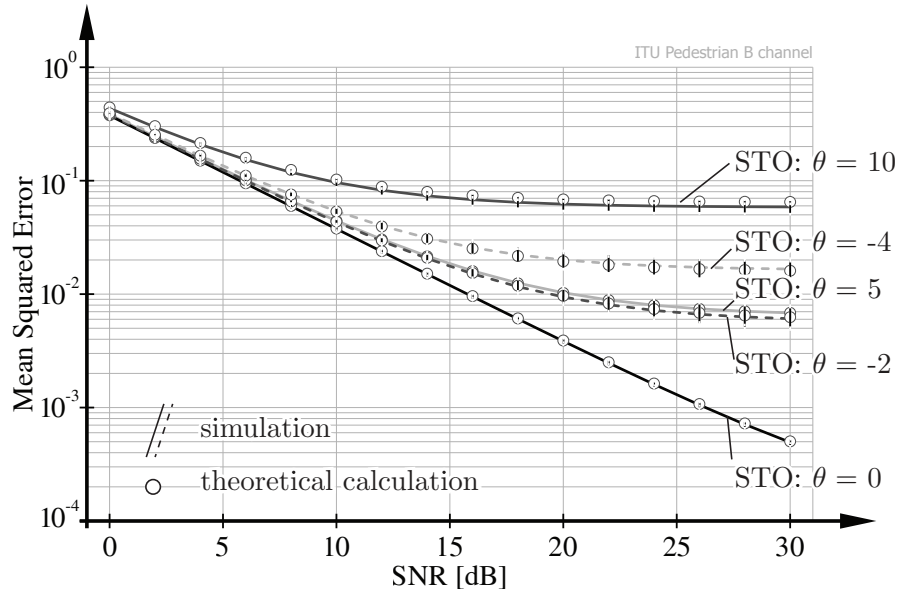


Figure 5.4: MSE of the LS channel estimator versus SNR, with STOs $\theta = \{-4, -2, 0, 5, 10\}$.

We write the estimated channel response on the two adjacent RS subcarriers as

$$\hat{a}_{uu}^{\text{LS}} = |\hat{a}_{uu}^{\text{LS}}| \cdot e^{j\phi_u}, \quad \phi_u = \arg\{\hat{a}_{uu}^{\text{LS}}\}, \quad (5.12)$$

$$\hat{a}_{vv}^{\text{LS}} = |\hat{a}_{vv}^{\text{LS}}| \cdot e^{j\phi_v}, \quad \phi_v = \arg\{\hat{a}_{vv}^{\text{LS}}\}. \quad (5.13)$$

The estimate on the data subcarrier k in between is obtained by applying linear interpolation in terms of magnitude and of argument, respectively:

$$\hat{a}_{kk} = (c_u \cdot |\hat{a}_{uu}^{\text{LS}}| + c_v \cdot |\hat{a}_{vv}^{\text{LS}}|) \cdot e^{j\phi_k}, \quad \phi_k = c_u \cdot \phi_u + c_v \cdot \phi_v. \quad (5.14)$$

Phase Compensated Interpolation

The authors of [85] suggested to compensate the phase rotation introduced by the residual STO before applying the normal linear interpolation. A differential phase estimate is obtained by

$$\begin{aligned} \hat{\phi} &= \arg \left\{ \sum_{k'=1}^{N_p-1} \hat{a}_{k'k'}^{\text{LS}} \cdot \hat{a}_{(k'+1)(k'+1)}^{\text{LS}*} \right\} \\ &= \arg \left\{ \alpha^2 H_{l',k'} H_{l',k'+1}^* e^{-i\frac{2\pi D\theta}{N}} \right\} \\ &\approx -\frac{2\pi D\theta}{N} \end{aligned} \quad (5.15)$$

where $k' \in \{1, \dots, N_p\}$ denotes the RS subcarrier indices and D the spacing between two adjacent RS subcarriers. This results in an STO estimate $\hat{\theta} = -\frac{\hat{\phi} \cdot N}{2\pi D}$. Thus, the phase rotation of LS estimates on the RS subcarriers can be compensated. Then, Equation (5.7) is applied to the phase compensated channel estimates.

The MSE curves of the LS estimator with the two alternative interpolators are displayed in Figure 5.5. Although with a slight difference in terms of the error floor in the ICI/ISI-free region, the two modified interpolators are capable of compensating most of the interpolation errors in an imperfect symbol timing scenario.

5.2.2. LMMSE Channel Estimator

An LMMSE estimator minimizes the estimation error. Therefore, it is in general believed that it outperforms an LS estimator. Following the notation from Equa-

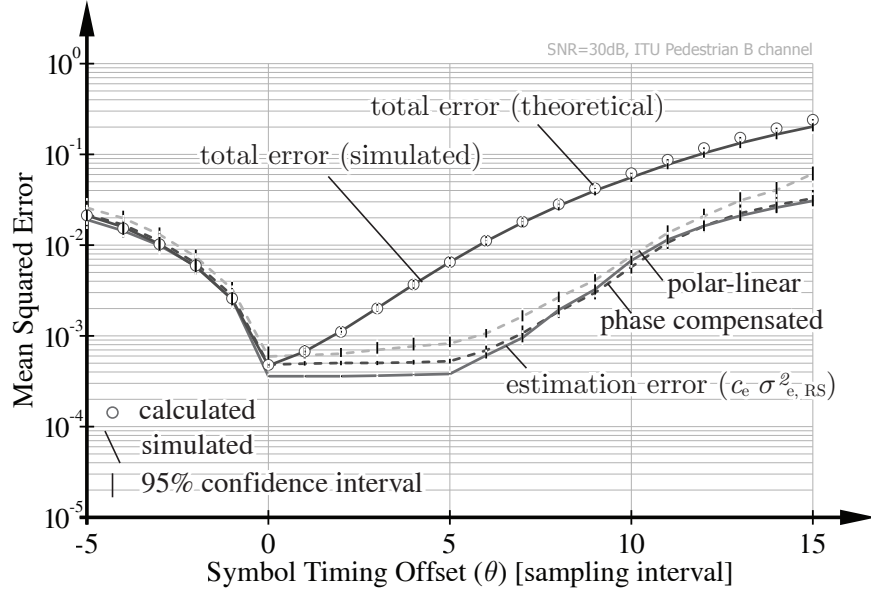


Figure 5.5: MSE of the LS channel estimator versus STOs with the alternative linear interpolators.

tions (5.1) to (5.4), an LMMSE estimator is given by

$$\begin{aligned}
 \hat{\mathbf{a}}_{l'}^{\text{LMMSE}} &= \arg \min_{\hat{\mathbf{a}}_{l'}} \|\hat{\mathbf{a}}_{l'} - \mathbf{a}_{l'}\|_2^2 \\
 &= \arg \min_{\mathbf{C}} \left\| \mathbf{C} \cdot \hat{\mathbf{a}}_{l',\text{RS}}^{\text{LS}} - \mathbf{a}_{l'} \right\|_2^2 \\
 &= \underbrace{\mathbf{R}_{aa'}^{(D)} \left(\mathbf{R}_{a'a'}^{(D)} + \sigma_w^2 \cdot \mathbf{I} \right)^{-1}}_{\mathbf{C}} \cdot \hat{\mathbf{a}}_{l',\text{RS}}^{\text{LS}}, \tag{5.16}
 \end{aligned}$$

where $\mathbf{R}_{a'a'}^{(D)} = \mathbb{E} \left\{ \mathbf{a}_{l',\text{RS}} \mathbf{a}_{l',\text{RS}}^H \right\}$ represents the channel autocorrelation matrix on the RS subcarriers. Correspondingly, $\mathbf{R}_{aa'}^{(D)} = \mathbb{E} \left\{ \mathbf{a}_{l'} \mathbf{a}_{l',\text{RS}}^H \right\}$ is the cross-correlation matrix between the entire channel and the RS subcarriers. They both can be regarded as the submatrices of $\mathbf{R}_{aa}^{(D)}$. The superscript (D) indicates this a-priori knowledge on the channel statistics is used for designing the channel estimator. The term σ_w^2 denotes the average power of the combined interference and noise term.

Estimation Performance

The theoretical MSE of an LMMSE estimator is well known as

$$\mathbb{E} \left\{ \left\| \hat{\mathbf{a}}_{l'}^{\text{LMMSE}} - \mathbf{a}_{l'} \right\|_2^2 \right\} = \mathbf{R}_{aa}^{(A)} - \mathbf{R}_{aa'}^{(A)} \cdot \mathbf{C}^H - \mathbf{C} \cdot \mathbf{R}_{a'a}^{(A)} + \mathbf{C} \left(\mathbf{R}_{a'a'}^{(A)} + \sigma_w^2 \mathbf{I} \right) \mathbf{C}^H, \tag{5.17}$$

where $\mathbf{R}_{aa}^{(A)}$ is the actual channel autocorrelation matrix. This actual statistics is dependent on the instantaneous residual STO, expressed as

$$\mathbf{R}_{aa}^{(A)} = \alpha^2 \cdot \mathbf{E}(\theta) \mathbf{R}_{hh} \mathbf{E}(\theta)^H, \quad (5.18)$$

though θ is unknown. Ideally, with the perfect knowledge of the actual second-order channel statistics, the MSE in Equation (5.17) is minimized, which means $\mathbf{R}_{aa}^{(A)} = \mathbf{R}_{aa}^{(D)}$. Any mismatch will result in a degradation in the estimation performance. Numerically, such a degradation is shown in Figure 5.6 where a perfect symbol timing $\theta = 0$ is assumed by the LMMSE estimator, i.e., $\mathbf{R}_{aa}^{(D)} = \mathbf{R}_{hh} = N \cdot \mathbf{F} \mathbf{X}_D \mathbf{F}^H$, where \mathbf{F} is the unitary FFT matrix. The diagonal matrix \mathbf{X}_D contains the channel PDP on its diagonal.

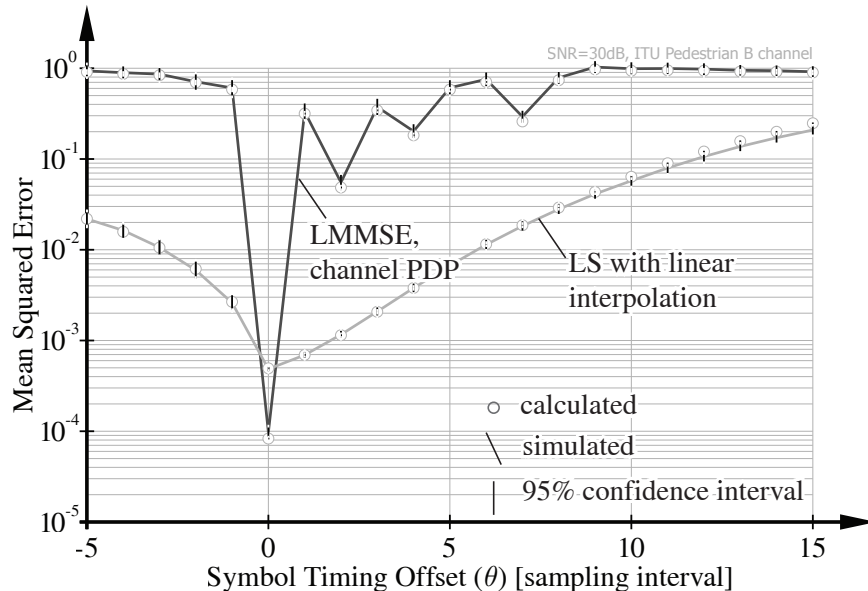


Figure 5.6: MSE of the LMMSE channel estimator against STOs.

In Figure 5.6, the MSE curve of an LS estimator with linear interpolation in Figure 5.3 is shown as a reference. Although the LMMSE estimator provides a smaller estimation error at zero STO, the estimation performance is rather sensitive to the symbol timing errors; in other words, it strongly depends on the accuracy of the a-priori knowledge of the actual channel statistics. Therefore, in a practical system where a perfect symbol timing is not guaranteed, an LMMSE estimator needs to be treated carefully.

Robust LMMSE Estimator

The idea of a robust LMMSE estimator was proposed in [86] in order to combat the mismatch between the estimator-to-channel statistics. The authors showed that by

using a channel autocorrelation matrix derived from a uniform channel PDP, the LMMSE becomes insensitive to the actual channel statistics and therefore, it can significantly improve the system performance. The authors in [79] suggested that a design with a uniform PDP also provides a certain tolerance to residual STOs. However, the mismatch between the actual channel length and the length of the uniform PDP used for design now becomes another issue.

In case a robust design is utilized, the a-priori knowledge of the channel autocorrelation matrix $\mathbf{R}_{aa}^{(D)}$ in Equation (5.16) is assumed to be

$$\mathbf{R}_{aa}^{(D)} = \frac{N}{L'} \cdot \mathbf{F} \cdot \begin{bmatrix} \mathbf{I}_{L'} & \mathbf{0} \\ \mathbf{0} & \mathbf{0} \end{bmatrix} \cdot \mathbf{F}^H, \quad (5.19)$$

where the identity matrix $\mathbf{I}_{L'}$ is of size $L' \times L'$. The effective maximum channel excess delay is denoted by $L' = L + \theta_{\max}$, where L is the true maximum channel excess delay and θ_{\max} the maximum residual STO that the estimator is able to cope with.

As an example, we simulate the estimation performance of robust LMMSE estimators with designs using various a-priori knowledge. The MSE curves are demonstrated in Figure 5.7. The true maximum channel excess delay of an ITU Pedestrian B channel in the simulation is eight sampling intervals. As shown in Figure 5.7, when a uniform PDP of length eight ($\theta_{\max} = 0$) is applied, the estimator shows the least tolerance to the residual STO. The larger L' is, the more robust the estimator is to an STO, although this comes at the expense of the estimation performance in the valid symbol timing region. In order to combat the whole set of the STOs $\theta \in [-5, 15]$ in the experiment, the following $\mathbf{R}_{aa}^{(D)}$ is utilized:

$$\mathbf{R}_{aa}^{(D)} = \frac{N}{L + (15 + 5)} \cdot \mathbf{F} \cdot \begin{bmatrix} \mathbf{I}_{L+15} & \mathbf{0} & \mathbf{0} \\ \mathbf{0} & \mathbf{0} & \mathbf{0} \\ \mathbf{0} & \mathbf{0} & \mathbf{I}_5 \end{bmatrix} \cdot \mathbf{F}^H. \quad (5.20)$$

The LMMSE with this PDP of length $L' = 28$ shows its robustness against the STOs within the range. However, the overall performance is comparable to those of the LS schemes with modified interpolators. Till here, it can be concluded that the performance gain promised by an LMMSE is rather controversy in a practical system unless an appropriate STO distribution is known. Therefore, the later performance evaluation is constrained to the LS case.

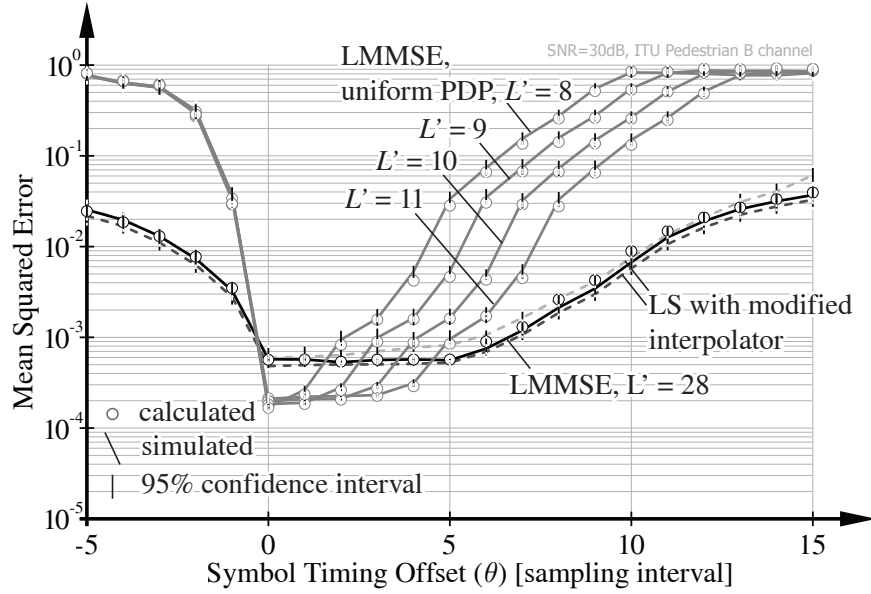


Figure 5.7: MSE of the robust LMMSE channel estimator against STOs. The maximum channel excess delay $L = 8$.

5.3. Post-Equalization SINR Evaluation

For a coherent OFDM system, the residual STO degrades the overall performance in a two-fold manner, namely the interferences to the received signal and the additional estimation error imposed on the imperfect channel knowledge. In this section, we consider a Zero Forcing (ZF) receiver and derive the post-equalization SINR subject to the residual STO. This analysis on the one hand implies the impact of imperfect symbol timing on a practical OFDM system; on the other hand, it can be used as a physical layer performance model in higher layer simulations.

5.3.1. Perfect Channel Knowledge

In this section, a closed form expression of the post-equalization SINR of an LTE DL transmission under imperfect symbol timing is derived.

Given the received signal in Equation (2.34), an RS-based linear channel estimator is merely able to estimate the diagonal elements of the effective channel matrix $\mathbf{A}(\theta)$, namely \mathbf{A}_{kk} . Starting with a simple assumption of perfect channel knowledge, the ZF equalizer for subcarrier k can be expressed as

$$\mathbf{G}_k = \mathbf{A}_{kk}^\dagger = (\mathbf{A}_{kk}^H \mathbf{A}_{kk})^{-1} \cdot \mathbf{A}_{kk}^H. \quad (5.21)$$

Table 5.1.: Simulation Parameters

Parameter	Value
Bandwidth	1.4 MHz
FFT size (N)	128
Number of data subcarriers (N_{tot})	72
CP length (N_g)	normal ($4.7 \mu\text{s}$) [9]
Sampling frequency	1.92 MHz
Subcarrier spacing	15 kHz
Transmission setting	$1 \times 1, 2 \times 2$ OLSM
Channel model	ITU PedB [15]
Channel state information	perfect
Equalizer	ZF

Table 5.2.: PDP of ITU Pedestrian B channel model [15]

Excess tap delay (ns)	0	200	800	1200	2300	3700
Relative power (dB)	0	-0.9	-4.9	-8.0	-7.8	-23.9

The output signal of such an equalizer can be written as

$$\begin{aligned}
 \hat{\mathbf{x}}_{l,k} &= \mathbf{G}_k \cdot \mathbf{r}_{l,k} \\
 &= \mathbf{x}_{l,k} + \underbrace{\mathbf{G}_k \sum_{p \neq k} \mathbf{A}_{kp} \mathbf{x}_{l,p}}_{\text{ICI}} + \underbrace{\mathbf{G}_k \sum_p \mathbf{B}_{kp} \mathbf{x}_{\text{int},p}}_{\text{ISI}} + \underbrace{\mathbf{G}_k \mathbf{v}_{l,k}}_{\text{noise}}.
 \end{aligned} \tag{5.22}$$

We obtain a closed form expression of the post-equalization SINR, expressed as

$$\begin{aligned}
 \text{SINR}_{l,k}^{(m)} &= \frac{[\mathbf{x}_{l,k} \mathbf{x}_{l,k}^H]_{(m,m)}}{[(\hat{\mathbf{x}}_{l,k} - \mathbf{x}_{l,k})(\hat{\mathbf{x}}_{l,k} - \mathbf{x}_{l,k})^H]_{(m,m)}} \\
 &= \frac{\sigma_s^2}{\sigma_s^2 \left[\sum_{p \neq k} \mathbf{G}_k \mathbf{A}_{kp} \mathbf{A}_{kp}^H \mathbf{G}_k^H \right]_{(m,m)} + \sigma_s^2 \left[\sum_p \mathbf{G}_k \mathbf{B}_{kp} \mathbf{B}_{kp}^H \mathbf{G}_k^H \right]_{(m,m)} + \sigma_v^2 [\mathbf{G}_k \mathbf{G}_k^H]_{(m,m)}},
 \end{aligned} \tag{5.23}$$

where σ_s^2 and σ_v^2 denote the averaged signal and the noise power on each Receiver (RX) antenna. The operation $[\cdot]_{(i,j)}$ extracts the element on the i -th row and j -th column. Since $\mathbf{A}_{kp}, \mathbf{B}_{kp}$ are only dependent on the channel realization and the system parameters, the post-equalization SINR under an arbitrary STO θ can be exclusively determined using Equation (5.23) for a given channel realization. In the following, Equation (5.23) is validated by standard compliant Monte-Carlo simulations using the Vienna LTE Link Level simulator [60]. Simulation parameters are listed in Table 5.1 and Table 5.2.

In the simulation, 500 LTE subframes were transmitted and the post-equalization SINRs were measured. With the 500 stored channel realizations, the post-equalization SINRs were calculated using Equation (5.23). Since the system performance is more sensitive to the interference at the high SNR region, SNR was fixed at 30 dB. A series of STO $\theta \in [-5, 15]$ was introduced. Corresponding results are shown in Figure 5.8 in terms of the so-called wide-band SINR which is an average over 72 data subcarriers.

In Figure 5.8, the curves obtained from the closed form expression agree well with those from the simulation. In the region of $\theta < 0$, namely where a late timing occurs, a sharp drop can be observed; whereas when an early timing occurs, the CP alleviates the situation. Although the CP has a length of $4.7 \mu\text{s}$, corresponding to nine sampling periods in this case, given the channel PDP in Table 5.2, ISI and ICI arises at the beginning of the CPs. Therefore, an SINR degradation appears after the second sample and becomes visible after the fifth.

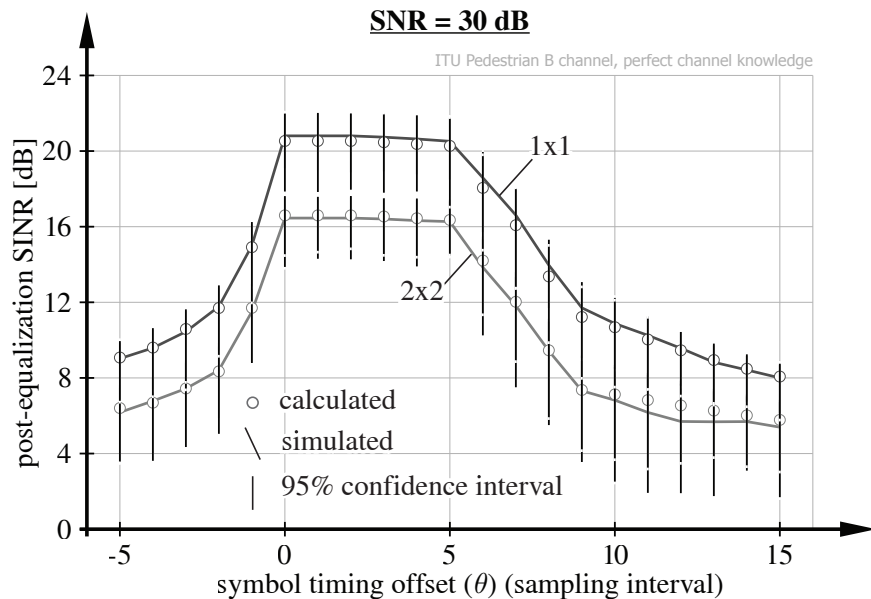


Figure 5.8: Calculated and simulated post-equalization SINR under STOs in ITU Pedestrian B channel. The 95 % confidence intervals are relatively large which can be explained by the strong frequency selectivity induced by the multi-path channel.

5.3.2. Imperfect Channel Knowledge

SINR models have become of interest, since they enable efficient system level simulations. The accuracy of system level simulations relies on the SINR models which abstract the link level behavior with only low complexity [87]. In [88], the authors investigated the effect of channel estimation error on the performance of MIMO ZF receiver in uncorrelated Rayleigh flat fading channels. A tight approximation for the

post-equalization SINR was derived in closed-form by modeling the estimation error as independent complex Gaussian random variables. However, it can be shown that for an LS channel estimator with linear interpolation, this model is only accurate when the interpolation error is relatively small. When an STO occurs, especially for $\theta > 0$, this model fails to fit the reality.

In order to obtain an accurate SINR model that describes the physical layer behavior in a practical scenario, we take a residual STO as well as an LS channel estimator into account and derive the effective SINR after a ZF equalizer on the data subcarriers.

Continue with Equation (5.21), when an imperfect channel knowledge is considered, the ZF equalizer for a data subcarrier k is constructed using the estimated channel frequency response, namely

$$\mathbf{G}_k = \hat{\mathbf{A}}_{kk}^\dagger = (\hat{\mathbf{A}}_{kk}^H \hat{\mathbf{A}}_{kk})^{-1} \cdot \hat{\mathbf{A}}_{kk}^H. \quad (5.24)$$

Given \hat{a}_{kk} in Equation (5.7), we model the channel estimate on a data position as

$$\hat{\mathbf{A}}_{kk} = \bar{\mathbf{A}}_{kk} + \mathbf{E}_{kk}, \quad (5.25)$$

where the $N_R \times N_T$ matrix $\bar{\mathbf{A}}_{kk}$ is the linearly interpolated channel matrix and \mathbf{E}_{kk} denotes the estimation error matrix. The entries in \mathbf{E}_{kk} are modeled as independent complex Gaussian random variables with zero-mean and variance $c_e \cdot \sigma_{e,RS}^2$ in Equation (5.9).

The post-equalization interference and noise can be calculated as

$$\begin{aligned} \hat{\mathbf{x}}_{l,k} - \mathbf{x}_{l,k} &= \mathbf{G}_k \cdot \mathbf{r}_{l,k} - \mathbf{x}_{l,k} \\ &= \underbrace{\left[(\hat{\mathbf{A}}_{kk}^H \hat{\mathbf{A}}_{kk})^{-1} \hat{\mathbf{A}}_{kk}^H \mathbf{A}_{kk} - \mathbf{I} \right]}_{\mathbf{Q}_k} \mathbf{x}_{l,k} + \mathbf{G}_k \cdot \sum_{p \neq k} \mathbf{A}_{kp} \mathbf{x}_{l,p} + \\ &\quad + \mathbf{G}_k \cdot \sum_p \mathbf{B}_{kp} \mathbf{x}_{\text{int},p} + \mathbf{G}_k \cdot \mathbf{v}_{l,k}, \end{aligned} \quad (5.26)$$

where

$$\begin{aligned} \mathbf{Q}_k &= \left(\hat{\mathbf{A}}_{kk}^H \hat{\mathbf{A}}_{kk} \right)^{-1} \hat{\mathbf{A}}_{kk}^H \left(\mathbf{A}_{kk} - \hat{\mathbf{A}}_{kk} \right) \\ &= \mathbf{G}_k \cdot \left(\underbrace{\mathbf{A}_{kk} - \bar{\mathbf{A}}_{kk}}_{\text{interpolation error}} - \mathbf{E}_{kk} \right). \end{aligned} \quad (5.27)$$

Since the estimation error and the interpolation error are uncorrelated from each

other, the total energy of the resulting interference and noise becomes

$$\begin{aligned}
 E_{I+N} &= \mathbb{E}\left\{\mathbf{Q}_k \cdot \underline{\mathbf{x}}_{l,k} \underline{\mathbf{x}}_{l,k}^H \cdot \mathbf{Q}_k^H\right\}_{(m,m)} + \mathbb{E}\left\{\sum_{p \neq k} \mathbf{G}_k \mathbf{A}_{kp} \mathbf{x}_{l,p} \mathbf{x}_{l,p}^H \mathbf{A}_{kp}^H \mathbf{G}_k^H\right\}_{(m,m)} + \\
 &\quad + \mathbb{E}\left\{\sum_p \mathbf{G}_k \mathbf{B}_{kp} \mathbf{x}_{\text{int},p} \mathbf{x}_{\text{int},p}^H \mathbf{B}_{kp}^H \mathbf{G}_k^H\right\}_{(m,m)} + \mathbb{E}\left\{\mathbf{G}_k \underline{\mathbf{v}}_{l,k} \underline{\mathbf{v}}_{l,k}^H \mathbf{G}_k^H\right\}_{(m,m)} \\
 &= \sigma_s^2 \cdot \left[\mathbf{G}_k (\mathbf{A}_{kk} - \bar{\mathbf{A}}_{kk}) (\mathbf{A}_{kk} - \bar{\mathbf{A}}_{kk})^H \mathbf{G}_k^H\right]_{(m,m)} + \\
 &\quad + \sigma_s^2 \cdot \left[\mathbf{G}_k \mathbf{E}_{kk} \mathbf{E}_{kk}^H \mathbf{G}_k^H\right]_{(m,m)} + \sigma_s^2 \cdot \left[\sum_{p \neq k} \mathbf{G}_k \mathbf{A}_{kp} \mathbf{A}_{kp}^H \mathbf{G}_k^H\right]_{(m,m)} + \\
 &\quad + \sigma_s^2 \cdot \left[\sum_p \mathbf{G}_k \mathbf{B}_{kp} \mathbf{B}_{kp}^H \mathbf{G}_k^H\right]_{(m,m)} + \sigma_v^2 \cdot \left[\mathbf{G}_k \mathbf{G}_k^H\right]_{(m,m)} \quad (5.28)
 \end{aligned}$$

which results in the post equalization signal power

$$E_S = \sigma_s^2 \cdot \left\{\mathbf{G}_k \left[\mathbf{A}_{kk} \mathbf{A}_{kk}^H - (\mathbf{A}_{kk} - \bar{\mathbf{A}}_{kk}) (\mathbf{A}_{kk} - \bar{\mathbf{A}}_{kk})^H - \mathbf{E}_{kk} \mathbf{E}_{kk}^H\right] \mathbf{G}_k^H\right\}_{(m,m)}. \quad (5.29)$$

The post-equalization SINR therefore can be expressed as

$$\text{SINR}_{l,k}^{(m)} = \frac{E_S}{E_{I+N}}. \quad (5.30)$$

5.4. Coded Throughput

The achievable throughput of a system is determined by the post-equalization SINR. Specifically for the LTE DL, such a mapping can be approximated using the Bit-Interleaved Coded Modulation (BICM) capacity as shown in Section 4.3.3. In Figure 5.9, a throughput evaluation of using the Vienna LTE link level simulator can be found. Its parameter setting follows Table 5.1 and Table 5.2.

As shown in Figure 5.9, the residual STOs have a strong influence on the link performance. This is confirmed in fact already by the MSE analysis of the LS channel estimator; ICI and ISI causes the degradation in the late timing region ($\theta < 0$) while the additional channel estimation error dominates the loss in the early timing region ($\theta > 0$).

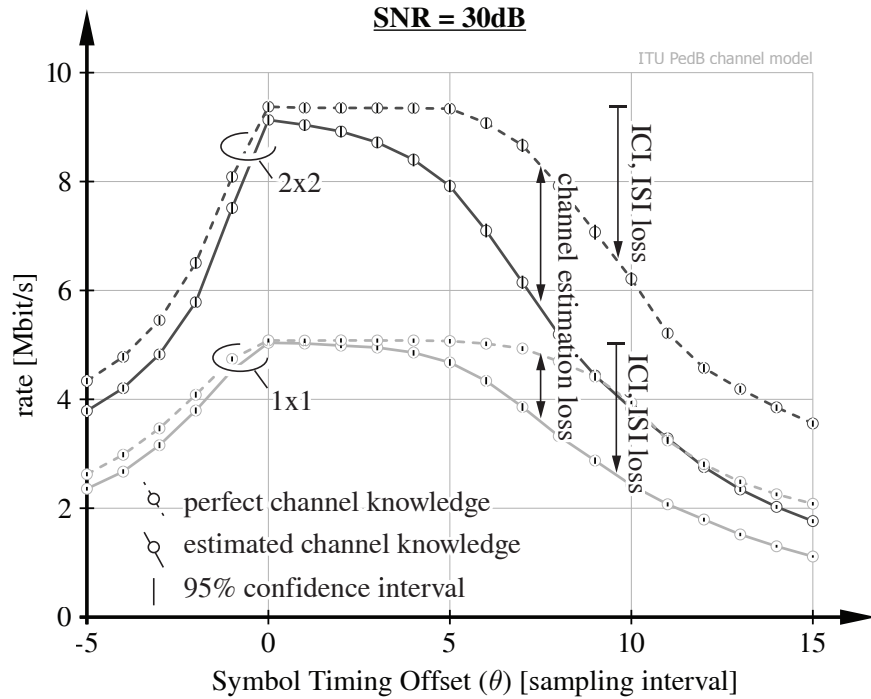


Figure 5.9: Coded throughput of the LTE DL with STOs at 30 dB SNR in ITU Pedestrian B channel. Comparison between the perfect channel knowledge and the estimated channel knowledge cases are shown.

5.5. Conclusion

This chapter reveals the impact of a fixed residual STO on the LTE DL. Although neither a time-variant distortion or a physical impairment, an offset in the OFDM symbol timing introduces significant ICI and ISI especially when a late timing occurs. In addition, an STO induces another fold of degradation in the state-of-the-art pilot symbol based channel estimators which rely on the a-priori knowledge of the channel statistics. This accordingly causes incremental performance loss in terms of the system throughput.

Since the investigation in this chapter does not include the estimation performance of any STO estimator, the results are limited to the fixed STO case in a relatively high SNR. Nevertheless, the overall performance loss is determined not only on a potential STO but also the probability of such an STO occurs. Therefore, a fair evaluation requires a distribution function of the detection error of the STO. Such a distribution function can also be utilized as the a-priori knowledge to improve the signal processing algorithm design on the receiver side.

6. Summary

6.1. Contributions

This thesis aims to expose the potential performance loss due to the synchronization errors in the two practical Orthogonal Frequency Division Multiplexing (OFDM) systems, i.e., the Worldwide Inter-operability for Microwave Access (WiMAX) OFDM physical layer and the Long Term Evolution (LTE) Downlink (DL). In contrast to related works in this field, the full physical layer instead of an individual synchronization unit is considered. The main contributions in this thesis are summarized in the following paragraphs.

In Chapter 3, the differential estimator for the Residual Frequency Offset (RFO) is optimized in order to exploit all the eight pilot subcarriers in WiMAX. The Cramér-Rao Lower Bound (CRLB) given these pilot subcarriers is derived in Appendix B. The optimized differential estimator approximately attains the CRLB. In addition, this estimator is modified in order to have an extended estimation range. All these aspects account for a significant improvement in terms of the estimation performance. However, such improvement becomes negligible in terms of the coded throughput. Such a result comes to be the original motivation for the performance evaluation in Chapter 4 and Chapter 5.

In Chapter 4, we propose a prediction model for the throughput loss from an imperfect carrier frequency synchronization in the LTE DL. This model provides a direct mapping between a residual Carrier Frequency Offset (CFO) estimation error and the corresponding loss in terms of coded throughput, taking into account a Zero Forcing (ZF) equalizer and the Modulation and Coding Scheme (MCS) defined in the LTE standard. Validated by extensive standard compliant link level simulations, this analytical model on the one hand implies the requirement on the accuracy of the

CFO estimation; on the other hand, provides an evaluation tool for the frequency synchronization algorithm designer.

In Chapter 5, a quantitative analysis of the performance loss due to a residual Symbol Timing Offset (STO) is presented. Unlike the late timing region severely interfered by the Inter-Carrier Interference (ICI) and Inter-Symbol Interference (ISI), the early timing region is highly affected by the incremental channel estimation error, although this part is hidden when the pre-equalization Signal to Interference-plus-Noise Ratio (SINR) is taken as the performance measure. Therefore, also an absolutely accurate symbol timing is required in a practical OFDM system.

To sum up, although it is generally believed that the CFO and STO cause significant ICI and ISI, other effects, i.e., the Common Phase Error (CPE) from a CFO and the additional phase variation from an STO induces negative impacts as well. Due to the overall system design constraint, these impacts may interfere the performance of other signal processing units and further degrades the system performance. These side-effects to some extent raise the requirement of the synchronization accuracy.

6.2. Outlook

When developing a wireless communication system, researchers in the academical world focus on the potential gain and invent novel techniques in order to achieve higher performance. However when going to the real world, a new technique must face many practical challenges which are usually zeroed out in simulation based experiments. In this work, we tried to reach one step closer to the real world. Although besides a CFO and a STO, a practical OFDM system will experience a lot more physical impairments, for instance, sampling frequency offset, I/Q imbalance, oscillator phase noise and Doppler frequency shift. Their individual impacts, as well as the cross-effects all need to be considered.

Specifically, in the scope of this work, since the investigation of the symbol timing aspects did not include the error performance analysis of any STO estimator, the evaluation lacks some insight compared to that of the CFO. Intuitively, given an arbitrary symbol timing offset estimator, a lower error probability at high Signal to Noise Ratio (SNR) while a higher error probability at lower SNR can be expected. Thus, the overall throughput loss is dependent not only on a potential symbol timing offset but also on the probability that such an offset occurs. Nevertheless, the latter is not considered in this thesis.

Furthermore, this work investigates the impact of a residual CFO or an STO individually. Although an STO estimator is usually designed to be robust to relatively large CFO, how these two interfere each other and further influence the system

performance is also considered to be an open issue.

Bibliography

- [1] IEEE, “**IEEE standard for local and metropolitan area networks; part 16: Air interface for fixed broadband wireless access systems, IEEE Std. 802.16-2004**,” Oct. 2004.
<http://standards.ieee.org/getieee802/download/802.16-2004.pdf>
- [2] Technical Specification Group Radio Access Network, “**E-UTRA; LTE physical layer – general description**,” 3GPP, Tech. Rep. TS 36.201 Version 9.1.0, Mar. 2010.
- [3] B. Stantchev and G. Fettweis, “**Time-variant distortion in OFDM**,” *IEEE Communications Letters*, vol. 4, pp. 312–314, Oct. 2000.
- [4] Y. Mostofi and D. C. Cox, “**Mathematical analysis of the impact of time synchronization errors on the performance of an OFDM system**,” *IEEE Transactions on Communications*, vol. 54, no. 2, pp. 226–230, Feb. 2006.
- [5] M. C. Jeruchim, P. Balaban, and K. S. Shanmugan, **Simulation of Communication Systems: Modeling, Methodology and Techniques**, 2nd ed. Kluwer Academic/Plenum Publisher, New York, 2000. ISBN: 0306462672.
- [6] “**WiMAX simulator homepage**.”
<http://www.nt.tuwien.ac.at/wimaxsimulator/>
- [7] “**LTE simulator homepage**.”
<http://www.nt.tuwien.ac.at/ltesimulator/>
- [8] IEEE, “**IEEE standard for local and metropolitan area networks; part 16: Air interface for fixed broadband wireless access systems, IEEE Std. 802.16-2009**,” May 2009.
<http://standards.ieee.org/getieee802/download/802.16-2009.pdf>
- [9] Technical Specification Group Radio Access Network, “**E-UTRA; physical channels and modulation**,” 3GPP, Tech. Rep. TS 36.211 Version 9.1.0, Mar. 2010.
- [10] P. H. Moose, “**A technique for orthogonal frequency division multiplexing frequency offset correction**,” *IEEE Transactions on Communications*, vol. 42, no. 10, pp. 2908–2914, Oct. 1994.
- [11] J. Lee, H.-L. Lou, D. Toumpakaris, and J. Cioffi, “**SNR analysis of OFDM systems in the presence of carrier frequency offset for fading channels**,” *IEEE Transactions on Wireless Communications*, vol. 5, no. 12, pp. 3360–3364, Dec. 2006.
- [12] Y. Mostofi and D. Cox, “**Mathematical analysis of the impact of timing synchronization errors on the performance of an OFDM system**,” *IEEE Transactions on Communications*, vol. 54, no. 2, pp. 226–230, Feb. 2006.
- [13] M. Speth, S. Fechtel, G. Fock, and H. Meyr, “**Optimum receiver design for wireless broadband systems using OFDM. part I**,” *IEEE Transactions on Communications*, vol. 47, no. 11, pp. 1668–1677, Nov. 1999.
- [14] M. Wang, L. Xiao, T. Brown, and M. Dong, “**Optimal symbol timing for OFDM wireless communications**,” *IEEE Transactions on Wireless Communications*, vol. 8, no. 10, pp. 5328–5337, Oct. 2009, doi: 10.1109/TWC.2009.090263.

-
- [15] Members of ITU, “**Recommendation ITU-R M.1225: Guidelines for evaluation of radio transmission technologies for IMT-2000,**” International Telecommunication Union (ITU), Tech. Rep., 1997.
- [16] J. G. Andrews, A. Ghosh, and R. Muhamed, **Fundamentals of WiMAX - Understanding Broadband Wireless Networking**, 1st ed. Pearson Educations, Inc., 2007. ISBN: 0132225522.
- [17] C. Mehlführer, S. Caban, and M. Rupp, “**Experimental evaluation of adaptive modulation and coding in MIMO WiMAX with limited feedback,**” *EURASIP Journal on Advances in Signal Processing, Special Issue on MIMO Systems with Limited Feedback*, vol. 2008, Article ID 837102, 2008.
http://publik.tuwien.ac.at/files/pub-et_13762.pdf
- [18] C. Mehlführer, S. Caban, and M. Rupp, “**An accurate and low complex channel estimator for OFDM WiMAX,**” in *Proc. Third International Symposium on Communications, Control, and Signal Processing (ISCCSP 2008)*, pp. 922–926, St. Julians, Malta, Mar. 2008, doi: 10.1109/ISCCSP.2008.4537355.
http://publik.tuwien.ac.at/files/pub-et_13650.pdf
- [19] C. Mehlführer, “**Measurement-based performance evaluation of WiMAX and HSDPA,**” Ph.D. dissertation, Institute of Telecommunications, Vienna University of Technology (TUWien), Austria, 2009.
- [20] S. Caban, “**Testbed-based evaluation of mobile communication systems,**” Ph.D. dissertation, Institute of Telecommunications, Vienna University of Technology (TUWien), Austria, 2009.
- [21] S. Caban, C. Mehlführer, R. Langwieser, A. L. Scholtz, and M. Rupp, “**Vienna MIMO testbed,**” *EURASIP Journal on Applied Signal Processing*, vol. 2006, Article ID 54868, 2006.
- [22] S. Caban, A. Disslbach-Fink, J. A. García-Naya, and M. Rupp, “**Synchronization of wireless radio testbed measurements,**” in *Proc. 2011 IEEE International Instrumentation and Measurement Technology Conference (I2MTC2011)*, Binjiang, Hangzhou, China, May 2011.
http://publik.tuwien.ac.at/files/PubDat_201643.pdf
- [23] T. Schmidl and D. Cox, “**Robust frequency and timing synchronization for OFDM,**” *IEEE Transactions on Communications*, vol. 45, no. 12, pp. 1613–1621, Dec. 1997.
- [24] M. Morelli and U. Mengali, “**An improved frequency offset estimator for OFDM applications,**” in *Communication Theory Mini-Conference, 1999*, pp. 106–109, Vancouver, Canada, June 1999.
- [25] M. Speth, S. Fechtel, G. Fock, and H. Meyr, “**Optimum receiver design for OFDM-based broadband transmission. II. a case study,**” *IEEE Transactions on Communications*, vol. 49, no. 4, pp. 571–578, Apr. 2001.
- [26] H. Minn, V. K. Bhargava, and K. B. Letaief, “**A robust timing and frequency synchronization for OFDM systems,**” *IEEE Trans. on Wireless Com.*, vol. 2, no. 4, pp. 822–839, July 2003.
- [27] J. Li, G. Liu, and G. B. Giannakis, “**Carrier frequency offset estimation for OFDM-based WLANs,**” *IEEE Signal Processing Letters*, vol. 8, no. 3, pp. 80–82, Mar. 2001.
- [28] S.-Y. Liu and J.-W. Chong, “**A study of joint tracking algorithms of carrier frequency offset and sampling clock offset for OFDM-based WLANs,**” in *IEEE 2002 International Conference on Communications, Circuits and Systems and West Sino Expositions*, vol. 1, pp. 109–113, June 2002.
- [29] V. Jimenez, M.-G. Garcia, F. Serrano, and A. Armada, “**Design and implementation of synchronization and AGC for OFDM-based WLAN receivers,**” *IEEE Transactions on Consumer*
-

- Electronics*, vol. 50, no. 4, pp. 1016–1025, Nov. 2004.
- [30] T. Schenk and A. van Zelst, “**Frequency synchronization for MIMO OFDM wireless LAN systems**,” in *IEEE 58th Vehicular Technology Conference, 2003. VTC 2003-Fall. 2003*, vol. 2, pp. 781–785, Oct. 2003.
- [31] A. van Zelst and T. Schenk, “**Implementation of a MIMO OFDM-based wireless LAN system**,” *IEEE Transactions on Signal Processing*, vol. 52, no. 2, pp. 483–494, Feb. 2004, doi: 10.1109/TSP.2003.820989.
- [32] J. J. van de Beek, M. Sandell, and P. O. Borjesson, “**ML estimation of time and frequency offset in OFDM system**,” *IEEE Trans. on Signal Processing*, vol. 45, no. 7, pp. 1800–1805, July 1997.
- [33] R. Mo, Y. H. Chew, T. T. Tjhung, and C. C. Ko, “**A new blind joint timing and frequency offset estimator for OFDM systems over multipath fading channels**,” *IEEE Transactions on Vehicular Technology*, vol. 57, no. 5, pp. 2947–2957, Sept. 2008.
- [34] U. Tureli, H. Liu, and M. Zoltowski, “**OFDM blind carrier offset estimation: ESPRIT**,” *IEEE Transactions on Communications*, vol. 48, no. 9, pp. 1459–1461, Sept. 2000.
- [35] H. Liu and U. Tureli, “**A high-efficiency carrier estimator for OFDM communications**,” *IEEE Communications Letters*, vol. 2, no. 4, pp. 104–106, Apr. 1998.
- [36] X. Ma, C. Tepedelenlioglu, G. B. Giannakis, and S. Barbarossa, “**Non-data-aided carrier offset estimators for OFDM with null subcarriers: identifiability, algorithms and performance**,” *IEEE Journals on Selected Areas*, vol. 19, no. 12, pp. 2504–2515, Dec. 2001.
- [37] H. Bölcskei, “**Blind estimation of symbol timing and carrier frequency offset in wireless OFDM systems**,” *IEEE Trans. on Communications*, vol. 49, no. 6, pp. 988–999, June 2001.
<http://www.nari.ee.ethz.ch/commth/pubs/p/synch>
- [38] Y. Yao and G. Giannakis, “**Blind carrier frequency offset estimation in SISO, MIMO, and multiuser OFDM systems**,” *IEEE Trans. on Com.*, vol. 53, no. 1, pp. 173–183, Jan. 2005.
- [39] B. Chen and H. Wang, “**Maximum likelihood estimation of OFDM carrier frequency offset**,” in *IEEE International Conference on Communications, (ICC 2002)*, vol. 1, pp. 49–53, Apr. 2002.
- [40] C. Chen and J. Li, “**Maximum likelihood method for integer frequency offset estimation of OFDM systems**,” *Electronics Letters*, vol. 40, no. 13, pp. 813–814, June 2004.
- [41] M. Morelli and M. Moretti, “**Integer frequency offset recovery in OFDM transmissions over selective channels**,” *IEEE Transactions on Wireless Communications*, vol. 7, no. 12, pp. 5220–5226, Dec. 2008.
- [42] D. Toumpakaris, J. Lee, and H. Lou, “**Estimation of integer carrier frequency offset in OFDM systems based on the maximum likelihood principle**,” *IEEE Transactions on Broadcasting*, vol. 55, pp. 95–108, Mar. 2009.
- [43] H. Chen and G. Pottie, “**A comparison of frequency offset tracking algorithms for OFDM**,” in *Global Telecommunications Conference, 2003. GLOBECOM '03. IEEE*, vol. 2, pp. 1069–1073, Dec. 2003.
- [44] S. S. Das, R. V. Rajakumar, M. I. Rahman, A. Pal, F. H. P. Fitzek, O. Olsen, and R. Prasad, “**Low complexity residual phase tracking algorithm for OFDM-based WLAN systems**,” in *Proc. International Symposium on Communication Systems, Networks and Digital Signal Processing*, pp. 128–131, Newcastle, U. K., July 2004.
- [45] M. Sandell, D. McNamara, and S. Parker, “**Analysis of frequency-offset tracking in MIMO**

- OFDM systems,**” *IEEE Transactions on Communications,*, vol. 54, no. 8, pp. 1481–1489, Aug. 2006, doi: 10.1109/TCOMM.2006.878841.
- [46] Q. Wang, C. Mehlführer, and M. Rupp, “**Carrier frequency synchronization in the downlink of 3GPP LTE,**” in *Proceeding of the 21st Annual IEEE International Symposium on Personal, Indoor and Mobile Radio Communications (PIMRC’10)*, Istanbul, Turkey, Sept. 2010.
- [47] S. Caban, C. Mehlführer, M. Rupp, and M. Wrulich, **Evaluation of HSDPA and LTE: From Testbed Measurements to System Level Performance**, 1st ed. John Wiley & Sons, Ltd, 2012. ISBN: 9780470711927.
- [48] Technical Specification Group Radio Access Network, “**Requirements for evolved UTRA(E-UTRA) and evolved UTRAN(E-UTRAN);**” 3GPP, Tech. Rep. TS 25.913 Version 9.0.0, Dec. 2009.
- [49] Technical Specification Group Radio Access Network, “**Evolved universal terrestrial radio access (E-UTRA); base station (BS) radio transmission and reception,**” 3GPP, Tech. Rep. TS 36.104 Version 9.9.0, Sept. 2011.
- [50] D. Chu, “**Polyphase codes with good periodic correlation properties (corresp.)**,” *IEEE Transactions on Information Theory,*, vol. 18, no. 4, pp. 531–532, July 1972.
- [51] R. Frank, “**Comments on ” polyphase codes with good periodic correlation properties by chu” , david c.**” *IEEE Transactions on Information Theory,*, vol. 19, no. 2, p. 244, Mar. 1973.
- [52] S. Sesia, I. Toufik, and M. Baker, **LTE-The UMTS Long Term Evolution: From Theory to Practice**, 1st ed. John Wiley & Sons, Ltd, 2009. ISBN: 9780470697160.
- [53] T. Aoki and M. Sandell, “**Analysis of pilots for residual frequency offset estimation in MIMO OFDM systems,**” *IEEE Transactions on Wireless Communications,*, vol. 8, no. 3, pp. 1128–1132, Mar. 2009, doi: 10.1109/TWC.2009.090311.
- [54] K. Sathananthan and C. Tellambura, “**Probability of error calculation of OFDM systems with frequency offset,**” *IEEE Transactions on Communications,*, vol. 49, no. 11, pp. 1884–1888, Nov. 2001.
- [55] T. Pollet, M. Van Bladel, and M. Moeneclaey, “**BER sensitivity of OFDM systems to carrier frequency offset and wiener phase noise,**” *IEEE Transactions on Communications,*, vol. 43, no. 234, pp. 191–193, Feb. 1995.
- [56] P. Dharmawansa, N. Rajatheva, and H. Minn, “**An exact error probability analysis of OFDM systems with frequency offset,**” *IEEE Transactions on Communications,*, vol. 57, no. 1, pp. 26–31, Jan. 2009.
- [57] L. Rugini and P. Banelli, “**BER of OFDM systems impaired by carrier frequency offset in multipath fading channels,**” *IEEE Transactions on Wireless Communications,*, vol. 4, no. 5, pp. 2279–2288, Sept. 2005.
- [58] M. Krondorf, T. Liang, and G. Fettweis, “**Symbol error rate of OFDM systems with carrier frequency offset and channel estimation error in frequency selective fading channels,**” in *IEEE International Conference on Communications, (ICC 2007)*, pp. 5132–5136, June 2007.
- [59] M. Krondorf and G. Fettweis, “**OFDM link performance analysis under various receiver impairments.**” *EURASIP Journal on Wireless Communications and Networking*, vol. 2008, Article ID 145279, 2008.
- [60] C. Mehlführer, J. C. Ikuno, M. Šimko, S. Schwarz, M. Wrulich, and M. Rupp, “**The Vienna LTE Simulators - Enabling Reproducibility in Wireless Communications Research,**” *EURASIP Journal on Advances in Signal Processing*, 2011.

-
- [61] S. M. Kay, **Fundamentals of Statistical Signal Processing: Estimation Theory**, 1st ed. Prentice & Hall, Inc., 1994. ISBN: 0133457117.
- [62] Q. Wang, S. Caban, C. Mehlführer, and M. Rupp, “**Measurement based throughput evaluation of residual frequency offset compensation in WiMAX**,” in *Proc. 51st International Symposium ELMAR-2009*, Zadar, Croatia, Sept. 2009.
- [63] M. Šimko, “**Channel estimation for UMTS long term evolution**,” Master’s thesis, Institute of Telecommunications, Vienna University of Technology (TUWien), Austria, 2009.
- [64] Q. Wang and M. Rupp, “**Analytical link performance evaluation of LTE downlink with carrier frequency offset**,” in *Conference Record of the 45th Asilomar Conference on Signals, Systems and Computers, 2011 (Asilomar-2011)*, Pacific Grove, USA, Nov. 2011.
- [65] S. Schwarz, M. Šimko, and M. Rupp, “**On performance bounds for MIMO OFDM based wireless communication systems**,” in *Proc. IEEE Signal Processing Advances in Wireless Communications SPAWC 2011*, June 2011.
- [66] G. Caire, G. Taricco, and E. Biglieri, “**Bit-interleaved coded modulation**,” *IEEE Transactions on Information Theory*, vol. 44, no. 3, pp. 927–946, May 1998.
- [67] Technical Specification Group Radio Access Network, “**E-UTRA; physical layer procedures**,” 3GPP, Tech. Rep. TS 36.211 Version 9.2.0, June 2010.
- [68] G. Caire, G. Taricco, and E. Biglieri, “**Capacity of bit-interleaved channels**,” *Electronics Letter*, vol. 32, no. 12, pp. 1060–1061, June 1996.
- [69] Rohde& Schwarz, **Cell search and cell selection in UMTS LTE**, ser. Application Note 1MA150.0E, Sept. 2009.
- [70] V. Le Nir, T. van Waterschoot, J. Duplicy, and M. Moonen, “**Blind coarse timing offset estimation for CP-OFDM and ZP-OFDM transmission over frequency selective channels**,” *EURASIP Journal on Wireless Communications and Networking*, vol. 2009, Article ID 262813, 2009.
- [71] Q. Wang, M. Šimko, and M. Rupp, “**Modified symbol timing offset estimation for OFDM over frequency selective channels**,” in *Proceeding of IEEE 74th Vehicular Technology Conference (VTC2011-Fall)*, San Francisco, USA, Sept. 2011.
- [72] M. Speth, F. Classen, and H. Meyr, “**Frame synchronization of OFDM systems in frequency selective fading channels**,” in *IEEE 47th Vehicular Technology Conference*, pp. 1807–1811, May 1997.
- [73] M. Šimko, C. Mehlführer, M. Wrulich, and M. Rupp, “**Doubly dispersive channel estimation with scalable complexity**,” in *Proceeding of International ITG Workshop on Smart Antennas (WSA 2010)*, Bremen, Germany, Feb. 2010.
- [74] M. Meidlinger and Q. Wang, “**Performance evaluation of LTE advanced downlink channel estimators**,” in *Proceeding of International Conference on Systems, Signals and Image Processing (IWSSIP 2012)*, Vienna, Austria, Apr. 2012.
- [75] Y. Mostofi, D. Cox, and A. Bahai, “**Effect of frame synchronization errors on pilot-aided channel estimation in OFDM: analysis and solution**,” in *The 5th International Symposium on Wireless Personal Multimedia Communications*, vol. 3, pp. 1309–1313, Oct. 2002.
- [76] J. Park, J. Kim, M. Park, K. Ko, C. Kang, and D. Hong, “**Performance analysis of channel estimation for OFDM systems with residual timing offset**,” *IEEE Transactions on Wireless Communications*, vol. 5, no. 7, pp. 1622–1625, July 2006.
- [77] C.-H. Lim and D. S. Han, “**Robust LS channel estimation with phase rotation for single**
-

-
- frequency network in OFDM,”** *IEEE Transactions on Consumer Electronics*, vol. 52, no. 4, pp. 1173–1178, Nov. 2006.
- [78] D.-C. Chang, “**Effect and compensation of symbol timing offset in OFDM systems with channel interpolation,**” *IEEE Transactions on Broadcasting*, vol. 54, no. 4, pp. 761–770, Dec. 2008.
- [79] V. Srivastava, C. K. Ho, P. H. W. Fung, and S. Sun, “**Robust MMSE channel estimation in OFDM systems with practical timing synchronization,**” in *IEEE Wireless Communications and Networking Conference, 2004. (WCNC. 2004)*, vol. 2, pp. 711 – 716 Vol.2, Mar. 2004, doi: 10.1109/WCNC.2004.1311273.
- [80] Q. Wang, D. Wu, J. Eilert, and D. Liu, “**Cost analysis of channel estimation in MIMO-OFDM for software defined radio,**” in *Proc. IEEE Wireless Communications & Networking Conference (WCNC 2008)*, Las Vegas, USA, Apr. 2008.
- [81] M. Šimko, S. Pendl, S. Schwarz, Q. Wang, J. C. Ikuno, and M. Rupp, “**Optimal pilot symbol power allocation in LTE,**” in *Proceeding of IEEE 74th Vehicular Technology Conference (VTC2011-Fall)*, San Francisco, USA, Sept. 2011.
- [82] R. Weber, “**Low-complexity channel estimation for WCDMA random access,**” in *IEEE 52nd Vehicular Technology Conference, 2000 (VTC-Fall 2000)*, vol. 1, pp. 344–351, 2000.
- [83] M. Jiang, S. Huang, and W. Wen, “**Adaptive polar-linear interpolation aided channel estimation for wireless communication systems,**” *IEEE Transactions on Wireless communications*, vol. 11, no. 3, pp. 920–926, Mar. 2012.
- [84] H. R. Tanhaei and S. A. Ghorashi, “**A novel channel estimation technique for OFDM systems with robustness against timing offset,**” *IEEE Transactions on Consumer Electronics*, vol. 57, no. 2, pp. 348–356, May 2011.
- [85] M.-H. Hsieh and C.-H. Wei, “**Channel estimation for OFDM systems based on comb-type pilot arrangement in frequency selective fading channels,**” *IEEE Transactions on Consumer Electronics*, vol. 44, no. 1, pp. 217–225, Feb. 1998.
- [86] Y. Li, J. Cimini, L.J., and N. Sollenberger, “**Robust channel estimation for OFDM systems with rapid dispersive fading channels,**” *IEEE Transactions on Communications*, vol. 46, no. 7, pp. 902–915, July 1998, doi: 10.1109/26.701317.
- [87] J. C. Ikuno, S. Pendl, M. Šimko, and M. Rupp, “**Accurate SINR estimation model for system level simulation of LTE networks,**” in *Proc. IEEE International Conference on Communications (ICC 2012)*, Ottawa, Canada, June 2012.
- [88] C. Wang, E. Au, R. Murch, W. H. Mow, R. Cheng, and V. Lau, “**On the performance of the MIMO zero-forcing receiver in the presence of channel estimation error,**” *IEEE Transactions on Wireless Communications*, vol. 6, no. 3, pp. 805–810, Mar. 2007, doi: 10.1109/TWC.2007.05384.

A. Differential RFO Estimation

A.1. Theoretical Mean Squared Error (MSE) - derivation of Equation (3.9)

A detailed performance analysis of the differential estimator for Residual Frequency Offset (RFO) estimation is presented in [45]. In this appendix, a brief summary is provided based on the signal model given in Chapter 2.

Following Equation (3.7), for medium and high Signal to Noise Ratio (SNR), the last term $\tilde{V}_{l,k}^{(m)} \tilde{V}_{l+d,k}^{(m)*} \cdot \left(X_{l,k}^{(q)} X_{l+d,k}^{(q)*} \right)^*$ will be negligible. Hence, the accumulated $W_{l,k}^{(m)}$ in Equation (3.8) can be approximated as a complex Gaussian random variable, expressed as

$$\sum_{m=1}^{N_R} \sum_{l=0}^{N_f-d-1} \sum_{k \in \mathcal{K}_p} W_{l,k}^{(m)} \sim \mathcal{N} \left(e^{-i\phi \cdot d} \sigma_s^4 \sigma_h^2 N_p (N_f - d) N_R, 2\sigma_s^6 \sigma_h^2 \sigma_v^2 N_p (N_f - d) N_R \right). \quad (\text{A.1})$$

Define

$$Y, X \sim \mathcal{N} \left(0, \sigma_s^6 \sigma_h^2 \sigma_v^2 N_p (N_f - d) N_R \right), \quad (\text{A.2})$$

assume $-\pi/2 < \phi d < \pi/2$, there is

$$\begin{aligned} \hat{\phi} &= -\frac{1}{d} \cdot \arctan \left\{ \frac{\Im \left\{ \sum_{m=1}^{N_R} \sum_{l=0}^{N_f-d} \sum_{k \in \mathcal{K}_p} W_{l,k}^{(m)} \right\}}{\Re \left\{ \sum_{m=1}^{N_R} \sum_{l=0}^{N_f-d} \sum_{k \in \mathcal{K}_p} W_{l,k}^{(m)} \right\}} \right\} \\ &= -\frac{1}{d} \cdot \arctan \left\{ \frac{\sigma_s^4 \sigma_h^2 N_p (N_f - d) N_R \cdot \sin(-\phi \cdot d) + Y}{\sigma_s^4 \sigma_h^2 N_p (N_f - d) N_R \cdot \cos(-\phi \cdot d) + X} \right\}. \end{aligned} \quad (\text{A.3})$$

Using a first-order Taylor expansion around $(x, y) = (x_0, y_0)$,

$$\begin{aligned} f(x, y) &\approx f(x_0, y_0) + (x - x_0) \left. \frac{\partial f(x, y)}{\partial x} \right|_{(x,y)=(x_0,y_0)} \\ &\quad + (y - y_0) \left. \frac{\partial f(x, y)}{\partial y} \right|_{(x,y)=(x_0,y_0)}, \end{aligned} \quad (\text{A.4})$$

the arctan function can be approximated as [45]

$$\begin{aligned} \arctan \left\{ \frac{y_0 + \Delta y}{x_0 + \Delta x} \right\} &\approx \arctan \left\{ \frac{y_0}{x_0} \right\} - \Delta x \frac{y_0}{y_0^2 + x_0^2} + \Delta y \frac{x_0}{y_0^2 + x_0^2} \\ &= \arctan \left\{ \frac{y_0}{x_0} \right\} + \frac{x_0 \Delta y - y_0 \Delta x}{y_0^2 + x_0^2}. \end{aligned} \quad (\text{A.5})$$

Therefore, Equation (A.3) leads to

$$\begin{aligned} \hat{\phi} &\approx -\frac{1}{d} \cdot \arctan \left\{ \frac{\sigma_s^4 \sigma_h^2 N_p (N_f - d) N_R \sin(-\phi \cdot d)}{\sigma_s^4 \sigma_h^2 N_p (N_f - d) N_R \cos(-\phi \cdot d)} \right\} - \\ &\quad - \frac{1}{d} \cdot \frac{\sigma_s^4 \sigma_h^2 N_p (N_f - d) N_R [Y \cos(-\phi \cdot d) - X \sin(-\phi \cdot d)]}{\sigma_s^8 \sigma_h^4 N_p^2 (N_f - d)^2 N_R^2 [\sin^2(-\phi \cdot d) + \cos^2(-\phi \cdot d)]} \\ &= \phi - \frac{1}{d} \cdot \frac{Y \cos(-\phi \cdot d) - X \sin(-\phi \cdot d)}{\sigma_s^4 \sigma_h^2 N_p (N_f - d) N_R}. \end{aligned} \quad (\text{A.6})$$

Using Equation (A.2), the distribution of the phase-shift estimation is then approximately

$$\begin{aligned} \hat{\phi} &\sim \mathcal{N} \left(\phi, \frac{\sigma_s^6 \sigma_h^2 \sigma_v^2 N_p (N_f - d) N_R}{\sigma_s^8 \sigma_h^4 N_p^2 (N_f - d)^2 N_R^2 d^2} \right) \\ &\sim \mathcal{N} \left(\phi, \frac{\sigma_v^2}{\sigma_s^2 \sigma_h^2 N_p (N_f - d) N_R d^2} \right). \end{aligned} \quad (\text{A.7})$$

Knowing that

$$\phi = \frac{2\pi \varepsilon_{\text{RFO}} (N + N_g)}{N}, \quad (\text{A.8})$$

we obtain

$$\begin{aligned} \mathbb{E}\{|\hat{\varepsilon}_{\text{RFO}} - \varepsilon_{\text{RFO}}|^2\} &= \frac{N^2}{4\pi^2 (N + N_g)^2} \cdot \mathbb{E}\{|\hat{\phi} - \phi|^2\} \\ &= \frac{N^2}{4\pi^2 (N + N_g)^2} \cdot \frac{\sigma_v^2}{\sigma_s^2 \sigma_h^2 N_p (N_f - d) N_R d^2} \\ &= \frac{N^2}{4\pi^2 (N + N_g)^2 N_p (N_f - d) N_R d^2 \cdot \text{SNR}} \quad | \quad \text{SNR} = \frac{\sigma_s^2 \sigma_h^2}{\sigma_v^2}, \end{aligned} \quad (\text{A.9})$$

which is the MSE of the differential estimator. Given the system parameters, a minimum MSE can be found by maximizing $(N_f - d)d^2$, where N_f is the number of Orthogonal Frequency Division Multiplexing (OFDM) symbols in the payload part of one frame. The estimation range of a differential estimator is constrained by the $\arg\{\cdot\}$ operation, namely

$$-\frac{\pi}{d} < \hat{\phi} < \frac{\pi}{d}. \quad (\text{A.10})$$

B. CRLB of the RFO Estimator using Pilot Subcarriers

This appendix provides a derivation of the Cramér-Rao Lower Bound (CRLB) of a pilot-subcarrier-based Residual Frequency Offset (RFO) estimator which applies to the Worldwide Inter-operability for Microwave Access (WiMAX) case.

We denote the number of pilot subcarriers by N_p , the number of Orthogonal Frequency Division Multiplexing (OFDM) symbols in one frame by N_f , and a normalized RFO by ε . In order to simplify the notation, we define $\phi = \frac{2\pi\varepsilon(N+N_g)}{N}$. Therefore, on the pilot subcarriers in the OFDM symbol l , the system model is expressed as

$$\mathbf{r}_l = e^{i\phi l} \cdot \underbrace{\mathbf{X}_l}_{N_p \times N_p} \underbrace{\mathbf{h}_l}_{N_p \times 1} + \mathbf{v}_l, \quad \mathbf{h}_l = \mathbf{h} \text{ for } l = 0, 1, \dots, N_f - 1, \quad (\text{B.1})$$

where \mathbf{r}_l is the received pilot symbols, \mathbf{h}_l the channel transfer function and \mathbf{v}_l the complex-valued additive Gaussian noise. The diagonal matrix \mathbf{X}_l contains the transmitted pilot symbols on its diagonal. Thus, the indexed log-likelihood function as a function of ϕ given the received pilot symbols can be written as

$$\begin{aligned} \Lambda(\phi) &= \ln f(\mathbf{r}_0, \mathbf{r}_1, \dots, \mathbf{r}_{N_f-1}; \phi) \\ &= \ln \frac{1}{\pi^{N_p N_f} \det(\mathbf{R})} \exp \left\{ - \underbrace{\begin{bmatrix} \mathbf{r}_0^H & \mathbf{r}_1^H & \dots & \mathbf{r}_{N_f-1}^H \end{bmatrix}}_{\mathbf{r}^H: 1 \times N_f N_p} \mathbf{R}^{-1} \underbrace{\begin{bmatrix} \mathbf{r}_0 \\ \mathbf{r}_1 \\ \vdots \\ \mathbf{r}_{N_f-1} \end{bmatrix}}_{\mathbf{r}} \right\}, \quad (\text{B.2}) \end{aligned}$$

where the correlation matrix

$$\begin{aligned} \mathbf{R} &= \mathbb{E}\{\underline{\mathbf{r}}\underline{\mathbf{r}}^H\} = \mathbb{E}\left\{ \begin{bmatrix} \underline{\mathbf{r}}_0 \\ \underline{\mathbf{r}}_1 \\ \vdots \\ \underline{\mathbf{r}}_{N_f-1} \end{bmatrix} \begin{bmatrix} \underline{\mathbf{r}}_0^H & \underline{\mathbf{r}}_1^H & \cdots & \underline{\mathbf{r}}_{N_f-1}^H \end{bmatrix} \right\} \\ &= \mathbb{E}\left\{ \begin{bmatrix} \underline{\mathbf{r}}_0\underline{\mathbf{r}}_0^H & \underline{\mathbf{r}}_0\underline{\mathbf{r}}_1^H & \cdots & \underline{\mathbf{r}}_0\underline{\mathbf{r}}_{N_f-1}^H \\ \underline{\mathbf{r}}_1\underline{\mathbf{r}}_0^H & \underline{\mathbf{r}}_1\underline{\mathbf{r}}_1^H & \ddots & \vdots \\ \vdots & \ddots & \ddots & \vdots \\ \underline{\mathbf{r}}_{N_f-1}\underline{\mathbf{r}}_0^H & \cdots & \cdots & \underline{\mathbf{r}}_{N_f-1}\underline{\mathbf{r}}_{N_f-1}^H \end{bmatrix} \right\}. \end{aligned} \quad (\text{B.3})$$

Knowing that

$$\begin{aligned} \mathbb{E}\{\underline{\mathbf{r}}_m\underline{\mathbf{r}}_n^H\} &= \mathbb{E}\left\{ \left[e^{i\phi m} \cdot \mathbf{X}_m \underline{\mathbf{h}} + \underline{\mathbf{v}}_m \right] \left[e^{i\phi n} \cdot \mathbf{X}_n \underline{\mathbf{h}} + \underline{\mathbf{v}}_n \right]^H \right\} \\ &= e^{i\phi(m-n)} \mathbf{X}_m \mathbb{E}\{\underline{\mathbf{h}}\underline{\mathbf{h}}^H\} \mathbf{X}_n^H + \mathbb{E}\{\underline{\mathbf{v}}_m \underline{\mathbf{v}}_n^H\} \end{aligned} \quad (\text{B.4})$$

$$= \begin{cases} e^{i\phi(m-n)} \mathbf{X}_m \mathbf{R}_{\mathbf{pp}} \mathbf{X}_n^H & \text{for } m \neq n \\ \mathbf{X}_m \mathbf{R}_{\mathbf{pp}} \mathbf{X}_m^H + \sigma_v^2 \mathbf{I} & \text{for } m = n, \end{cases} \quad (\text{B.5})$$

where $\mathbf{R}_{\mathbf{pp}} \in \mathbb{C}^{N_p \times N_p}$ denotes the channel autocorrelation matrix based on the pilot subcarriers, plugging Equation (B.4) into Equation (B.3) and assume $\mathbf{X}\mathbf{X}^H = \mathbf{I}$, after some arithmetic manipulations, we arrive at

$$\mathbf{R} = \mathbf{X} (\underline{\mathbf{a}}\underline{\mathbf{a}}^H \otimes \mathbf{R}_{\mathbf{pp}} + \sigma_v^2 \mathbf{I}) \mathbf{X}^H, \quad (\text{B.6})$$

with

$$\mathbf{X} = \text{diag}\{\mathbf{X}_0, \mathbf{X}_1, \dots, \mathbf{X}_{N_f-1}\}, \quad (\text{B.7})$$

$$\underline{\mathbf{a}} = \begin{bmatrix} 1 & e^{i\phi \cdot 1} & \cdots & e^{i\phi \cdot (N_f-1)} \end{bmatrix}^T. \quad (\text{B.8})$$

Firstly, we calculate $\det(\mathbf{R})$ in Equation (B.2). Given Equation (B.6) and $\mathbf{X}\mathbf{X}^H = \mathbf{I}$, there is $\det(\mathbf{R}) = \det\{(\underline{\mathbf{a}}\underline{\mathbf{a}}^H \otimes \mathbf{R}_{\mathbf{pp}}) + \sigma_v^2 \mathbf{I}\}$. The eigenvalues of $\underline{\mathbf{a}}\underline{\mathbf{a}}^H \otimes \mathbf{R}_{\mathbf{pp}}$ are defined by the product pairs of the eigenvalues of $\underline{\mathbf{a}}\underline{\mathbf{a}}^H$ and $\mathbf{R}_{\mathbf{pp}}$. The eigenvalues of the rank-1 matrix $\underline{\mathbf{a}}\underline{\mathbf{a}}^H$ are $N_f = \underline{\mathbf{a}}^H \underline{\mathbf{a}}$ and $N_f - 1$ times zero. Thus, the eigenvalues of $\underline{\mathbf{a}}\underline{\mathbf{a}}^H \otimes \mathbf{R}_{\mathbf{pp}}$ are N_p times the eigenvalues of $\mathbf{R}_{\mathbf{pp}}$ scaled by N_f and zero otherwise. They are all shifted by the term $\sigma_v^2 \mathbf{I}$. The determinant is thus $\prod[(N_f \cdot \text{eig}\{\mathbf{R}_{\mathbf{pp}}\} + \sigma_v^2)]$. Therefore, the scaling factor $\frac{1}{\pi^{N_p N_f} \det(\mathbf{R})}$ in $\Lambda(\phi)$ is independent of ϕ .

Secondly, the quadratic expression in the exponential term can be rewritten as

$$\begin{aligned} -\underline{\mathbf{r}}^H \mathbf{R}^{-1} \underline{\mathbf{r}} &= -\underline{\mathbf{r}}^H (\mathbf{X} (\underline{\mathbf{a}} \underline{\mathbf{a}}^H \otimes \mathbf{R}_{\text{pp}} + \sigma_v^2 \mathbf{I}) \mathbf{X}^H)^{-1} \underline{\mathbf{r}} \\ &= -\underline{\mathbf{r}}^H \mathbf{X} (\underline{\mathbf{a}} \underline{\mathbf{a}}^H \otimes \mathbf{R}_{\text{pp}} + \sigma_v^2 \mathbf{I})^{-1} \mathbf{X}^H \underline{\mathbf{r}}, \end{aligned} \quad (\text{B.9})$$

where the matrix inversion part can be reformulated as

$$(\underline{\mathbf{a}} \underline{\mathbf{a}}^H \otimes \mathbf{R}_{\text{pp}} + \sigma_v^2 \mathbf{I})^{-1} = ((\underline{\mathbf{a}} \otimes \mathbf{I})(1 \otimes \mathbf{R}_{\text{pp}})(\underline{\mathbf{a}}^H \otimes \mathbf{I}) + \sigma_v^2 \mathbf{I})^{-1}. \quad (\text{B.10})$$

Apply the matrix inversion lemma

$$(\mathbf{W} + \mathbf{U} \mathbf{S} \mathbf{V})^{-1} = \mathbf{W}^{-1} - \mathbf{W}^{-1} \mathbf{U} (\mathbf{S}^{-1} + \mathbf{V} \mathbf{W}^{-1} \mathbf{U})^{-1} \mathbf{V} \mathbf{W}^{-1}, \quad (\text{B.11})$$

we obtain

$$\begin{aligned} & ((\underline{\mathbf{a}} \otimes \mathbf{I})(1 \otimes \mathbf{R}_{\text{pp}})(\underline{\mathbf{a}}^H \otimes \mathbf{I}) + \sigma_v^2 \mathbf{I})^{-1} \\ &= \frac{1}{\sigma_v^2} \cdot \mathbf{I} - \frac{1}{\sigma_v^2} \cdot (\underline{\mathbf{a}} \otimes \mathbf{I}) \left[(1 \otimes \mathbf{R}_{\text{pp}})^{-1} + \frac{1}{\sigma_v^2} (\underline{\mathbf{a}}^H \otimes \mathbf{I})(\underline{\mathbf{a}} \otimes \mathbf{I}) \right]^{-1} (\underline{\mathbf{a}}^H \otimes \mathbf{I}) \frac{1}{\sigma_v^2} \\ &= \frac{1}{\sigma_v^2} \cdot \mathbf{I} - \frac{1}{\sigma_v^4} \cdot (\underline{\mathbf{a}} \otimes \mathbf{I}) \underbrace{\left[\mathbf{R}_{\text{pp}}^{-1} + \frac{N_f}{\sigma_v^2} \cdot \mathbf{I} \right]^{-1}}_{\mathbf{B}} (\underline{\mathbf{a}}^H \otimes \mathbf{I}) \\ &= \frac{1}{\sigma_v^2} \cdot \mathbf{I} - \frac{1}{\sigma_v^4} \cdot (\underline{\mathbf{a}} \otimes \mathbf{I})(1 \otimes \mathbf{B})(\underline{\mathbf{a}}^H \otimes \mathbf{I}) \\ &= \frac{1}{\sigma_v^2} \cdot \mathbf{I} - \frac{1}{\sigma_v^4} \cdot \underbrace{(\underline{\mathbf{a}} \underline{\mathbf{a}}^H \otimes \mathbf{B})}_{\mathbf{A}(\phi)}. \end{aligned} \quad (\text{B.12})$$

Thus, Equation (B.9) becomes

$$\begin{aligned} -\underline{\mathbf{r}}^H \mathbf{R}^{-1} \underline{\mathbf{r}} &= -\underline{\mathbf{r}}^H \mathbf{X} \left[\frac{1}{\sigma_v^2} \cdot \mathbf{I} - \frac{1}{\sigma_v^4} \cdot (\mathbf{A}(\phi) \otimes \mathbf{B}) \right] \mathbf{X}^H \underline{\mathbf{r}} \\ &= -\frac{\underline{\mathbf{r}}^H \underline{\mathbf{r}}}{\sigma_v^2} + \frac{1}{\sigma_v^4} \underline{\mathbf{r}}^H \mathbf{X} (\mathbf{A}(\phi) \otimes \mathbf{B}) \mathbf{X}^H \underline{\mathbf{r}}. \end{aligned} \quad (\text{B.13})$$

Specifically,

$$\mathbf{A}(\phi) = \begin{bmatrix} 1 & e^{i\phi \cdot (-1)} & \dots & e^{i\phi \cdot (-(N_f-1))} \\ e^{i\phi \cdot (1)} & 1 & \ddots & \vdots \\ \vdots & \ddots & \ddots & \vdots \\ e^{i\phi \cdot (N_f-1)} & \dots & \dots & 1 \end{bmatrix} \quad (\text{B.14})$$

To calculate the Fisher information

$$J(\phi) = -\mathbb{E}\left\{\frac{\partial^2}{\partial\phi^2}\Lambda(\phi)\right\}, \quad (\text{B.15})$$

the second derivative of the log-likelihood function can be calculated as

$$\frac{\partial^2}{\partial\phi^2}\Lambda(\phi) = \frac{\partial^2}{\partial\phi^2}\{-\underline{\mathbf{r}}^H\mathbf{R}^{-1}\underline{\mathbf{r}}\} = \frac{1}{\sigma_v^4}\underline{\mathbf{r}}^H\mathbf{X}\left(\frac{\partial^2}{\partial\phi^2}\mathbf{A}(\phi)\otimes\mathbf{B}\right)\mathbf{X}^H\underline{\mathbf{r}}, \quad (\text{B.16})$$

where

$$\begin{aligned} \frac{\partial^2}{\partial\phi^2}\mathbf{A}(\phi) &= \begin{bmatrix} 0 & (-1i)^2e^{i\phi(-1)} & \dots & -(N_f-1)i^2e^{i\phi(-(N_f-1))} \\ (1i)^2e^{i\phi(1)} & 0 & \ddots & \vdots \\ \vdots & \ddots & \ddots & \vdots \\ ((N_f-1)i)^2e^{i\phi(N_f-1)} & \dots & \dots & 0 \end{bmatrix} \\ &= \text{diag}\{\underline{\mathbf{a}}\} \cdot \mathbf{C} \cdot \text{diag}\{\underline{\mathbf{a}}\}^H = \mathbf{DCD}^H, \end{aligned} \quad (\text{B.17})$$

with

$$\begin{aligned} \mathbf{C} &= \begin{bmatrix} 0 & (-1i)^2 & \dots & -(N_f-1)i^2 \\ (1i)^2 & 0 & \ddots & \vdots \\ \vdots & \ddots & \ddots & \vdots \\ ((N_f-1)i)^2 & \dots & \dots & 0 \end{bmatrix} \\ &= \begin{bmatrix} 0 & -1^2 & \dots & -(N_f-1)^2 \\ -1^2 & 0 & \ddots & \vdots \\ \vdots & \ddots & \ddots & -1^2 \\ -(N_f-1)^2 & \dots & -1^2 & 0 \end{bmatrix}. \end{aligned} \quad (\text{B.18})$$

Thus,

$$\begin{aligned} J(\phi) &= -\mathbb{E}\left\{\frac{\partial^2}{\partial\phi^2}\Lambda(\phi)\right\} = -\mathbb{E}\left\{\frac{1}{\sigma_v^4}\underline{\mathbf{r}}^H\mathbf{X}(\mathbf{DCD}^H\otimes\mathbf{B})\mathbf{X}^H\underline{\mathbf{r}}\right\} \\ &= -\frac{1}{\sigma_v^4}\mathbb{E}\{\underline{\mathbf{r}}^H\mathbf{X}(\mathbf{D}\otimes\mathbf{I})(\mathbf{C}\otimes\mathbf{B})(\mathbf{D}^H\otimes\mathbf{I})\mathbf{X}^H\underline{\mathbf{r}}\}. \end{aligned} \quad (\text{B.19})$$

Given Equation (B.1) and Equation (B.2), the received pilot symbol vector can be rewritten as $\underline{\mathbf{r}} = \mathbf{X}(\mathbf{D}\otimes\mathbf{I})(\mathbf{1}\otimes\underline{\mathbf{h}}) + \underline{\mathbf{v}}$, where $\mathbf{1}$ is an all-one vector of size $N_f \times 1$.

Continue with Equation (B.19), there is

$$\begin{aligned}
 J(\phi) &= -\frac{1}{\sigma_v^4} \mathbb{E}\{(\mathbf{1}^H \otimes \mathbf{h}^H)(\mathbf{D}^H \otimes \mathbf{I})\mathbf{X}^H\mathbf{X}(\mathbf{D} \otimes \mathbf{I})(\mathbf{C} \otimes \mathbf{B})(\mathbf{D}^H \otimes \mathbf{I})\mathbf{X}^H\mathbf{X}(\mathbf{D} \otimes \mathbf{I})(\mathbf{1} \otimes \mathbf{h})\} \\
 &\quad - \frac{1}{\sigma_v^4} \mathbb{E}\{\mathbf{v}^H\mathbf{X}(\mathbf{D} \otimes \mathbf{I})(\mathbf{C} \otimes \mathbf{B})(\mathbf{D}^H \otimes \mathbf{I})\mathbf{X}^H\mathbf{v}\} \\
 &= -\frac{1}{\sigma_v^4} \mathbb{E}\{(\mathbf{1}^H \otimes \mathbf{h}^H)(\mathbf{C} \otimes \mathbf{B})(\mathbf{1} \otimes \mathbf{h})\} - \frac{1}{\sigma_v^4} \text{tr}\{(\mathbf{D}\mathbf{C}\mathbf{D}^H \otimes \mathbf{B}) \mathbb{E}\{\mathbf{X}^H\mathbf{v}\mathbf{v}^H\mathbf{X}\}\} \\
 &= -\frac{1}{\sigma_v^4} \mathbb{E}\{(\mathbf{1}^H\mathbf{C}\mathbf{1} \otimes \mathbf{h}^H\mathbf{B}\mathbf{h})\} - \frac{1}{\sigma_v^2} \text{tr}\{\mathbf{D}\mathbf{C}\mathbf{D}^H\} \text{tr}\{\mathbf{B}\} \\
 &= -\frac{1}{\sigma_v^4} \cdot \mathbf{1}^H\mathbf{C}\mathbf{1} \cdot \mathbb{E}\{\mathbf{h}^H\mathbf{B}\mathbf{h}\} - \frac{1}{\sigma_v^2} \underbrace{\text{tr}\{\mathbf{C}\}}_{=0} \text{tr}\{\mathbf{B}\}. \tag{B.20}
 \end{aligned}$$

The expectation term can be further manipulated as

$$\begin{aligned}
 \mathbb{E}\{\mathbf{h}^H\mathbf{B}\mathbf{h}\} &= \mathbb{E}\{\text{tr}\{\mathbf{B}\mathbf{h}\mathbf{h}^H\}\} = \text{tr}\{\mathbf{B} \cdot \mathbb{E}\{\mathbf{h}\mathbf{h}^H\}\} = \text{tr}\{\mathbf{B}\mathbf{R}_{\mathbf{pp}}\} \\
 &= \text{tr}\left\{\left[\mathbf{R}_{\mathbf{pp}}^{-1} + \frac{N_f}{\sigma_v^2} \cdot \mathbf{I}\right]^{-1} \mathbf{R}_{\mathbf{pp}}\right\} = \sum \text{eig}\left\{\left[\mathbf{R}_{\mathbf{pp}}^{-1} + \frac{N_f}{\sigma_v^2} \cdot \mathbf{I}\right]^{-1} \mathbf{R}_{\mathbf{pp}}\right\} \\
 &= \sum_{i=1}^{N_p} \frac{\lambda_i}{\frac{1}{\lambda_i} + \frac{N_f}{\sigma_v^2}} \quad \text{for } \lambda_i \neq 0, \tag{B.21}
 \end{aligned}$$

where $\lambda_i; i = 1, \dots, N_p$ denotes the eigenvalues of $\mathbf{R}_{\mathbf{pp}}$. To summarize, using the Fisher information

$$\begin{aligned}
 J(\phi) &= -\frac{1}{\sigma_v^4} \cdot \mathbf{1}^H\mathbf{C}\mathbf{1} \cdot \sum_{i=1}^{N_p} \frac{\lambda_i}{\frac{1}{\lambda_i} + \frac{N_f}{\sigma_v^2}} = -\mathbf{1}^H\mathbf{C}\mathbf{1} \cdot \sum_{i=1}^{N_p} \frac{\lambda_i^2}{\sigma_v^4 + N_f\sigma_v^2\lambda_i} \\
 &\approx -\mathbf{1}^H\mathbf{C}\mathbf{1} \cdot \sum_{i=1}^{N_p} \frac{\lambda_i}{N_f\sigma_v^2} \quad \text{for large SNRs.} \tag{B.22}
 \end{aligned}$$

Using the Faulhaber's formular

$$\sum_{k=1}^p k = \frac{p(p+1)}{2}, \tag{B.23}$$

$$\sum_{k=1}^p k^2 = \frac{p(p+1)(2p+1)}{6} = \frac{p^3}{3} + \frac{p^2}{2} + \frac{p}{6}, \tag{B.24}$$

$$\sum_{k=1}^p k^3 = \left[\frac{p(p+1)}{2}\right]^2 = \frac{p^4}{4} + \frac{p^3}{2} + \frac{p^2}{4}, \tag{B.25}$$

the sum of elements in the matrix \mathbf{C} can be calculated as

$$\begin{aligned}
-\underline{\mathbf{1}}^H \mathbf{C} \underline{\mathbf{1}} &= 2 \cdot \sum_{m=1}^{N_f-1} \sum_{n=1}^m n^2 = 2 \cdot \sum_{m=1}^{N_f-1} \frac{m^3}{3} + \frac{m^2}{2} + \frac{m}{6} \\
&= 2 \left[\frac{1}{3} \sum_{m=1}^{N_f-1} m^3 + \frac{1}{2} \sum_{m=1}^{N_f-1} m^2 + \frac{1}{6} \sum_{m=1}^{N_f-1} m \right] \\
&= \frac{2}{3} \left[\frac{(N_f-1)^4}{4} + \frac{(N_f-1)^3}{2} + \frac{(N_f-1)^2}{4} \right] + \left[\frac{(N_f-1)^3}{3} + \right. \\
&\quad \left. + \frac{(N_f-1)^2}{2} + \frac{(N_f-1)}{6} \right] + \frac{1}{3} \left[\frac{(N_f-1)^2}{2} + \frac{(N_f-1)}{2} \right] \\
&= \frac{1}{6}(N_f-1)^4 + \frac{2}{3}(N_f-1)^3 + \frac{5}{6}(N_f-1)^2 + \frac{1}{3}(N_f-1). \tag{B.26}
\end{aligned}$$

Thus, the CRLB is obtained by

$$\text{MSE}_{\hat{\varepsilon}} = \frac{N^2}{4\pi^2(N+N_g)^2} \cdot \text{MSE}_{\hat{\phi}} \geq \frac{N^2}{4\pi^2(N+N_g)^2} \cdot \frac{1}{J(\phi)}. \tag{B.27}$$

C. Maximum Likelihood Estimator

C.1. Fractional Frequency Offset (FFO) - derivation of Equation (4.1)

This section provides a derivation of the Maximum Likelihood (ML) estimator of the Fractional Frequency Offset (FFO) in Section 4.2. We consider a simplified system model of single-input single-output in a vector form:

$$\mathbf{r}_{\text{CP}} = \mathbf{z} + \mathbf{v}_{\text{CP}} \in \mathbb{C}^{N_g \times 1} \quad (\text{C.1})$$

$$\mathbf{r} = \mathbf{z} \cdot e^{i\frac{2\pi\varepsilon N}{N}} + \mathbf{v} = \mathbf{z} \cdot e^{i2\pi\varepsilon} + \mathbf{v} \in \mathbb{C}^{N_g \times 1} \quad (\text{C.2})$$

This model describes the behavior of the two duplicated parts in one Orthogonal Frequency Division Multiplexing (OFDM) symbol due to the insertion of the Cyclic Prefix (CP). The vector \mathbf{z} is the received signal which is not disturbed by the additive noise. The vectors \mathbf{r}_{CP} and \mathbf{r} are the received signals from the beginning(CP) and the tail of an OFDM symbol. The complex-valued additive white Gaussian noise is denoted by \mathbf{v} , $\mathbf{v}_{\text{CP}} \sim \mathcal{CN}(0, \sigma_v^2 \mathbf{I})$.

In order to derive an ML estimator for ε based on the observation vector \mathbf{r}_{CP} and \mathbf{r} , we write the indexed log-likelihood function as a function of ε as

$$\begin{aligned} \Lambda(\varepsilon) &= \ln f(\mathbf{r}_{\text{CP}}, \mathbf{r}; \varepsilon) \\ &= \ln \frac{1}{\pi^{2N_g} \det(\mathbf{R})} \exp \left\{ - \begin{bmatrix} \mathbf{r}_{\text{CP}}^{\text{H}} & \mathbf{r}^{\text{H}} \end{bmatrix} \mathbf{R}^{-1} \begin{bmatrix} \mathbf{r}_{\text{CP}} \\ \mathbf{r} \end{bmatrix} \right\}, \end{aligned} \quad (\text{C.3})$$

where the covariance matrix

$$\begin{aligned} \mathbf{R} &= \mathbb{E} \left\{ \begin{bmatrix} \mathbf{r}_{\text{CP}} \mathbf{r}_{\text{CP}}^{\text{H}} & \mathbf{r}_{\text{CP}} \mathbf{r}^{\text{H}} \\ \mathbf{r} \mathbf{r}_{\text{CP}}^{\text{H}} & \mathbf{r} \mathbf{r}^{\text{H}} \end{bmatrix} \right\} = \begin{bmatrix} \mathbb{E}\{\mathbf{r}_{\text{CP}} \mathbf{r}_{\text{CP}}^{\text{H}}\} & \mathbb{E}\{\mathbf{r}_{\text{CP}} \mathbf{r}^{\text{H}}\} \\ \mathbb{E}\{\mathbf{r} \mathbf{r}_{\text{CP}}^{\text{H}}\} & \mathbb{E}\{\mathbf{r} \mathbf{r}^{\text{H}}\} \end{bmatrix} \\ &= \begin{bmatrix} (\sigma_z^2 + \sigma_v^2) \mathbf{I} & \sigma_z^2 e^{-i2\pi\varepsilon} \mathbf{I} \\ \sigma_z^2 e^{i2\pi\varepsilon} \mathbf{I} & (\sigma_z^2 + \sigma_v^2) \mathbf{I} \end{bmatrix} = \begin{bmatrix} \sigma_z^2 + \sigma_v^2 & \sigma_z^2 e^{-i2\pi\varepsilon} \\ \sigma_z^2 e^{i2\pi\varepsilon} & \sigma_z^2 + \sigma_v^2 \end{bmatrix} \otimes \mathbf{I}. \end{aligned} \quad (\text{C.4})$$

Here, the average power of the undisturbed received signal is denoted by σ_z^2 and the average noise power by σ_v^2 . Using the properties of the Kronecker product, we

obtain

$$\det(\mathbf{R}) = \begin{vmatrix} \sigma_z^2 + \sigma_v^2 & \sigma_z^2 e^{-i2\pi\varepsilon} \\ \sigma_z^2 e^{i2\pi\varepsilon} & \sigma_z^2 + \sigma_v^2 \end{vmatrix}^{N_g} \cdot (1)^2 = (2\sigma_z^2\sigma_v^2 + \sigma_v^4)^{N_g} \quad (\text{C.5})$$

$$\begin{aligned} \mathbf{R}^{-1} &= \begin{bmatrix} \sigma_z^2 + \sigma_v^2 & \sigma_z^2 e^{-i2\pi\varepsilon} \\ \sigma_z^2 e^{i2\pi\varepsilon} & \sigma_z^2 + \sigma_v^2 \end{bmatrix}^{-1} \otimes \mathbf{I}^{-1} \\ &= \frac{1}{2\sigma_z^2\sigma_v^2 + \sigma_v^4} \begin{bmatrix} \sigma_z^2 + \sigma_v^2 & -\sigma_z^2 e^{-i2\pi\varepsilon} \\ -\sigma_z^2 e^{i2\pi\varepsilon} & \sigma_z^2 + \sigma_v^2 \end{bmatrix} \otimes \mathbf{I} \end{aligned} \quad (\text{C.6})$$

Plug into Equation (C.3), the ML estimation of ε is obtained by

$$\begin{aligned} \hat{\varepsilon}_{\text{FFO,ML}} &= \arg \max_{\varepsilon} \Lambda(\varepsilon) = \arg \max_{\varepsilon} \left\{ - \begin{bmatrix} \mathbf{r}_{\text{CP}}^H & \mathbf{r}^H \end{bmatrix} \mathbf{R}^{-1} \begin{bmatrix} \mathbf{r}_{\text{CP}} \\ \mathbf{r} \end{bmatrix} \right\} \\ &= \arg \max_{\varepsilon} \left\{ \sigma_z^2 e^{i2\pi\varepsilon} \mathbf{r}^H \mathbf{r}_{\text{CP}} + \sigma_z^2 e^{-i2\pi\varepsilon} \mathbf{r}_{\text{CP}}^H \mathbf{r} - (\sigma_z^2 + \sigma_v^2) (\|\mathbf{r}_{\text{CP}}\|_2^2 + \|\mathbf{r}\|_2^2) \right\} \\ &= \arg \max_{\varepsilon} \left\{ e^{i2\pi\varepsilon} \mathbf{r}^H \mathbf{r}_{\text{CP}} + e^{-i2\pi\varepsilon} \mathbf{r}_{\text{CP}}^H \mathbf{r} \right\} \\ &= \arg \max_{\varepsilon} \left\{ \Re \{ e^{i2\pi\varepsilon} \mathbf{r}^H \mathbf{r}_{\text{CP}} \} \right\} \\ &= -\frac{1}{2\pi} \arg \{ \mathbf{r}^H \mathbf{r}_{\text{CP}} \} \end{aligned} \quad (\text{C.7})$$

Therefore, we arrive at the solution as shown in Equation (4.1).

C.2. Integer Frequency Offset (IFO) - derivation of Equation (4.4)

This section provides a derivation of the Maximum Likelihood (ML) estimator of the Integer Frequency Offset (IFO) in Equation (4.4). We define the following expressions in a vector form:

$$\mathbf{x}_S(\varepsilon) = [X_{\text{SSS},0-\varepsilon}, \dots, X_{\text{SSS},k-\varepsilon}, \dots, X_{\text{SSS},N_{\text{sync}}-\varepsilon}]^T \in \mathbb{C}^{N_{\text{sync}} \times 1} \quad (\text{C.8})$$

$$\mathbf{x}_P(\varepsilon) = [X_{\text{PSS},0-\varepsilon}, \dots, X_{\text{PSS},k-\varepsilon}, \dots, X_{\text{PSS},N_{\text{sync}}-\varepsilon}]^T \in \mathbb{C}^{N_{\text{sync}} \times 1} \quad (\text{C.9})$$

$$\mathbf{H}(\varepsilon) = \text{diag} \{ H_{0-\varepsilon}, \dots, H_{k-\varepsilon}, \dots, H_{N_{\text{sync}}-\varepsilon} \} \in \mathbb{C}^{N_{\text{sync}} \times N_{\text{sync}}} \quad (\text{C.10})$$

$$\mathbf{r}_S = [R_{\text{SSS},0}, \dots, R_{\text{SSS},k}, \dots, R_{\text{SSS},N_{\text{sync}}}]^T \in \mathbb{C}^{N_{\text{sync}} \times 1} \quad (\text{C.11})$$

$$\mathbf{r}_P = [R_{\text{PSS},0}, \dots, R_{\text{PSS},k}, \dots, R_{\text{PSS},N_{\text{sync}}}]^T \in \mathbb{C}^{N_{\text{sync}} \times 1} \quad (\text{C.12})$$

Here, N_{sync} is the number of subcarriers occupied by the synchronization signals. Assume an integer-valued Carrier Frequency Offset (CFO) ε , a simplified system model of single-input single-output can be defined as

$$\mathbf{r}_S = e^{i \frac{2\pi\varepsilon l(N+N_g)}{N}} \cdot \mathbf{H}(\varepsilon) \mathbf{x}_S(\varepsilon) + \mathbf{v}_S, \quad (\text{C.13})$$

$$\mathbf{r}_P = e^{i \frac{2\pi\varepsilon(l+1)(N+N_g)}{N}} \cdot \mathbf{H}(\varepsilon) \mathbf{x}_P(\varepsilon) + \mathbf{v}_P, \quad (\text{C.14})$$

where the vectors \mathbf{v}_S and \mathbf{v}_P are the corresponding noise vectors. Here, the normalized CFO ε is considered as an integer. Based on the observation of received vectors \mathbf{r}_S and \mathbf{r}_P , the log-likelihood function for ε can be written as

$$\begin{aligned} \Lambda(\varepsilon) &= \ln f(\mathbf{r}_S, \mathbf{r}_P; \varepsilon) \\ &= \ln \frac{1}{\pi^{2N_{\text{sync}}} \det(\mathbf{R})} \exp \left\{ - \begin{bmatrix} \mathbf{r}_S^H & \mathbf{r}_P^H \end{bmatrix} \mathbf{R}^{-1} \begin{bmatrix} \mathbf{r}_S \\ \mathbf{r}_P \end{bmatrix} \right\}, \end{aligned} \quad (\text{C.15})$$

where the covariance matrix

$$\begin{aligned} \mathbf{R} &= \mathbb{E} \left\{ \begin{bmatrix} \mathbf{r}_S \mathbf{r}_S^H & \mathbf{r}_S \mathbf{r}_P^H \\ \mathbf{r}_P \mathbf{r}_S^H & \mathbf{r}_P \mathbf{r}_P^H \end{bmatrix} \right\} \\ &= \begin{bmatrix} (\sigma_h^2 \sigma_s^2 + \sigma_v^2) \mathbf{I} & \sigma_h^2 \mathbf{x}_S(\varepsilon) \mathbf{x}_P(\varepsilon)^H e^{-i \frac{2\pi \varepsilon N_g}{N}} \\ \sigma_h^2 \mathbf{x}_P(\varepsilon) \mathbf{x}_S(\varepsilon)^H e^{i \frac{2\pi \varepsilon N_g}{N}} & (\sigma_h^2 \sigma_s^2 + \sigma_v^2) \mathbf{I} \end{bmatrix}. \end{aligned} \quad (\text{C.16})$$

Following similar procedure as in Appendix C.1 and leaving out algebraic manipulation, the ML estimation of ε_{IFO} is obtained by

$$\begin{aligned} \hat{\varepsilon}_{\text{IFO,ML}} &= \arg \max_{\varepsilon} \Lambda(\varepsilon) = \arg \max_{\varepsilon} \left\{ - \begin{bmatrix} \mathbf{r}_S^H & \mathbf{r}_P^H \end{bmatrix} \mathbf{R}^{-1} \begin{bmatrix} \mathbf{r}_S \\ \mathbf{r}_P \end{bmatrix} \right\} \\ &= \arg \max_{\varepsilon} \left\{ \mathbf{r}_P^H \mathbf{x}_P(\varepsilon) \mathbf{x}_S(\varepsilon)^H \mathbf{r}_S \cdot e^{i \frac{2\pi \varepsilon N_g}{N}} + \mathbf{r}_S^H \mathbf{x}_S(\varepsilon) \mathbf{x}_P(\varepsilon)^H \mathbf{r}_P \cdot e^{-i \frac{2\pi \varepsilon N_g}{N}} \right\} \\ &= \arg \max_{\varepsilon} \left\{ \Re \left\{ \mathbf{r}_P^H \mathbf{x}_P(\varepsilon) \mathbf{x}_S(\varepsilon)^H \mathbf{r}_S \cdot e^{i \frac{2\pi \varepsilon N_g}{N}} \right\} \right\} \quad |\varepsilon \in \mathbb{Z}. \end{aligned} \quad (\text{C.17})$$

This is equivalent to the expression given in Equation (4.4).

C.3. Residual Frequency Offset (RFO) - derivation of Equation (4.6)

Similarly for the RFO, we consider a small-valued RFO ε and define the received reference signal vectors as

$$\mathbf{r}_l = e^{i \frac{2\pi \varepsilon l(N+N_g)}{N}} \cdot \mathbf{H} \mathbf{x}_l + \mathbf{v}_l, \quad (\text{C.18})$$

$$\mathbf{r}_{l+N_s} = e^{i \frac{2\pi \varepsilon (l+N_s)(N+N_g)}{N}} \cdot \mathbf{H} \mathbf{x}_{l+N_s} + \mathbf{v}_{l+N_s}, \quad (\text{C.19})$$

where N_s is the distance between the two cell-specific reference signals in the same subcarrier. Specifically, in Long Term Evolution (LTE), it equals the number of OFDM symbols in one slot. Thus, the log-likelihood function for the ε can be

expressed as

$$\begin{aligned}\Lambda(\varepsilon) &= \ln f(\mathbf{r}_l, \mathbf{r}_{l+N_s}; \varepsilon) \\ &= \ln \frac{1}{\pi^{2N_p} \det(\mathbf{R})} \exp \left\{ - \begin{bmatrix} \mathbf{r}_l^H & \mathbf{r}_{l+N_s}^H \end{bmatrix} \mathbf{R}^{-1} \begin{bmatrix} \mathbf{r}_l \\ \mathbf{r}_{l+N_s} \end{bmatrix} \right\},\end{aligned}\quad (\text{C.20})$$

where the covariance matrix

$$\begin{aligned}\mathbf{R} &= \mathbb{E} \left\{ \begin{bmatrix} \mathbf{r}_l \mathbf{r}_l^H & \mathbf{r}_l \mathbf{r}_{l+N_s}^H \\ \mathbf{r}_{l+N_s} \mathbf{r}_l^H & \mathbf{r}_{l+N_s} \mathbf{r}_{l+N_s}^H \end{bmatrix} \right\} \\ &= \begin{bmatrix} (\sigma_h^2 \sigma_s^2 + \sigma_v^2) \mathbf{I} & \sigma_h^2 \mathbf{x}_l \mathbf{x}_{l+N_s}^H e^{-i \frac{2\pi \varepsilon N_s (N+N_g)}{N}} \\ \sigma_h^2 \mathbf{x}_{l+N_s} \mathbf{x}_l^H e^{i \frac{2\pi \varepsilon N_s (N+N_g)}{N}} & (\sigma_h^2 \sigma_s^2 + \sigma_v^2) \mathbf{I} \end{bmatrix}.\end{aligned}\quad (\text{C.21})$$

Following similar procedure as in Appendix C.1 and leaving out algebraic manipulation, the ML estimation of ε_{RFO} is obtained by

$$\begin{aligned}\hat{\varepsilon}_{\text{RFO,ML}} &= \arg \max_{\varepsilon} \Lambda(\varepsilon) = \arg \max_{\varepsilon} \left\{ - \begin{bmatrix} \mathbf{r}_l^H & \mathbf{r}_{l+N_s}^H \end{bmatrix} \mathbf{R}^{-1} \begin{bmatrix} \mathbf{r}_l \\ \mathbf{r}_{l+N_s} \end{bmatrix} \right\} \\ &= \arg \max_{\varepsilon} \left\{ \mathbf{r}_{l+N_s}^H \mathbf{x}_{l+N_s} \mathbf{x}_l^H \mathbf{r}_l \cdot e^{i \frac{2\pi \varepsilon N_s (N+N_g)}{N}} + \mathbf{r}_l^H \mathbf{x}_l \mathbf{x}_{l+N_s}^H \mathbf{r}_{l+N_s} \cdot e^{-i \frac{2\pi \varepsilon N_s (N+N_g)}{N}} \right\} \\ &= \arg \max_{\varepsilon} \left\{ \Re \left\{ \mathbf{r}_{l+N_s}^H \mathbf{x}_{l+N_s} \mathbf{x}_l^H \mathbf{r}_l \cdot e^{i \frac{2\pi \varepsilon N_s (N+N_g)}{N}} \right\} \right\} \\ &= -\frac{1}{2\pi} \frac{N}{N_s(N+N_g)} \arg \{ \mathbf{r}_{l+N_s}^H \mathbf{x}_{l+N_s} \mathbf{x}_l^H \mathbf{r}_l \},\end{aligned}\quad (\text{C.22})$$

which is equivalent to the expression given in Equation (4.6).

D. Theoretical Mean Squared Error (MSE) and Cramér-Rao Lower Bound (CRLB)

D.1. Theoretical Mean Squared Error (MSE) - derivation of Equation (4.9)

The theoretical MSE of the previously derived Maximum Likelihood (ML) estimator (Equation (C.7)) is shown in this section. Using the simplified system model of single-input single-output in Equation (C.1) and Equation (C.2), Equation (C.7) can be rewritten as

$$\hat{\varepsilon}_{\text{FFO,ML}} = -\frac{1}{2\pi} \arg\{\mathbf{r}^H \mathbf{r}_{\text{CP}}\} = -\frac{1}{2\pi} \arctan \frac{\Im\{\mathbf{r}^H \mathbf{r}_{\text{CP}}\}}{\Re\{\mathbf{r}^H \mathbf{r}_{\text{CP}}\}}, \quad (\text{D.1})$$

where $\Re\{\cdot\}$ and $\Im\{\cdot\}$ are operators to extract the real and imaginary parts of the argument respectively. Correspondingly, the estimation error can be written as

$$\varepsilon - \hat{\varepsilon}_{\text{FFO,ML}} = \frac{1}{2\pi} \arctan \frac{\Im\{\mathbf{r}^H \mathbf{r}_{\text{CP}} e^{i2\pi\varepsilon}\}}{\Re\{\mathbf{r}^H \mathbf{r}_{\text{CP}} e^{i2\pi\varepsilon}\}}. \quad (\text{D.2})$$

Assuming small estimation error, Equation (D.2) can be approximated to

$$\varepsilon - \hat{\varepsilon}_{\text{FFO,ML}} = \frac{1}{2\pi} \frac{\Im\{\mathbf{r}^H \mathbf{r}_{\text{CP}} e^{i2\pi\varepsilon}\}}{\Re\{\mathbf{r}^H \mathbf{r}_{\text{CP}} e^{i2\pi\varepsilon}\}}. \quad (\text{D.3})$$

Specifically,

$$\begin{aligned} \mathbf{r}^H \mathbf{r}_{\text{CP}} \cdot e^{i2\pi\varepsilon} &= (\mathbf{z}^H \cdot e^{-i2\pi\hat{\varepsilon}} + \mathbf{v}^H)(\mathbf{z} + \mathbf{v}_{\text{CP}}) \cdot e^{i2\pi\varepsilon} \\ &= \|\mathbf{z}\|_2^2 \cdot \underbrace{e^{i2\pi(\varepsilon-\hat{\varepsilon})}}_{\approx 1} + \mathbf{z}^H \mathbf{v}_{\text{CP}} \cdot \underbrace{e^{i2\pi(\varepsilon-\hat{\varepsilon})}}_{\approx 1} + \mathbf{v}^H \mathbf{z} \cdot e^{i2\pi\varepsilon} + \mathbf{v}^H \mathbf{v}_{\text{CP}} \cdot e^{i2\pi\varepsilon} \end{aligned} \quad (\text{D.4})$$

When relatively large Signal to Noise Ratio (SNR) is assumed, there is

$$\Re\{\|\mathbf{z}\|_2^2\} \gg \Re\{\mathbf{z}^H \mathbf{v}_{\text{CP}} \cdot e^{i2\pi\varepsilon} + \mathbf{v}^H \mathbf{z} \cdot e^{i2\pi\varepsilon} + \mathbf{v}^H \mathbf{v}_{\text{CP}} \cdot e^{i2\pi\varepsilon}\}. \quad (\text{D.5})$$

Thus, the denominator in Equation (D.3) becomes

$$\Re\{\mathbf{r}^H \mathbf{r}_{\text{CP}} e^{i2\pi\varepsilon}\} = \|\mathbf{z}\|_2^2, \quad (\text{D.6})$$

Define σ_z^2 as the average signal power of the received signal in the time domain, given that the noise elements are of zero mean and variance σ_v^2 , we obtain from the nominator of Equation (D.3)

$$\mathbb{E}\{|\Im\{\cdot\}|^2\} = N_g \left(\sigma_z^2 \sigma_v^2 + \frac{1}{2} \sigma_v^4 \right). \quad (\text{D.7})$$

Therefore, the MSE of the Fractional Frequency Offset (FFO) estimator can be expressed as

$$\begin{aligned} \text{MSE}_{\text{FFO}} &= \mathbb{E}\{|\varepsilon - \hat{\varepsilon}_{\text{FFO,ML}}|^2\} = \frac{1}{4\pi^2} \cdot \frac{\mathbb{E}\{|\Im\{\mathbf{r}^H \mathbf{r}_{\text{CP}} e^{i2\pi\varepsilon}\}|^2\}}{\mathbb{E}\{|\Re\{\mathbf{r}^H \mathbf{r}_{\text{CP}} e^{i2\pi\varepsilon}\}|^2\}} \\ &= \frac{1}{4\pi^2} \cdot \frac{N_g (\sigma_z^2 \sigma_v^2 + \frac{1}{2} \sigma_v^4)}{N_g^2 \sigma_z^4} = \frac{1}{4\pi^2} \cdot \frac{2\gamma_T + 1}{2N_g \gamma_T^2} \quad \left| \gamma_T = \sigma_z^2 / \sigma_v^2 \right. \\ &\approx \frac{1}{4\pi^2 N_g \gamma_T} \quad \text{for large } \gamma_T \end{aligned} \quad (\text{D.8})$$

When multiple Orthogonal Frequency Division Multiplexing (OFDM) symbols from multiple Receiver (RX) antennas are available for estimation, the received signal \mathbf{r} and \mathbf{r}_{CP} will be concatenated up to a length of $N_g N_R N_f$, which leads to Equation (4.9) for the Long Term Evolution (LTE) downlink.

D.2. Cramér-Rao Lower Bound (CRLB) - derivation of Equation (4.10)

For any unbiased estimator, the MSE is lower bounded as

$$\text{MSE}_{\hat{\varepsilon}} \geq \frac{1}{J(\varepsilon)}, \quad (\text{D.9})$$

where $J(\varepsilon)$ is known as the Fisher information, written as [61]

$$J(\varepsilon) = -\mathbb{E}\left\{\frac{\partial^2}{\partial \varepsilon^2} \ln f(\mathbf{x}; \varepsilon)\right\}. \quad (\text{D.10})$$

Given the log-likelihood function in Equation (C.3), the Fisher information can be

calculated as

$$\begin{aligned}
J(\varepsilon) &= -\mathbb{E}\left\{\frac{\partial^2}{\partial\varepsilon^2}\Lambda(\varepsilon)\right\} = -\mathbb{E}\left\{\frac{\partial^2}{\partial\varepsilon^2}\ln f(\mathbf{r}_{\text{CP}}, \mathbf{r}; \varepsilon)\right\} & (\text{D.11}) \\
&= -\mathbb{E}\left\{\frac{\partial^2}{\partial\varepsilon^2}\left(-\begin{bmatrix} \mathbf{r}_{\text{CP}}^{\text{H}} & \mathbf{r}^{\text{H}} \end{bmatrix} \mathbf{R}^{-1} \begin{bmatrix} \mathbf{r}_{\text{CP}} \\ \mathbf{r} \end{bmatrix}\right)\right\} \\
&= -\mathbb{E}\left\{\frac{\partial^2}{\partial\varepsilon^2}\left(\frac{1}{2\sigma_z^2\sigma_v^2 + \sigma_v^4} \cdot \right.\right. \\
&\quad \left.\left. \cdot \left(\sigma_z^2 e^{i2\pi\varepsilon} \mathbf{r}^{\text{H}} \mathbf{r}_{\text{CP}} + \sigma_z^2 e^{-i2\pi\varepsilon} \mathbf{r}_{\text{CP}}^{\text{H}} \mathbf{r} - (\sigma_z^2 + \sigma_v^2) (\|\mathbf{r}_{\text{CP}}\|_2^2 + \|\mathbf{r}\|_2^2)\right)\right)\right\} \\
&= -\frac{1}{2\sigma_z^2\sigma_v^2 + \sigma_v^4} \cdot \mathbb{E}\left\{-4\pi^2\sigma_z^2 e^{i2\pi\varepsilon} \mathbf{r}^{\text{H}} \mathbf{r}_{\text{CP}} - 4\pi^2\sigma_z^2 e^{-i2\pi\varepsilon} \mathbf{r}_{\text{CP}}^{\text{H}} \mathbf{r}\right\} \\
&= \frac{8\pi^2\sigma_z^4 N_g}{2\sigma_z^2\sigma_v^2 + \sigma_v^4}. & (\text{D.12})
\end{aligned}$$

This leads to the CRLB for the FFO estimation given the knowledge of \mathbf{r}_{CP} and \mathbf{r} :

$$\text{MSE}_{\text{FFO}} \geq \frac{2\sigma_z^2\sigma_v^2 + \sigma_v^4}{8\pi^2\sigma_z^4 N_g} \quad (\text{D.13})$$

Extend the signal model to the N_f OFDM symbols and N_R RX antenna case, we arrive at the expression in Equation (4.10).